



electronics

Electromagnetic Interference and Compatibility

Edited by

Paolo Stefano Crovetto

Printed Edition of the Special Issue Published in *Electronics*

Electromagnetic Interference and Compatibility

Electromagnetic Interference and Compatibility

Editor

Paolo Stefano Crovetto

MDPI • Basel • Beijing • Wuhan • Barcelona • Belgrade • Manchester • Tokyo • Cluj • Tianjin



Editor

Paolo Stefano Crovetti
Politecnico di Torino
Italy

Editorial Office

MDPI
St. Alban-Anlage 66
4052 Basel, Switzerland

This is a reprint of articles from the Special Issue published online in the open access journal *Electronics* (ISSN 2079-9292) (available at: https://www.mdpi.com/journal/electronics/special_issues/eimc#).

For citation purposes, cite each article independently as indicated on the article page online and as indicated below:

LastName, A.A.; LastName, B.B.; LastName, C.C. Article Title. <i>Journal Name</i> Year , Volume Number, Page Range.
--

ISBN 978-3-0365-0500-8 (Hbk)

ISBN 978-3-0365-0501-5 (PDF)

Cover image courtesy of Paolo Crovetti.

© 2021 by the authors. Articles in this book are Open Access and distributed under the Creative Commons Attribution (CC BY) license, which allows users to download, copy and build upon published articles, as long as the author and publisher are properly credited, which ensures maximum dissemination and a wider impact of our publications.

The book as a whole is distributed by MDPI under the terms and conditions of the Creative Commons license CC BY-NC-ND.

Contents

About the Editor	vii
Preface to "Electromagnetic Interference and Compatibility"	ix
Paolo Croveti and Francesco Musolino	
Interference of Spread-Spectrum EMI and Digital Data Links under Narrowband Resonant Coupling Reprinted from: <i>Electronics</i> 2020 , 9, 60, doi:10.3390/electronics9010060	1
Leonardo Sandrolini and Andrea Mariscotti	
Signal Transformations for Analysis of Supraharmonic EMI Caused by Switched-Mode Power Supplies Reprinted from: <i>Electronics</i> 2020 , 9, 2088, doi:10.3390/electronics9122088	19
Shuaitao Zhang, Baihua Zhang, Qiang Lin, Eiji Takegami, Masahito Shoyama and Gamal M. Dousoky	
Modeling and Optimization of Impedance Balancing Technique for Common Mode Noise Attenuation in DC-DC Boost Converters Reprinted from: <i>Electronics</i> 2020 , 9, 480, doi:10.3390/electronics9030480	41
Orazio Aiello	
Electromagnetic Susceptibility of Battery Management Systems' ICs for Electric Vehicles: Experimental Study Reprinted from: <i>Electronics</i> 2020 , 9, 510, doi:10.3390/electronics9030510	57
Anna Richelli, Luigi Colalongo and Zsolt Kovacs-Vajna	
EMI Susceptibility of the Output Pin in CMOS Amplifiers Reprinted from: <i>Electronics</i> 2020 , 9, 304, doi:10.3390/electronics9020304	77
Orazio Aiello	
Hall-Effect Current Sensors Susceptibility to EMI: Experimental Study Reprinted from: <i>Electronics</i> 2019 , 8, 1310, doi:10.3390/electronics8111310	95
Jung-Han Lee	
A Novel Meander Split Power/Ground Plane Reducing Crosstalk of Traces Crossing Over Reprinted from: <i>Electronics</i> 2019 , 8, 1041, doi:10.3390/electronics8091041	109
Myunghoi Kim	
A Dual-Perforation Electromagnetic Bandgap Structure for Parallel-Plate Noise Suppression in Thin and Low-Cost Printed Circuit Boards Reprinted from: <i>Electronics</i> 2019 , 8, 719, doi:10.3390/electronics8060719	123
Muhammad Yasir, Davide di Summa, Giuseppe Ruscica, Isabella Natali Sora and Patrizia Savi	
Shielding Properties of Cement Composites Filled with Commercial Biochar Reprinted from: <i>Electronics</i> 2020 , 9, 819, doi:10.3390/electronics9050819	137
Kamil G. Gareev, Vladislava S. Bagrets, Vladimir A. Golubkov, Maria G. Ivanitsa, Ivan K. Khmel'nitskiy, Victor V. Luchinin, Olga N. Mikhailova and Dmitriy O. Testov	
Synthesis and Characterization of Polyaniline-Based Composites for Electromagnetic Compatibility of Electronic Devices Reprinted from: <i>Electronics</i> 2020 , 9, 734, doi:10.3390/electronics9050734	147

**Adrian Suarez, Jorge Victoria, Jose Torres, Pedro A. Martinez, Antonio Alcarria,
Joaquin Perez, Raimundo Garcia-Olcina, Jesus Soret, Steffen Muetsch and Alexander Gerfer**
Performance Study of Split Ferrite Cores Designed for EMI Suppression on Cables
Reprinted from: *Electronics* **2020**, *9*, 1992, doi:10.3390/electronics9121992 157

**Pablo González-Vizueté, Carlos Domínguez-Palacios, Joaquín Bernal and
María A. Martín-Prats**
Simple Setup for Measuring the Response to Differential Mode Noise of Common Mode Chokes
Reprinted from: *Electronics* **2020**, *9*, 381, doi:10.3390/electronics9030381 177

About the Editor

Paolo Stefano Croveti was born in Turin, Italy, in 1976. He received the Laurea degree (summa cum laude) and the Ph.D. degree in electronic engineering from the Politecnico di Turin, Turin, in 2000 and 2003, respectively. He is currently an Associate Professor of Electrical Engineering with the Department of Electronics and Telecommunications (DET), Politecnico di Torino, Turin. He has co-authored more than 75 articles appearing in journals and international conference proceedings. His research interests are in the fields of analog, mixed-signal, and power integrated circuit (IC) design and IC-level and System level Electromagnetic Compatibility (EMC). Prof. Croveti is a Senior Member of the IEEE and serves as the Subject Editor-in-Chief of IET Electronics Letters in the area of Circuits and Systems and as an Associate Editor of the IEEE Transactions on VLSI Systems.

Preface to "Electromagnetic Interference and Compatibility"

Due to the continuous progress in semiconductor technology and the rapidly evolving application scenarios, electromagnetic compatibility (EMC) is constantly raising new challenges and is a very dynamic field of research. In this context, this collection of papers, originally published in the "Electromagnetic Interference and Compatibility" Special Issue of *Electronics* for which I served as a Guest Editor, offers a vivid picture of the EMC research challenges and directions over the last years in this complex and multifaceted field.

Focusing on EMC in communication systems, the paper "Interference of Spread-Spectrum EMI and Digital Data Links under Narrowband Resonant Coupling" by Croveti and Musolino highlights how traditional methods like spread-spectrum clock modulation, developed with reference to AM and FM radio receivers, are no longer well suited to digital communications.

In the very crucial field of EMC in power electronics, the paper "Signal Transformations for Analysis of Supraharmonic EMI Caused by Switched-Mode Power Supplies" by Sandrolini and Mariscotti explores advanced signal processing techniques (Wavelet Packet Transform and the Empirical Mode Decomposition) in the analysis of electromagnetic emissions of power converters, while in "Modeling and Optimization of Impedance Balancing Technique for Common Mode Noise Attenuation in DC-DC Boost Converters," by Shuaitao Zhang et al. more conventional balancing techniques are optimized to attenuate common-mode emissions.

For new application scenarios, EMC challenges in emerging electric vehicles are addressed in "Electromagnetic Susceptibility of Battery Management Systems' ICs for Electric Vehicles: Experimental Study," by Aiello. Moreover, IC-level EMC issues in operational amplifiers are addressed in "EMI Susceptibility of the Output Pin in CMOS Amplifiers" by Richelli, Colalongo, and Kovacs-Vajna, and the susceptibility of Hall Effect sensors is studied in "Hall-Effect Current Sensors Susceptibility to EMI: Experimental Study" by Aiello.

New contributions in the area of cross-talk reduction and signal/power integrity are presented in "A Novel Meander Split Power/Ground Plane Reducing Crosstalk of Traces Crossing Over" by Jung-Han Lee and in "A Dual-Perforation Electromagnetic Bandgap Structure for Parallel-Plate Noise Suppression in Thin and Low-Cost Printed Circuit Boards" by Myunghoi Kim.

The active research area on the EMC properties of materials and their application to the suppression of interference is represented in this volume by "Shielding Properties of Cement Composites Filled with Commercial Biochar" by Yasir et al. and by "Synthesis and Characterization of Polyaniline-Based Composites for Electromagnetic Compatibility of Electronic Devices" by Gareev et al. Last, but not least, new contributions on ferrite cores and their characterization are presented in "Performance Study of Split Ferrite Cores Designed for EMI Suppression on Cables" by Suarez et al. and in "Simple Setup for Measuring the Response to Differential Mode Noise of Common Mode Chokes" by González-Vizuet et al.

Though not exhaustive, the papers collected in this volume can be useful to address practical EMC problems and stimulate future research and should be well received by the EMC community.

Paolo Stefano Croveti
Editor

Article

Interference of Spread-Spectrum EMI and Digital Data Links under Narrowband Resonant Coupling

Paolo Stefano Crovetti [†] and Francesco Musolino [†]

Department of Electronics and Telecommunications (DET), Politecnico di Torino, 10129 Turin, Italy; francesco.musolino@polito.it

* Correspondence: paolo.crovetti@polito.it; Tel.: +39-011-090-4220

[†] The authors contributed equally to this work.

Received: 6 November 2019; Accepted: 17 December 2019; Published: 1 January 2020

Abstract: In this paper, the effects of electromagnetic interference (EMI) coupled to a radio-frequency (RF) communication channel by resonant mechanisms are investigated and described in the framework of Shannon information theory in terms of an equivalent channel capacity loss so that to analyze and compare the effects of non-modulated and random Spread Spectrum (SS) modulated EMI. The analysis reveals a higher EMI-induced capacity loss for SS-modulated compared to non modulated EMI under practical values of the quality factor Q , while a modest improvement in the worst case capacity loss is observed only for impractical values of Q . Simulations on a 4-quadrature amplitude modulation (4-QAM) digital link featuring Turbo coding under EMI resonant coupling reveal that SS-modulated EMI gives rise to higher bit error rate (BER) at lower EMI power compared non-modulated EMI in the presence of resonant coupling for practical values of Q , thus suggesting a worse interfering potential of SS-modulated EMI.

Keywords: Spread Spectrum; DC–DC power converters; digital communications; channel capacity; resonant coupling

1. Introduction

Due to the widespread diffusion of highly integrated information and communication technology (ICT) systems like smartphones, tablets and intelligent sensor nodes, digital communication modules operate in a more and more harsh electromagnetic environment, in which electromagnetic interference (EMI) from digital integrated circuits (ICs) and switching mode power converters can be easily coupled to the nominal signal path via the silicon substrate, the IC package and the power distribution network of ICs and printed circuit boards (PCBs), resulting in a degraded bit error rate (BER) and possibly in a complete communication failure [1–7].

As a consequence, the effects of EMI need to be addressed adopting specific countermeasures as early as possible in the design of circuits and systems and/or by limiting the coupling mechanisms so that to assure the proper operation with no penalty in terms of costs, time-to-market and performance, and also in order to meet the stringent Electromagnetic Compatibility (EMC) regulations [8–11].

For this purpose, several approaches have been proposed in recent years to mitigate EMI [12–16]. Among them, *Spread-Spectrum (SS) techniques*, which consist in the modulation of the frequency of switching signals around the nominal value, so that to spread their spectral energy over a wider bandwidth [17,18], are often adopted in clock oscillators [19–23] and DC–DC converter controllers [24–27] since they give rise to a significant (10–20 dB) reduction of EMI spectral peaks measured following EMC standards [8–11] and make it possible to meet EMC requirements at low cost. In this field, chaos-based random SS-modulations have proven to achieve the best spectral characteristics [28–30].

While SS techniques help in complying with EMC regulations, their effectiveness in reducing the interfering potential of switching signals is more controversial and has been sometimes put in question [31–34]. Moreover, SS-modulations have found to bring no BER reduction in an I^2C link operating in the presence of EMI generated by a power converter [35] and a worse interfering potential of SS-modulated compared to non-modulated EMI in Wireless Local Area Networks (WLAN) is reported in [36].

In this scenario, focusing on the effects of SS EMI on digital communications, the impact of random SS-modulated interference on baseband digital data lines has been described in [37] in terms of an equivalent channel capacity loss and compared with non-SS-modulated EMI in practical application scenarios, revealing that SS-modulated EMI can show a worse interfering potential compared to non-modulated EMI in a digital link featuring advanced channel coding. The analysis presented in [37], however, was carried out assuming frequency-independent EMI coupling in the victim channel bandwidth. This assumption conveniently describes low frequency inductive and capacitive coupling scenarios in baseband data links but could not be valid in general in the presence of radiated and conducted EMI resonant coupling mechanisms [38–42], which affect high-frequency EMI propagation and can be therefore relevant when interference with radio-frequency (RF) digital communications are considered.

Generally speaking, in the presence of resonant coupling, the adoption of SS-modulations may lead to a more significant reduction of the EMI power which is actually coupled to the victim equipment compared with the case of wideband coupling considered in [37], as illustrated in Figure 1, where B and W are the channel and the EMI bandwidth, respectively. From the figure, it can be observed that under the same resonant coupling mechanism $G(f)$, the coupled EMI power can be reduced of more than 50% by adopting SS-modulations compared to the non-SS-modulated case. In this paper the analysis in [37] is extended to investigate if and to what extent the conclusions on the worse EMI-induced capacity loss of SS-modulated signals presented in [37] apply to the case of resonant coupling.

The paper is organized as follows: in Section 2, the model of a digital communication channel under EMI resonant coupling is introduced. With reference to such a model, a description of the adverse effects of EMI in terms of capacity loss is introduced in Section 3 and discussed in Section 4. Simulations on the effects of resonant-coupled EMI from a switching mode DC–DC converter on a 4-quadrature amplitude modulation (4-QAM) data link featuring Turbo coding are then presented in Section 5 to verify the theoretical results with reference to a practical case. Finally, in Section 6, some concluding remarks are drawn.

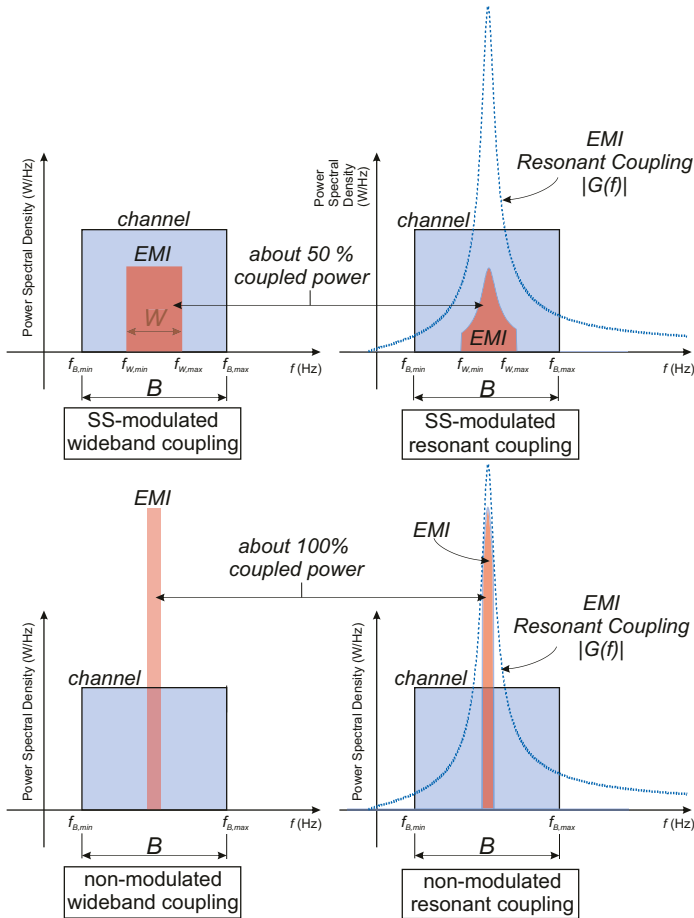


Figure 1. Effects of resonant coupling mechanisms on non-modulated and SS-modulated EMI.

2. Communication Channel Modeling under Resonant EMI Coupling

In this paper, the interfering potential of periodic and SS-modulated EMI generated by switching signals and coupled to a digital communication channel by a resonant coupling mechanism, as depicted in Figure 2, are compared in the framework of Shannon information theory in terms of an equivalent EMI-induced channel capacity loss [43], following the approach adopted in [37].

2.1. Channel Modelling

A band-limited communication channel corrupted by additive white Gaussian noise (AWGN) with unilateral power spectral density N_0 is considered in what follows. The transmitted signal and the background noise are both described by two wide-sense stationary (WSS), statistically independent gaussian random processes. In particular, the signal process is assumed to have a total power P_S and a power spectral density (p.s.d.) P_S/B constant over the channel bandwidth $B = (f_{B,min}, f_{B,max})$, as depicted in Figure 3, while the noise is assumed to have unilateral power spectral density N_0 .

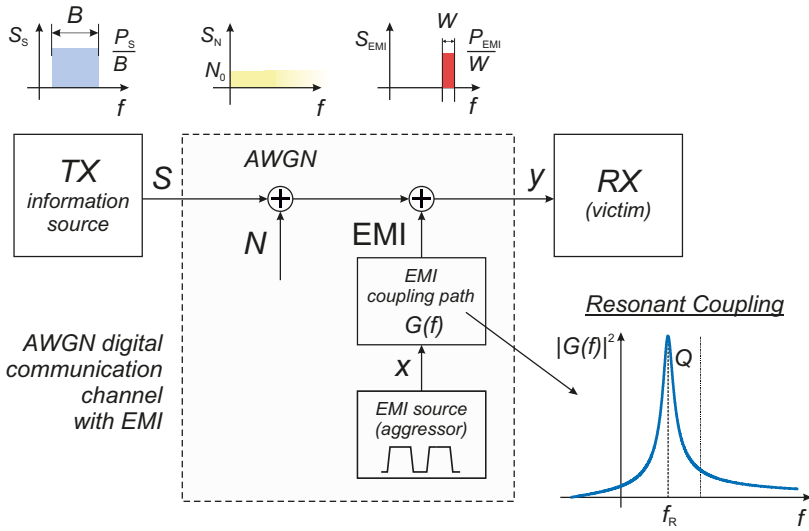


Figure 2. Digital communication channel with EMI resonant coupling: Block Diagram.

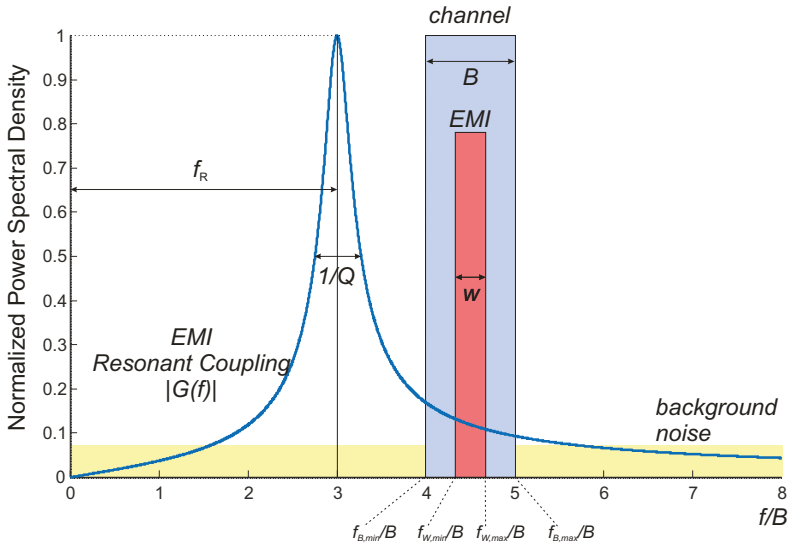


Figure 3. EMI resonant coupling in the frequency domain: power spectral densities of nominal signals, EMI, background noise and resonant coupling transfer function.

In the framework of Shannon information theory, the upper bound of the information that can be reliably transmitted over the AWGN channel considered above in the unit time, is given by the Shannon-Hartley equation [43]:

$$C_0 = B \log_2 \left(1 + \frac{P_S}{BN_0} \right) = B \log_2 (1 + \alpha) \tag{1}$$

where

$$\alpha = \frac{P_S}{BN_0}$$

is the signal-to-noise ratio (SNR) of the AWGN channel.

2.2. Modelling of a Communication Channel Affected by EMI

In the above model, it is now assumed that the communication channel is also corrupted by EMI generated by an aggressor whose operation is based on periodic or randomly SS-modulated switching signals.

In case of periodic signals, the EMI spectrum has nonzero components only at the harmonics kf_0 , with $k \in \mathbb{N}$, of the switching frequency f_0 of the aggressor. By contrast, when SS techniques are applied, the instantaneous frequency f of the aggressor varies according to the law

$$f(t) = f_0 + \delta f_0 \zeta(t) \quad (2)$$

where f_0 is the central frequency, δ is the modulation depth and $0 \leq \zeta(t) \leq 1$ is the modulation profile. As a consequence, the EMI spectral power is more or less uniformly spread over the bandwidth $[kf_0, kf_0(1 + \delta)]$ and the spectral peaks are consequently reduced. By using SS-modulations with a random modulation profile $\zeta(t)$ optimized for this purpose, the EMI power can be effectively spread over the whole spreading bandwidth $[kf_0, kf_0(1 + \delta)]$ in a nearly uniform way, leading to a reduction of the EMI p.s.d. to $P_k/k\delta f_0$ which makes it easier to comply with EMC regulations.

Under the above hypotheses, EMI around an harmonic kf_0 within the bandwidth B of the communication channel in Figure 2 is modelled by a wide-sense stationary (WSS) narrowband Gaussian process, independent both of the background noise and of the transmitted signal, with total power P_{EMI} and bandwidth W , completely or partially overlapping the signal bandwidth B .

2.3. Resonant Coupling Modeling

Even if realistic EMI coupling transfer functions can be rather complex depending on the specific physical mechanism involved in conducted/radiated EMI propagation, focusing the attention to the relatively narrow region of the spectrum included in the bandwidth of the victim channel, practical resonant coupling mechanisms can be conveniently described by a second-order resonant transfer function:

$$G(f) = G_0 \frac{\frac{f}{Qf_R}}{1 + \frac{f}{Qf_R} - \frac{f^2}{f_R^2}} \quad (3)$$

where G_0 is a frequency-independent coupling factor, f_R is the resonance frequency and Q is the quality factor.

In view of that, for the sake of simplicity and without loss of generality, the effects of resonant EMI coupling on the EMI-induced capacity loss will be discussed in the following considering the EMI transfer function $G(f)$ in (3).

3. EMI-Induced Channel Capacity Loss

Under the hypotheses introduced in the previous Section, the capacity C of a communication channel in the presence of EMI, for a single EMI harmonic overlapping completely or in part with the channel bandwidth B , as depicted in Figure 3 can be calculated as

$$C = C_1 + C_2 \quad (4)$$

where C_1 is the capacity of sub-channel where the signal bandwidth overlaps with the EMI bandwidth, i.e., over the bandwidth

$$W^* = B \cap W = [W_{\min}^*, W_{\max}^*] = [\max(f_{B_{\min}}, f_{W_{\min}}), \min(f_{B_{\max}}, f_{W_{\max}})]. \quad (5)$$

and can be expressed as

$$C_1 = \int_{W^*} \log_2 \left(1 + \frac{S_S(f)}{S_N(f) + |G(f)|^2 S_{EMI}(f)} \right) df \quad (6)$$

where:

$$S_S(f) = \frac{P_S}{B} \Pi_B(f - f_{B,\min})$$

is the signal p.s.d.,

$$S_N(f) = N_0$$

is the background noise p.s.d.,

$$S_{EMI}(f) = \frac{P_{EMI}}{W} \Pi_W(f - f_{W,\min})$$

is the EMI p.s.d. and $G(f)$ is the resonant coupling transfer function defined in (3).

By introducing in (6) the expressions of $S_S(f)$, $S_N(f)$ and $G(f)$ derived above, the capacity of the sub-channel C_1 affected by EMI can be explicitly evaluated as

$$\begin{aligned} C_1 &= \int_{B \cap W} \log_2 \left(1 + \frac{S_S(f) \left[1 + \left(\frac{1}{Q^2} - 2 \right) \frac{f^2}{f_R^2} + \frac{f^4}{f_R^4} \right]}{S_N(f) + \left[S_N(f) \left(\frac{1}{Q^2} - 2 \right) + \frac{G_0^2}{Q^2} S_{EMI}(f) \right] \frac{f^2}{f_R^2} + S_N(f) \frac{f^4}{f_R^4}} \right) df \\ &= \int_{B \cap W} \log_2 \left(1 + \frac{P_S}{BN_0} \frac{1 + \left(\frac{1}{Q^2} - 2 \right) \frac{f^2}{f_R^2} + \frac{f^4}{f_R^4}}{1 + \left(\frac{1}{Q^2} - 2 + G_0 \frac{P_{EMI}}{WN_0} \right) \frac{f^2}{f_R^2} + \frac{f^4}{f_R^4}} \right) df \\ &= \int_{B \cap W} \log_2 \left(1 + \alpha \frac{1 + \left(\frac{1}{Q^2} - 2 \right) \frac{f^2}{f_R^2} + \frac{f^4}{f_R^4}}{1 + \left(\frac{1}{Q^2} - 2 + \alpha\beta \right) \frac{f^2}{f_R^2} + \frac{f^4}{f_R^4}} \right) df \\ &= \int_{B \cap W} \log_2(1 + \alpha) + \log_2 \left(\frac{1 + a_1 \frac{f^2}{f_R^2} + \frac{f^4}{f_R^4}}{1 + a_2 \frac{f^2}{f_R^2} + \frac{f^4}{f_R^4}} \right) df \end{aligned} \quad (7)$$

where

$$a_1 = \frac{\frac{1}{Q^2} - 2 + \alpha(\beta + 1)}{1 + \alpha},$$

$$a_2 = \frac{1}{Q^2} - 2 + \alpha\beta$$

and where α is the signal-to-noise ratio as in (1) and $\beta = P_{EMI}/P_S$ is the overall EMI-to-signal power ratio. Since the integral in (7) can be calculated analytically in closed form in terms of:

$$\begin{aligned} \Theta(x, a) &= \int \log_2(x^2 + ax + 1) dx \\ &= \frac{1}{\log 2} \left[\left(x + \frac{a}{2} \right) \log(x^2 + ax + 1) - 2x + \sqrt{4 - a^2} \arctan \frac{2x - a}{\sqrt{4 - a^2}} \right] \end{aligned} \quad (8)$$

the capacity C_1 can be finally expressed as

$$C_1 = \frac{W^*}{B} C_0 + \Theta \left[\left(\frac{W_{\max}^*}{f_R} \right)^2, a_1 \right] - \Theta \left[\left(\frac{W_{\min}^*}{f_R} \right)^2, a_1 \right] - \Theta \left[\left(\frac{W_{\max}^*}{f_R} \right)^2, a_2 \right] + \Theta \left[\left(\frac{W_{\min}^*}{f_R} \right)^2, a_2 \right] \quad (9)$$

where C_0 is the capacity of the EMI-free channel.

With the same notations, the capacity C_2 of the complementary sub-channel $B - B \cap W$, not affected by EMI, can be expressed as

$$\begin{aligned} C_2 &= \int_{B-B \cap W} \log_2 \left(1 + \frac{S_S(f)}{N_0} \right) df \\ &= (B - W^*) \log_2 (1 + \alpha) = \left(1 - \frac{W^*}{B} \right) C_0. \end{aligned} \quad (10)$$

Replacing (7) and (10) in (4), the overall channel capacity in the presence of EMI can be expressed in the form

$$C = C_0 + \Delta C \quad (11)$$

where

$$\Delta C = \Theta \left[\left(\frac{W_{\max}^*}{f_R} \right)^2, a_1 \right] - \Theta \left[\left(\frac{W_{\min}^*}{f_R} \right)^2, a_1 \right] - \Theta \left[\left(\frac{W_{\max}^*}{f_R} \right)^2, a_2 \right] + \Theta \left[\left(\frac{W_{\min}^*}{f_R} \right)^2, a_2 \right] \quad (12)$$

is the channel capacity loss due to the presence of EMI.

The analysis presented so far can be applied to calculate the capacity loss ΔC_k in an AWGN channel due to EMI at frequency kf_0 with up-spreading, symmetric and down-spreading SS-modulations and modulation depth δ , by considering $W = \delta kf_0$ and appropriate values of W_{\min}^* and W_{\max}^* in (12) by the same approach detailed in [37]. Moreover, the EMI-induced capacity loss ΔC_{TOT} due to several non-overlapping EMI spectral lines can be immediately evaluated by superposition of the capacity loss contributions due to each spectral line $k = N_1 \dots N_2$ in the channel bandwidth as

$$\Delta C_{TOT} = \sum_{k=N_1}^{N_2} \Delta C_k. \quad (13)$$

4. Discussion

Based on the results presented in Section 3, the effects of SS-modulation under resonant EMI coupling are now investigated and discussed.

For this purpose, a bandpass channel with bandwidth B ranging from $f_{B_{\min}} = 4B$ to $f_{B_{\max}} = 5B$ is considered and an aggressor generating periodic or random SS-modulated EMI with a fixed total power 20dB below the total signal power, concentrated in a spectral line at frequency f_0 falling in correspondence of the central frequency of the channel $f_C = \frac{f_{B_{\min}} + f_{B_{\max}}}{2} = f_0 = 4.5B$ is considered, as depicted in Figure 4. The signal-to-background noise ratio of the channel is assumed to be 47dB so that the background thermal noise is negligible compared to EMI.

Moreover, it is assumed that the EMI source is coupled to the victim receiver by a resonant coupling function $G(f)$ in (3), with resonant frequency f_R and quality factor Q , where the scaling constant G_0 is chosen so that to have unity peak amplitude

$$\max_f |G(f)| = 1.$$

The channel capacity is evaluated accordingly as in Section 3 and is plotted in Figure 4 for $Q = 100$ versus the resonant frequency f_R and for different values of the SS EMI bandwidth W normalized with respect to the channel bandwidth B , for W/B ranging from 0 (no SS) up to 25%. Based on (2), depending on the EMI harmonic order k , the SS-modulation depth can be expressed in terms of the normalized bandwidth W/B as

$$\delta = \frac{W}{kf_0} = \frac{W}{B} \frac{1}{4.5 \cdot k}. \quad (14)$$

The same analysis is repeated in Figure 5 for different values of the quality factor Q ranging from 1 to 1,000,000 to discuss the effects of SS-modulations on signal capacity under different resonant coupling quality factors.

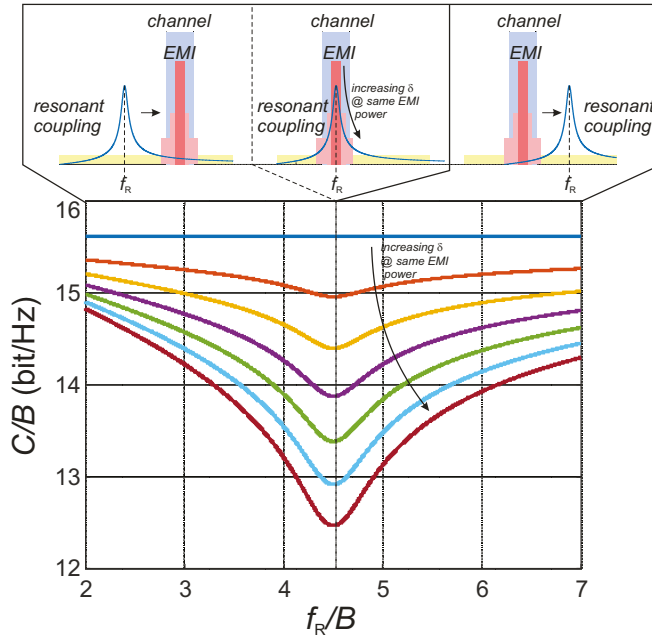


Figure 4. Normalized capacity versus resonant frequency f_R/B for a communication channel with bandwidth $B = (f_1, f_2)$ in the presence of EMI .

For $Q = 1$, the resonant behaviour is weak and the situation is similar to that considered in [37] for wideband EMI coupling (In this study, just the case of EMI bandwidth fully included in the communication channel bandwidth is considered. For extremely narrow-bandwidth communications, EMI coupling can be always considered nearly uniform over the channel bandwidth even in the presence of resonant coupling and the considerations presented in [37] can be directly extended) and an increasing EMI-induced channel capacity loss, weakly dependent on f_R , is observed for an increased SS spreading bandwidth W/B , i.e., for an increased modulation depth δ , which is consistent with [37].

For an increased quality factor Q , the channel capacity loss decreases since the EMI components far from the resonant frequency are partially filtered. Moreover, the capacity loss is more sensitive to the resonant frequency f_R and expectedly reaches a minimum when f_R is close to the EMI central frequency, i.e., for $f_C \simeq f_R$. Even in this case, however, for Q up to 10,000, the EMI-induced capacity loss gets worse and worse by increasing the spreading bandwidth W/B of SS-modulations. A beneficial effect of SS-modulations, which could be possibly expected in view of the reduced SS-EMI coupled power under resonant conditions, as highlighted in Figure 1, is observed only for extremely high Q values exceeding 10,000, where the peak capacity loss decreases for an increasing spreading bandwidth W/B . Even in these cases, for SS-modulations, a capacity impairment is experienced over a wider bandwidth compared to the case with lower W/B or no SS-modulation. Such extremely high values of the quality factor, however, are not realistic for EMI coupling.

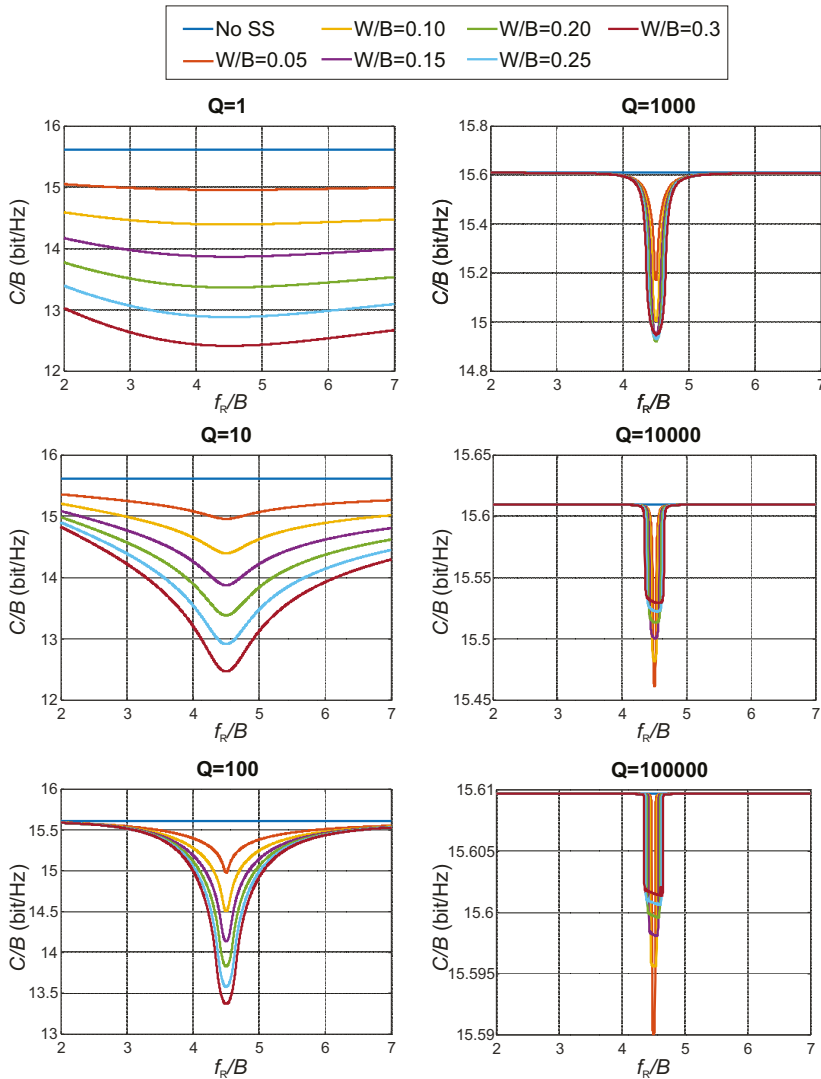


Figure 5. Normalized capacity versus resonant frequency f_R/B for the channel in Figure 3 for different values of the resonant coupling quality factor Q under constant peak coupling, reported in each plot for different SS-modulation depth δ ranging from 0 (no SS) to 30%.

To better highlight the effect of SS-modulations, the worst case channel capacity and the average EMI-induced capacity loss over different values of f_R ranging from $2B$ to $7B$ are reported in Figures 6 and 7, respectively, versus W/B . It can be clearly observed that the worst case capacity monotonically decreases with W/B for practical values of Q below 10,000 and shows an increasing behavior only for extremely high values of Q and for quite large W/B ratios, according to the previous discussion. By contrast, the average channel capacity has found to be monotonically decreasing with W/B for any value of Q .

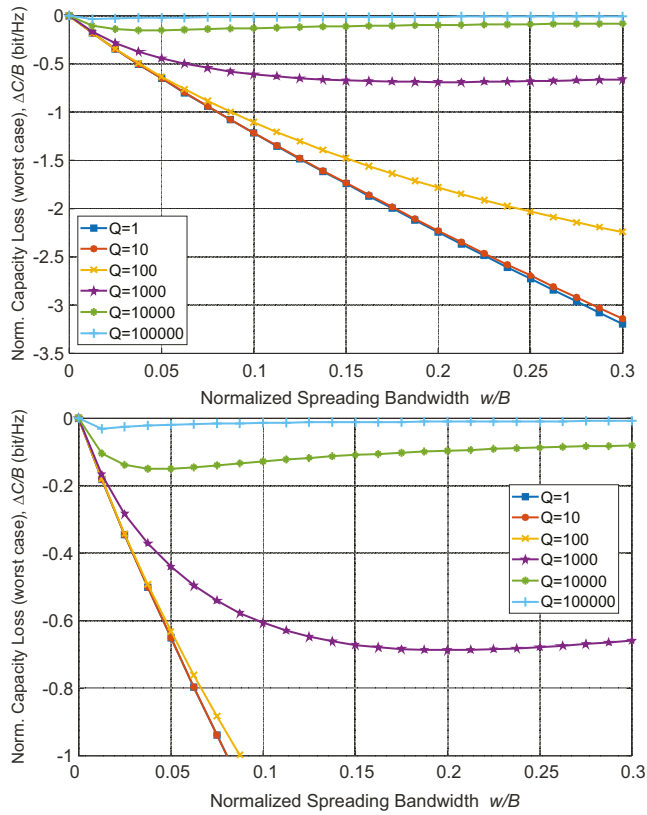


Figure 6. Worst case normalized capacity loss over different resonant frequencies f_R versus SS-modulation depth δ ranging from 0 (no SS) to 30% for different values of the resonant coupling quality factor Q under constant peak coupling. A detail of the top figure is reported in the bottom figure.

To further investigate the effect of SS-modulation under resonant coupling, the analysis described above has been repeated choosing the scaling constant G_0 in (3) so that the coupling function $G(f)$ has unitary energy, i.e., imposing

$$\int_{-\infty}^{+\infty} |G(f)|^2 df = 1.$$

In analogy with Figures 6 and 7, the average and the worst case capacity loss over different values of f_R are reported in Figure 8 versus the SS bandwidth W normalized with respect to the channel bandwidth. In this case, a monotonic decrease of both the average and of the worst case channel capacity is observed for increased W/B for all the considered values of the quality factor Q .

Under the hypotheses and limitations considered in the proposed analysis, i.e., that SS EMI can be described as a band-limited Gaussian random process, which is coupled to a wideband AWGN channel by resonant coupling described by the transfer function (3), it can be observed that the application of SS-modulations on periodic interfering signals gives rise to a larger EMI-induced capacity loss under the same EMI total power compared to non-SS-modulated EMI for almost all practical resonant EMI coupling conditions. In other words, the results on the impact of SS-modulations on EMI-induced capacity loss studied in [37] for wideband EMI coupling can be extended to practical resonant coupling conditions according to the proposed analysis.

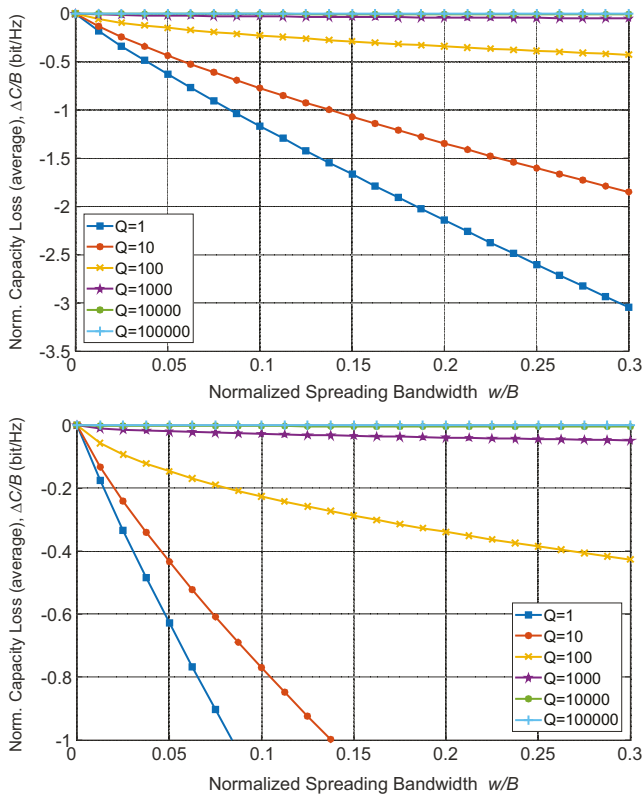


Figure 7. Average normalized capacity for resonant frequencies f_R ranging from $2B$ to $7B$ versus SS-modulation depth δ ranging from 0 (no SS) to 30% for different values of the resonant coupling quality factor Q under constant peak coupling. A detail of the top figure is reported in the bottom figure.

As observed in [37], such a larger capacity loss is not always related to an increased bit error rate (BER) in communication channels operating at sub-capacity bit rates, by the way it is expected to give rise to a worse and worse BER degradation as far as the data rate approaches the Shannon capacity limit, as in real world communication channels employing advanced channel coding schemes (e.g., Turbo coding). Under this perspective, the impact of SS-modulations on the BER of a 4-QAM digital link featuring Turbo coding will be considered as a test case in what follows.

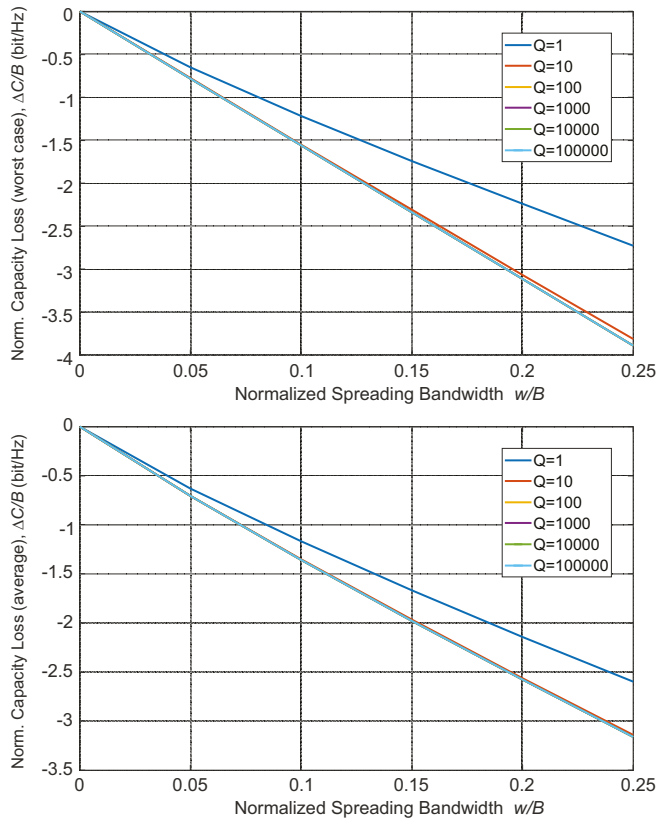


Figure 8. Worst case and average normalized capacity loss over different resonant frequencies f_R versus SS-modulation depth δ ranging from 0 (no SS) to 25% for different values of the resonant coupling quality factor Q under constant coupling integral.

5. Impact of Spread Spectrum Modulations in a 4-QAM Channel under Resonant EMI Coupling

The effects of SS EMI on a communication channel under resonant EMI coupling, which have been discussed in the previous section in a completely general, coding-independent way in terms of equivalent channel capacity loss, are now investigated with reference to a synchronous buck DC–DC power converter interfering with a 4-QAM digital link featuring Turbo coding, which makes it possible to achieve a data rate approaching the channel capacity and is therefore expected to be more sensitive to EMI-induced capacity loss [37].

Test Setup

The interference generated by a synchronous buck DC–DC converter has been measured and added in simulation to the input signal of a 4-QAM digital communication channel under resonant coupling with $Q = 1$ and $Q = 100$.

In order to extract the EMI waveforms, the test setup in Figure 9, which is the same presented in [35], is considered. Here, a DC–DC power converter is intentionally designed to interfere with a digital data link. The converter is a hard-switched synchronous Buck operated from an input voltage $V_{IN} = 16$ V and connected to a load $R_L = 10$ Ω in open-loop mode with a fixed duty cycle $D = 0.375$. Such a converter is driven by a 100kHz PWM signal generated by a microcontroller, which can be programmed to operate at constant frequency or with an SS random frequency modulation with

different modulation depth δ . The EMI voltage v_c at the receiver input without SS-modulation and with random SS-modulation at different modulation depth δ is acquired by a digital scope at 125 MS/s during the DC–DC converter operation and is stored in a database. The power spectral density of the measured waveform for periodic and random SS-modulated ($\delta = 6\%$) is reported in Figure 10.

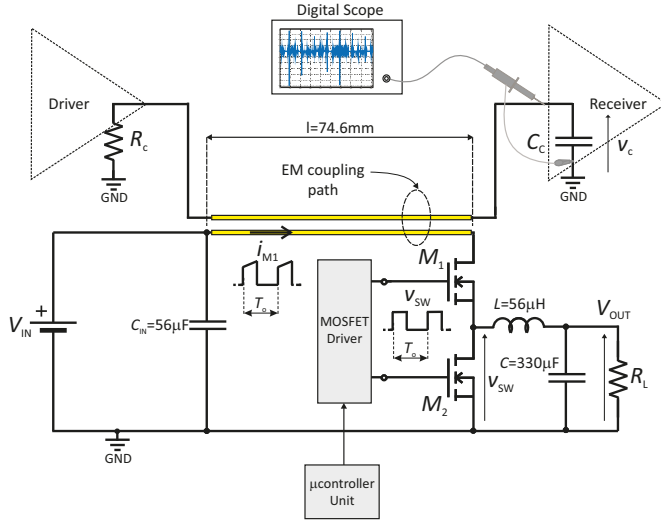


Figure 9. Schematic view of the test setup.

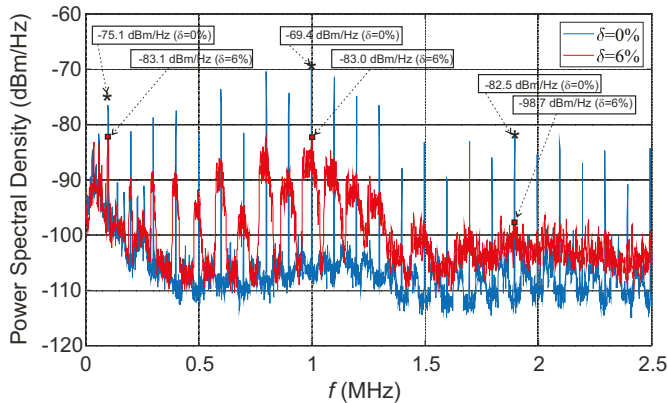


Figure 10. Measured power spectral density of periodic and random SS-modulated ($\delta = 6\%$) EMI.

Then, the measured EMI waveforms are added in simulation to the input of a 4-QAM receiver, modelling the EMI propagation path to the receiver as a resonant transfer function $G(f)$ with $Q = 1$ and $Q = 100$ to discuss the impact of different resonant coupling mechanisms.

For this purpose, a 4-QAM communication scheme over an AWGN channel with $B = 600$ kHz bandwidth is considered and the effects of non-modulated and SS-modulated EMI coupled to the channel bandwidth with a resonant transfer function with $Q = 1$ and with $Q = 100$ have been simulated in the Matlab environment, adding the measured non-modulated and SS-modulated EMI waveforms generated by the power converter to the received input signal.

In Figure 11, resonant coupling with $Q = 1$ is considered and the BER is plotted versus the r.m.s. EMI amplitude (disturbances with different amplitudes have been obtained applying a scaling factor

to the same measured EMI waveforms) for different values of the modulation depth δ . From the figure, it can be observed that the EMI amplitude at which BER starts increasing in a significant way is lower for a larger SS-modulation depth and higher in the non-modulated case or for small values of δ .

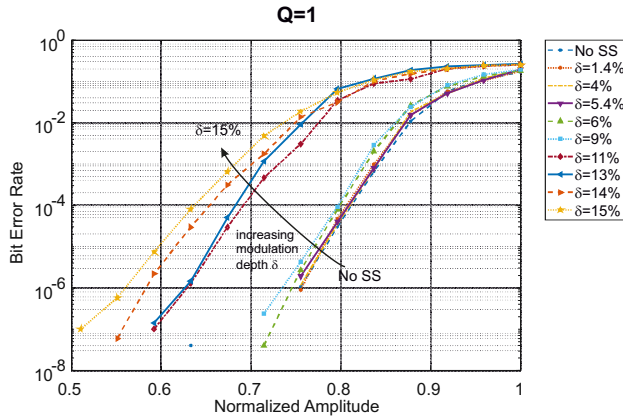


Figure 11. Bit error rate of a communication channel corrupted by SS-modulated EMI under weakly resonant coupling ($Q = 1$) vs. EMI normalized r.m.s. amplitude at different modulation depth δ .

Comparing non-modulated EMI with SS-modulated EMI, a similar BER is achieved for a 20% higher EMI amplitude in the non-modulated case. In Figure 12, the same analysis is performed under resonant EMI coupling with quality factor $Q = 100$. In this case, a similar BER is achieved for a 3.4X higher EMI amplitude than in the non-modulated cases, revealing an even worse impact of SS-modulations on the BER when an EMI resonant coupling with a higher Q factor is introduced.

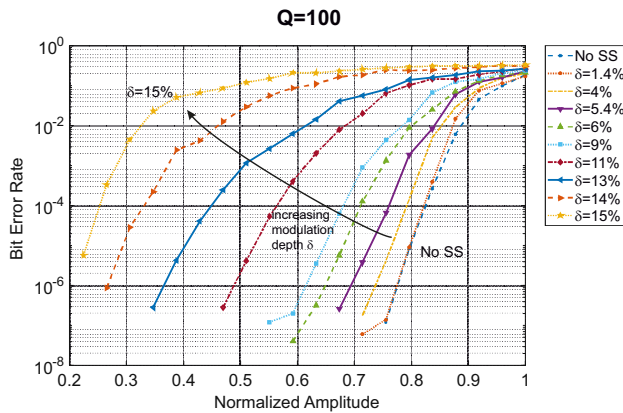


Figure 12. Bit error rate of a communication channel corrupted by SS-modulated EMI under strongly resonant coupling ($Q = 100$) vs. EMI normalized r.m.s. amplitude at different modulation depth δ .

Based on the same analysis described above, the BER has been plotted for different EMI power levels versus the modulation depth δ in Figure 13 for $Q = 1$ and in Figure 14 for $Q = 100$ and also in this case a worse BER degradation with increased SS-modulation depth is observed for resonant coupling with an increased quality factor.

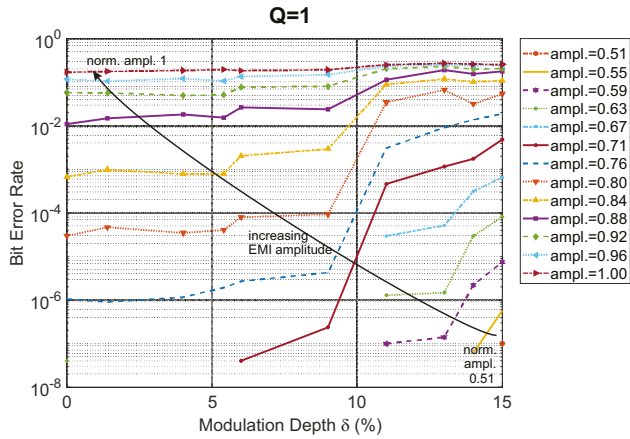


Figure 13. Bit error rate of a communication channel corrupted by SS-modulated EMI under weakly resonant coupling ($Q = 1$) vs. different modulation depth δ at different EMI normalized r.m.s. amplitude values.

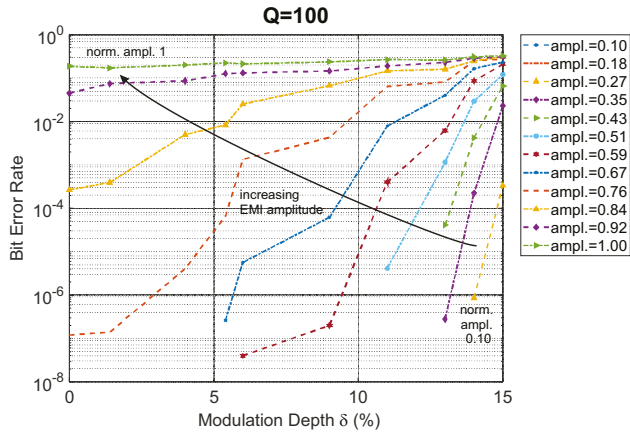


Figure 14. Bit error rate of a communication channel corrupted by SS-modulated EMI under strongly resonant coupling ($Q = 100$) vs. different modulation depth δ at different EMI normalized r.m.s. amplitude values.

6. Conclusions

The effects of EMI coupled to a communication channel by narrowband resonant mechanisms have been investigated in terms of an equivalent channel capacity loss. In this framework, the effects of non-modulated and random SS-modulated EMI under different resonant frequency and quality factors of the EMI coupling mechanism have been compared, thus extending the analysis presented in [37], which was limited to the case of wideband EMI coupling. The analysis has revealed a higher EMI-induced capacity loss for SS-modulated compared to non modulated EMI under practical values of the quality factor Q , while a modest improvement in the worst case capacity loss is observed only for impractical values of Q exceeding 10,000. Simulations on a 4-QAM digital link featuring Turbo coding under EMI resonant coupling have also revealed that SS-modulated EMI gives rise to higher BER at lower EMI power compared WITH non-modulated EMI also in the presence of resonant coupling with practical values, thus confirming a worse interfering potential of SS-modulated EMI.

Author Contributions: Conceptualization, methodology, formal analysis: P.S.C.; validation, writing F.M. All authors have read and agreed to the published version of the manuscript.

Funding: This research received no external funding.

Conflicts of Interest: The authors declare no conflict of interest.

References

1. Dhia, S.B.; Ramdani, M.; Sicard, E. *Electromagnetic Compatibility of Integrated Circuits: Techniques for Low Emission and Susceptibility*; Springer: New York, NY, USA, 2006.
2. Archambeault, B.; Ruehli, A.E. Analysis of power/ground-plane EMI decoupling performance using the partial-element equivalent circuit technique. *IEEE Trans. Electromagn. Compatibil.* **2001**, *43*, 437–445. [[CrossRef](#)]
3. Shringarpure, K.; Pan, S.; Kim, J.; Fan, J.; Achkir, B.; Archambeault, B.; Drewniak, J.L. Sensitivity Analysis of a Circuit Model for Power Distribution Network in a Multilayered Printed Circuit Board. *IEEE Trans. Electromagn. Compatibil.* **2017**, *59*, 1993–2001. [[CrossRef](#)]
4. Kim, J.; Rotaru, M.D.; Baek, S.; Park, J.; Iyer, M.K.; Kim, J. Analysis of noise coupling from a power distribution network to signal traces in high-speed multilayer printed circuit boards. *IEEE Trans. Electromagn. Compatibil.* **2006**, *48*, 319–330. [[CrossRef](#)]
5. Crovetto, P.S. Operational amplifier immune to EMI with no baseband performance degradation. *Electron. Lett.* **2010**, *46*, 209–210. [[CrossRef](#)]
6. Redouté, J.; Richelli, A. A methodological approach to EMI resistant analog integrated circuit design. *IEEE Electr. Comp. Mag.* **2015**, *4*, 92–100. [[CrossRef](#)]
7. Villavicencio, Y.; Musolino, F.; Fiori, F. Electrical Model of Microcontrollers for the Prediction of Electromagnetic Emissions. *IEEE Trans. Very Large Scale Integr. (VLSI) Syst.* **2011**, *19*, 1205–1217. [[CrossRef](#)]
8. 'Code of Federal Regulations, Title 47, Chapter I, Subchapter A, Part 15, Subpart B: Unintentional Radiators'. Available online: <https://www.ecfr.gov/> (accessed on 19 July 2018).
9. Council Directive 89/336/EEC on the Approximation of the Laws of the Member States Relating to Electromagnetic Compatibility; Official Journal of the European Union, Technical Report L139/19; The Publications Office of the European Union: Luxembourg, 1989.
10. CISPR 11:2015 Industrial, Scientific and Medical Equipment - Radio-Frequency Disturbance Characteristics—Limits and Methods of Measurement; IEC: Geneva, Switzerland, 2015.
11. CISPR 14-1:2016 Electromagnetic Compatibility - Requirements for Household Appliances, Electric Tools and Similar Apparatus—Part 1: Emission; IEC: Geneva, Switzerland, 2016.
12. Musolino, F.; Villavicencio, Y.; Fiori, F. Chip-Level Design Constraints to Comply With Conducted Electromagnetic Emission Specifications. *IEEE Trans. Electromagn. Compatibil.* **2012**, *54*, 1137–1146. [[CrossRef](#)]
13. Crovetto, P.S.; Fiori, F.L. Efficient BEM-based substrate network extraction in silicon SoCs. *Microelectron. J.* **2008**, *39*, 1774–1784. [[CrossRef](#)]
14. Lobsiger, Y.; Kolar, J.W. Closed-Loop di/dt and dv/dt IGBT Gate Driver. *IEEE Trans. Power Electron.* **2015**, *30*, 3402–3417. [[CrossRef](#)]
15. Chung, H.; Hui, S.Y.R.; Tse, K.K. Reduction of power converter EMI emission using soft-switching technique. *IEEE Trans. Electromagn. Compatibil.* **1998**, *40*, 282–287. [[CrossRef](#)]
16. Pareschi, F.; Rovatti, R.; Setti, G. EMI Reduction via Spread Spectrum in DC/DC Converters: State of the Art, Optimization, and Tradeoffs. *IEEE Access* **2015**, *3*, 2857–2874. [[CrossRef](#)]
17. Lin, F.; Chen, D.Y. Reduction of power supply EMI emission by switching frequency modulation. *IEEE Trans. Power Electron.* **1994**, *9*, 132–137.
18. Hardin, K.B.; Fessler, J.T.; Bush, D.R. Spread spectrum clock generation for the reduction of radiated emissions. In Proceedings of the IEEE Symposium on Electromagnetic Compatibility, Chicago, IL, USA, 22–26 August 1994; pp. 227–231.
19. Chen, Y.; Ma, D.B. 15.7 An 8.3MHz GaN Power Converter Using Markov Continuous RSSM for 35dB μ V Conducted EMI Attenuation and One-Cycle TON Rebalancing for 27.6dB VO Jittering Suppression. In Proceedings of the 2019 IEEE International Solid- State Circuits Conference—(ISSCC), San Francisco, CA, USA, 17–21 February 2019; pp. 250–252.

20. De Martino, M.; De Caro, D.; Esposito, D.; Napoli, E.; Petra, N.; Strollo, A.G.M. A Standard-Cell-Based All-Digital PWM Modulator With High Resolution and Spread-Spectrum Capability. *IEEE Trans. Circuits Syst. I Regul. Pap.* **2018**, *65*, 3885–3896. [CrossRef]
21. Jun, J.; Bae, S.; Lee, Y.; Kim, C. A Spread Spectrum Clock Generator With Nested Modulation Profile for a High-Resolution Display System. *IEEE Trans. Circuits Syst. II Express Briefs* **2018**, *65*, 1509–1513. [CrossRef]
22. De Caro, D.; Tessitore, F.; Vai, G.; Imperato, N.; Petra, N.; Napoli, E.; Parrella, C.; Strollo, A.G. A 3.3 GHz Spread-Spectrum Clock Generator Supporting Discontinuous Frequency Modulations in 28 nm CMOS. *IEEE J. Solid-State Circuits* **2015**, *50*, 2074–2089. [CrossRef]
23. Hwang, S.; Song, M.; Kwak, Y.; Jung, I.; Kim, C. A 3.5 GHz Spread-Spectrum Clock Generator With a Memoryless Newton-Raphson Modulation Profile. *IEEE J. Solid-State Circuits* **2012**, *47*, 1199–1208. [CrossRef]
24. *Spread Spectrum Clocking Using the CDC5502/503*; Application Note SCAA103; Texas Instruments: Dallas, TX, USA, 2009.
25. *STM32 MCUs Spread-Spectrum Clock Generation Principles, Properties and Implementation*; Application Note AN4850; STMicroelectronics: Geneva, Switzerland, 2016.
26. *R12755 Series, 30V, 2A, Synchronous PWM Step-Down DC/DC Converter*; Ricoh Electronic Devices Co. Ltd.: Tokyo, Japan, 2018.
27. Multiphase Oscillator with Spread Spectrum Frequency Modulation, Document LTC6902, Linear Technology, 2003. Available online: <http://cds.linear.com/docs/en/datasheet/6902f.pdf> (accessed on 19 December 2019).
28. Callegari, S.; Rovatti, R.; Setti, G. Spectral properties of chaos-based FM signals: theory and simulation results. *IEEE Trans. Circuits Syst. I Fundament. Theory Appl.* **2003**, *50*, 3–15. [CrossRef]
29. Setti, G.; Balestra, M.; Rovatti, R. Experimental verification of enhanced electromagnetic compatibility in chaotic FM clock signals. In Proceedings of the 2000 IEEE International Symposium on Circuits and Systems (ISCAS), Geneva, CH, 28–31 May 2000; Volume 3, pp. 229–232.
30. Ktse, K.; Chung, H.S.; Hui, S.Y.R.; So, H.C. A comparative study of carrier-frequency modulation techniques for conducted EMI suppression in PWM converters. *IEEE Trans. Ind. Electron.* **2002**, *49*, 618–627.
31. Lauder, D.; Moritz, J. *Investigation into Possible Effects Resulting From Dithered Clock Oscillators on EMC Measurements and Interference to Radio Transmission Systems*; Radiocommunications Agency: London, UK, March 2000.
32. Hardin, K.; Oglesbee, R.A.; Fisher, F. Investigation into the interference potential of spread-spectrum clock generation to broadband digital communications. *IEEE Trans. Electromagn. Compatibil.* **2003**, *45*, 10–21. [CrossRef]
33. Mukherjee, R.; Patra, A.; Banerjee, S. Impact of a Frequency Modulated Pulsewidth Modulation (PWM) Switching Converter on the Input Power System Quality. *IEEE Trans. Power Electron.* **2010**, *25*, 1450–1459. [CrossRef]
34. Skinner, H.; Slattery, K. Why spread spectrum clocking of computing devices is not cheating. In Proceedings of the 2001 IEEE EMC International Symposium. Symposium Record. International Symposium on Electromagnetic Compatibility (Cat. No.01CH37161), Montreal, QC, Canada, 13–17 August 2001.
35. Musolino, F.; Crovetto, P.S. Interference of Spread-Spectrum Switching-Mode Power Converters and Low-Frequency Digital Lines. In Proceedings of the 2018 IEEE International Symposium on Circuits and Systems (ISCAS), Florence, Italy, 27–30 May 2018; pp. 1–5.
36. Matsumoto, Y.; Shimizu, T.; Murakami, T.; Fujii, K.; Sugiura, A. Impact of Frequency-Modulated Harmonic Noises From PCs on OFDM-Based WLAN Systems. *IEEE Trans. Electromagn. Compatibil.* **2007**, *49*, 455–462. [CrossRef]
37. Musolino, F.; Crovetto, P.S. Interference of Spread-Spectrum Modulated Disturbances on Digital Communication Channels. *IEEE Access* **2019**, *7*, 158969–158980. [CrossRef]
38. Shim, H.; Hubing, T.H. A closed-form expression for estimating radiated emissions from the power planes in a populated printed circuit board. *IEEE Trans. Electromagn. Compatibil.* **2006**, *48*, 74–81. [CrossRef]
39. Zeeff, T.M.; Hubing, T.H. Reducing power bus impedance at resonance with lossy components. *IEEE Trans. Adv. Pack.* **2002**, *25*, 307–310. [CrossRef]
40. Grassi, F.; Spadacini, G.; Marliani, F.; Pignari, S.A. Use of Double Bulk Current Injection for Susceptibility Testing of Avionics. *IEEE Trans. Electromagn. Compatibil.* **2008**, *50*, 524–535. [CrossRef]

41. Crovetto, P.S.; Fiori, F. Distributed Conversion of Common-Mode Into Differential-Mode Interference. *IEEE Trans. Microw. Theory Tech.* **2011**, *59*, 2140–2150. [[CrossRef](#)]
42. Crovetto, P.S. Finite Common-Mode Rejection in Fully Differential Nonlinear Circuits. *IEEE Trans. Circuits Syst. II Express Briefs* **2011**, *58*, 507–511. [[CrossRef](#)]
43. Shannon, C.E. A Mathematical Theory of Communication. *Bell Syst. Tech. J.* **1948**, *27*, 379–423. [[CrossRef](#)]



© 2020 by the authors. Licensee MDPI, Basel, Switzerland. This article is an open access article distributed under the terms and conditions of the Creative Commons Attribution (CC BY) license (<http://creativecommons.org/licenses/by/4.0/>).

Article

Signal Transformations for Analysis of Supraharmonic EMI Caused by Switched-Mode Power Supplies

Leonardo Sandrolini ^{1,*} and Andrea Mariscotti ²

¹ Department of Electrical, Electronic and Information Engineering (DEI), University of Bologna, 40126 Bologna, Italy

² Department of Electrical, Electronics and Telecommunication Engineering and Naval Architecture (DITEN), University of Genova, 16145 Genova, Italy; andrea.mariscotti@unige.it

* Correspondence: leonardo.sandrolini@unibo.it; Tel.: +39-051-2093-484

Received: 31 October 2020; Accepted: 4 December 2020; Published: 7 December 2020

Abstract: Switched-Mode Power Supplies (SMPSs) are a relevant source of conducted emissions, in particular in the frequency interval of supraharmonics, between 2 kHz and 150 kHz. When using sampled data for assessment of compliance, methods other than Fourier analysis should be considered for better frequency resolution, compact signal energy decomposition and a shorter time support. This work investigates the application of the Wavelet Packet Transform (WPT) and the Empirical Mode Decomposition (EMD) to measured recordings of SMPS conducted emissions, featuring steep impulses and damped oscillations. The comparison shows a general accuracy of the amplitude estimate within the variability of data themselves, with very good performance of WPT in tracking on stationary components in the low frequency range at some kHz. WPT performance however may vary appreciably depending on the selected mother wavelet for which some examples are given. EMD and its Ensemble EMD implementation show a fairly good accuracy in representing the original signal with a very limited number of base functions with the capability of exploiting a filtering effect on the low-frequency components of the signal.

Keywords: electromagnetic compatibility; conducted emissions; Discrete Wavelet Transform; electromagnetic interference; Empirical Mode Decomposition; harmonics; Switched-Mode Power Supplies; transients; Wavelet Packet Transform

1. Introduction

The widespread use of Switched-Mode Power Supplies (SMPSs) can be justified with flexibility, portability and better efficiency, including superior voltage regulation at the dc load. SMPSs feature various types of power electronic converters topologies, with conducted emissions that need to be assessed over a wide frequency range [1]. Conducted emissions caused by the switching process, in fact, originate from switching fundamentals of some tens of kHz and spread in the hundreds kHz and MHz ranges, well above the “classical” interval of harmonic and interharmonic penetration studies, limited in general to some kHz for 50–60 Hz systems. In the last ten years, attention has been extended to frequency intervals below 150 kHz [2–9], in general not currently regulated by electromagnetic compatibility (EMC) standards, focusing on the so-called “supraharmonics”. Some standards [10–14] deal with the 2–150 kHz interval, but do not cover explicitly SMPSs and other similar switching converters, thus taking into account the characteristics of the related signals. The approach of EMC standards to the quantification of conducted emissions is quite similar above and below 150 kHz: resolution bandwidth of 9 kHz and frequency sweep by a spectrum analyzer or EMI receiver is the reference approach. However, the use of time-domain sampling is a valid alternative for the many data acquisition boards and digital sampling oscilloscopes available, for the possibility of inspecting the

“real” waveform when cross-checking the final results (especially in case of noncompliance) and the possibility of changing and tuning the post-processing methods.

The most popular of these methods is the spectrum calculation by Fourier transform (a Discrete Fourier Transform (DFT) or a Short-Time Fourier Transform (STFT), tracking Fourier spectrum versus time): it is a well-known technique that can be mastered after some practice, but may in reality lead to some disappointment, especially in the case of transient signals with a short time support [15], as it briefly pointed out in Section 2. Alternative methods better suited to handle signals characterized by transients may be considered: wavelets with the Wavelet Packet Transform (WPT) [16–22] and the Empirical Mode Decomposition (EMD), in the Ensemble EMD (EEMD) implementation [23–26] (to avoid the EMD shortcomings, as shown in Section 2). Although they have both been extensively described in the literature and the former applied often to Power Quality analysis, the considered problem is peculiar in two aspects:

- The investigated methods must provide accurate results in terms of amplitude of the signal components that may be compared to existing or future emission limits, in order to assess compliance and related margins. Several wavelet applications do not discuss the amplitude accuracy in the presence of both narrowband and broadband components, as well as of significant variability of the instantaneous frequency.
- They must support the analysis of the signal and of the control measures necessary in the case of noncompliance, with clear relationship with the internal sources and switching mechanisms, as well as also being easily interpretable, at least for the most relevant components critical for compliance to limits.

Modern controllers for switching converters adopt smart modulation techniques to improve efficiency, reduce voltage stress on components and reduce EMI. They are able to rapidly switch between different modulation patterns, each optimized for a range of operations and possibly with different spectral signatures: this opens the door to potential non-stationarity of the signal and the need to adopt short time windows, unsuitable for a Fourier-based approach.

Traditional EMC techniques based on frequency sweep have fallen behind the technological development in some sectors, such as power transfer and conversion [27], as well as in the presence of significant transients as the first source of emissions [28]. They would benefit from time–frequency analysis methods that are computationally attractive and preserve the accuracy necessary for the assessment of compliance. The focus is on amplitude accuracy, with the frequency estimate used only to locate suitable limit values and track component behavior. The definition of a reference case for comparison is particularly challenging, as discussed in Section 3.

This work describes the setup and measurement methods in Section 2. Then, after a synthetic description in Section 3 of the WPT and EMD transforms (with a comparison between EMD and EEMD), results are compared and discussed in Section 4.

2. Measurement Setup and Signal Transformations

2.1. Measurement Setup

The signals considered in this work are the conducted emissions of SMPSs connected to the AC mains through a Line Impedance Stabilization Network (LISN). The output of the LISN is fed to an 8-bit DSO with a sampling rate of 10 MSa/s, to keep records to a manageable size for later post-processing. Frequency domain sweeps can be carried out as well by means of an EMI receiver, to use as reference in case of need. The scheme of the setup is shown in Figure 1.

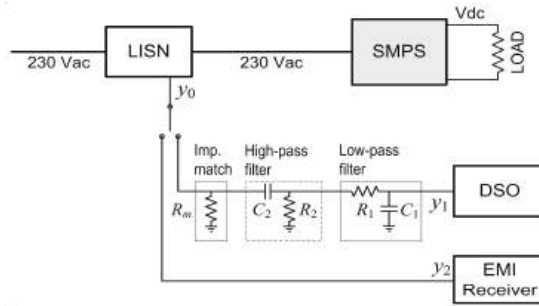


Figure 1. Scheme of the experimental setup: SMPS under test and its dc variable load, LISN (Line Impedance Stabilization Network), 50 Ω impedance matching, high-pass filter (1 kHz cutoff) and low-pass filter (2 MHz cutoff), Digital Storage Oscilloscope (DSO) and EMI Receiver.

An anti-aliasing low-pass filter with a cutoff frequency of 2 MHz is used to feed the DSO: the resistor R_2 is 5 kΩ and the capacitance C_2 is the internal input capacitance of the DSO, equal to 15 pF with good accuracy. A high-pass filter with a cutoff frequency of 1 kHz is also included for additional attenuation of the fundamental and the 100 Hz ripple component possibly leaking through the LISN: the resistor $R_1 = 1.5$ kΩ is large enough to be neglected in parallel to the impedance-matching 50 Ω resistor R_m , giving a neat 100 nF for C_1 to get the desired 1 kHz cutoff.

The tested SMPSs are all AC/DC low-voltage switching converters with a 5 V or 12 V nominal dc output and a power level in the range of some tens of W. This allowed the use of a 16 A LISN and no major issues of heating and high-voltage hazards; it is not likewise a limiting factor, since it is expected that smaller converters will show the most rapid switching transients. As a matter of fact, the observed switching frequency values are in the range of some tens of kHz, in line with the dynamics of controllers and MOS transistors available about ten years ago.

The switching byproducts responsible for the conducted emissions are superimposed to the mains sinusoidal voltage, located at its zero crossings. The signal y_1 at the DSO input (qualitatively similar to the signal y_0 as provided at the LISN output) is an intermittent waveform, deprived of the 50 Hz mains voltage component and of its low-order harmonics, also to improve the dynamic range. The zero-mean high-pass filtered signal is characterized by steep transients and rapid oscillations, as shown in Figure 2. The instantaneous frequency of oscillations is in the order of 20–30 kHz and is in relation to the internal switching frequency; the repetition rate is 100 Hz, twice the mains frequency.

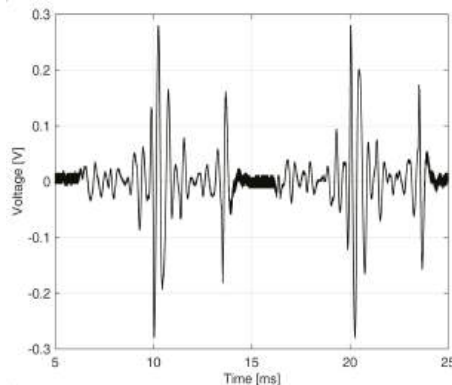


Figure 2. Typical time-domain waveform of an SMPS at the high-pass filtered LISN output measured as DSO input signal y_1 .

2.2. Use of the Discrete Fourier Transform (DFT)

The Fourier-based analysis, for simplicity gathered under the abbreviation DFT, is assumed well known and is not repeated. As seen, the signal is characterized by bursts with oscillations at low and high frequency of limited duration. The use of DFT applied to this kind of intermittent rapidly varying signals has the following drawbacks:

- The signal portion to analyze has a short duration, which contrasts to the desirable or required frequency resolution. The IEC 61000-4-7 standard [29] indicates an observation time of 200 ms that is clearly inadequate (equivalent to 5 Hz resolution, suitable for low frequency harmonics, but not for phenomena at higher frequency with fast dynamics, as in the present case). The EN 55065-1 [14] and in general EMC standards for conducted emissions below 150 kHz require a 200 Hz resolution bandwidth. A more suitable approach has been proposed in the IEC 61000-4-30 [13], defining a frequency resolution of 2 kHz, which goes in the direction of tracking signals with fast dynamics, as in the present case.
- To avoid spectral leakage, the signal should be cut in the zero-valued short intervals between pulses, implying a resolution frequency of about 100 Hz. Other window intervals will suffer from spectral leakage, only partly attenuated by the use of tapering windows.
- Using a long window interval has the drawback of averaging the contribution of the contained signal components, largely reducing the estimated amplitude of the peak located at the center.
- Using a short window interval reduces the frequency resolution and worsens the spectral representation and the estimate of the amplitude, this time caused by the short-range spectral leakage (or “picket fence effect”), if no additional post processing is used.

For all the reasons above and as justified in the Introduction, alternative signal transformations should be investigated for applicability to the present case, providing spectral representations in a domain (or combination of domains, e.g., time and frequency) that can still be interpreted and used to evaluate the degree of compliance, as for conducted emissions in the aforesaid 2–150 kHz interval. Wavelets have been extensively applied for accurate PQ analysis in the harmonic low-frequency range [1,16,18–21], as effective alternative method for compliance to the IEC 61000-4-30 processing requirement and for detection of transient PQ phenomena (e.g., voltage sags, overvoltages, etc.) [17], the latter without the analysis of the accuracy of the parameters estimate. EMD and EEMD find their application in the analysis of seismic data, vibrations, speech signals and medical data [23–25], but lack a clear quantification of component amplitude to support comparison with limits and susceptibility criteria, defined in the frequency domain. Rather their typical application is more oriented to the detection and identification of signal features and components hidden by noise and signal compression.

2.3. Wavelet Packet Transform (WPT)

Oppositely to the DFT with its stationary sinusoidal kernel, wavelet analysis relies on short-duration oscillating waveforms that have zero mean and decay rapidly to zero at both ends [16]. Dilation and shifting of kernel waveforms allow adapting it for variable time and frequency resolution. Since its first inception, wavelets have been proposed in both wavelet function and multistage filter bank implementations. The filter bank was built using low-pass (LP) and high-pass (HP) complementary filters (for reference, they can be created as “quadrature mirror filters”) [16,18]. The first implementation (Discrete Wavelet Transform (DWT)) applied recursively the LP and HP filters of the successive stage only to the LP output of the previous stage, and so on. The Wavelet Packet Transform (WPT) uses then a symmetrical structure, applying the decomposition to both LP and HP outputs, as shown in Figure 3, which allows a linear, rather than logarithmic, apportionment of the frequency axis, and thus a linear decomposition of the signal spectrum. This is inline with the 2 kHz group representation uniformly spread over the frequency axis suggested by the EN 61000-4-30 [13]. At each stage, the outputs of the LP and HP filters are named “approximation” and “detail”, respectively.

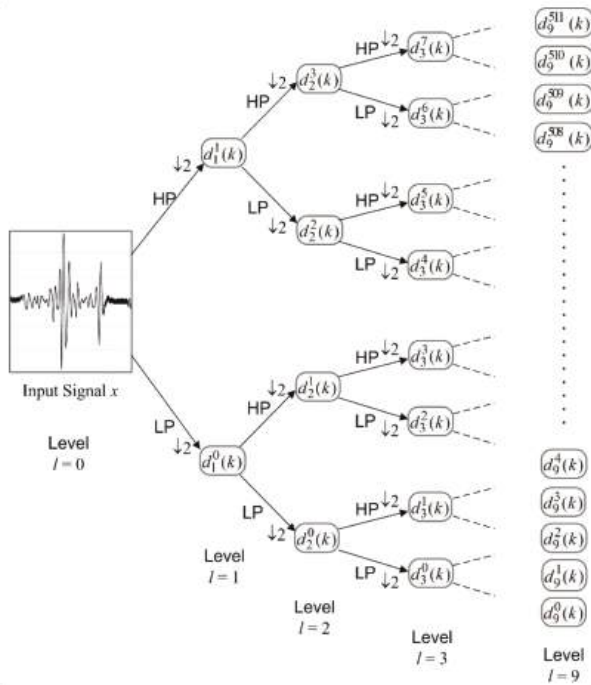


Figure 3. WPT (Wavelet Packet Transform) tree structure, indicating levels, ordinal indices at each level and terminal nodes. The down arrow “↓*n*” indicates a down sampling (or decimation) by a factor of *n* (in our case, *n* = 2).

The output of the WPT decomposition is used for a compact spectrum estimate focused on the determination of three elements: the amplitude of the component, its location on the frequency axis and its location on the time axis (or duration). The STFT addresses this third point by assigning a window length and the amount of overlap between successive windows sliding over the signal along the time axis.

The WPT spectrum estimate is built on the “details” of the terminal nodes, which are in a number $N = 2^L$, where L is the number of chosen levels. Details are denoted as $d_l^p(k)$, where l indicates the level ($l = 0, 1, \dots, L$, level 0 being the original signal x), p is the position along the row of nodes in the tree at the same level ($p = 0, 1, \dots, 2^l$) and k is a “time” index (the position along the sequence of data samples). Each detail in fact apportions the original signal of length M over the N nodes at a given level with data sequences of length M/N ; the lower in the tree, the higher the level l and the number of nodes ($N_l = 2^l$), and the shorter the length of each sequence $K = M/2^l$. Each data sequence contained by a detail (for ease of understanding, we consider the last and deeper level, i.e., the terminal nodes) is a sub-band representation of the original signal: the bandwidth, or frequency resolution, Δf is derived from the original sampling f_s as $\Delta f = f_s/2^{L+1}$, and in general $\Delta f_l = f_s/2^{l+1}$. In our case with a downsampled version of the raw data using $f_s = 1 \text{ MSa/s}$ and $L = 9$, we obtain $\Delta f = 976 \text{ Hz}$, which matches the selected RBW for the EMI receiver data used for comparison in Section 3.

To the aim of the quantitative assessment of the accuracy of WPT spectrum estimate, the amplitude of the components of the spectral representation must be derived: the Matlab function `wpspectrum()` gives such time–frequency representation, where time and frequency resolutions Δt and Δf are determined by the selected number of levels L and the original sampling f_s .

The problem is to understand the unity of measure and the meaning of the spectrum values (pixels, or tiles) in terms of the original quantities; in other words, WPT spectrum extraction needs to be “calibrated” in order to be used as an EMI assessment tool.

Given the details as sub-banded data sequences, the calculation of the total rms value gives straightforwardly a measure of the power contained in each sub-band p (the notation $l = L$ in (1) indicates that the expression is general for whatever l , but we select in the following $l = L$, so that the terminal nodes give the desired frequency resolution).

$$\tilde{x}_{p,l=L} = \sqrt{\frac{\sum_k (d_{l=L}^p(k))^2}{N_{l=L}}} \quad (1)$$

Of course, rms values from adjacent sub-sequences may be aggregated with a concept of overall rms in a wider band, made of the composition of each respective Δf_l^p (the sub-band of order p at the level l). Being rms values interpreted in a power perspective, such aggregation is performed by rms summation over the sub-sequences $d_L^p(k)$ with p in the selected α set (written as p_α).

$$\tilde{x}_{[p_\alpha],L} = \sqrt{\frac{\sum_\alpha \sum_k (d_L^{p_\alpha}(k))^2}{N_L}} \quad (2)$$

To exemplify, to make an approximately 2 kHz representation from the $\Delta f = 976$ Hz representation, two adjacent sub-bands must be aggregated, discarding the first one that contains the dc component. Thus, the p indices would start from 1 and go in pairs: (2,3), (4,5), (6,7), etc. A bandwidth of approximately 3 kHz is obtained by grouping with a ratio of 3, so (2,3,4), (5,6,7), etc.

2.4. Empirical Mode Decomposition (EMD) and Ensemble Empirical Mode Decomposition (EEMD)

The Empirical Mode Decomposition (EMD) was proposed for attractive characteristics: the transformation is based on simple operations (and should be relatively light computationally), its results can be clearly interpreted and it is robust, thus there are no wide or uncontrolled variations of the results for small changes of the parameters.

The EMD was developed to prepare the data to which the Hilbert Transform (HT) could be applied; the combination of EMD and HT is the Hilbert-Huang Transform (HHT), which provides a powerful tool for nonlinear and nonstationary signal processing. The signal is decomposed adaptively into a finite (often small) number of the so-called Intrinsic Mode Functions (IMFs), not known a priori (differently than in the Fourier or Wavelet analysis), which represent the oscillation modes embedded in the data. With the HT, the IMFs yield instantaneous frequencies as functions of time. Each IMF satisfies the following two conditions:

- In the whole dataset, the number of extrema and the number of zero crossings is either equal or differ at least by one.
- At any point, the mean value of the envelope defined by local maxima and local minima is zero.

The iterative process of extraction of the IMFs through the EMD method is called the sifting process. The first IMF contains the highest oscillation frequency in the signal. The difference between the original signal and the first IMF is called a residue. The residue is then considered as new data to decompose and the sifting process is applied to it; the same definition thus applies to the difference between the previous residue and the last IMF at later stages. The sifting process must be repeated until the extracted signal (the candidate IMF) satisfies the IMF definition or the predefined maximum number of iterations is exceeded. The number of extrema decreases as the decomposition proceeds, and the sifting process ends when the residue becomes a monotonic function or a function with only one extremum from which no further IMF can be extracted [23] (in other words, no oscillations are

contained in the residue). At the end of the decomposition, we have N IMF functions and one residue, and the original signal $x(t)$ can be reconstructed as

$$x(t) = \sum_{i=1}^N c_i(t) + r(t) \quad (3)$$

where c_1 and c_N are the highest and lowest frequency IMFs, respectively, and $r(t)$ is the residue. Besides the harmonic content, IMFs are characterized by different amplitudes. The original signal may then be fairly approximated by using only a limited set of the IMFs, i.e., those with the largest amplitudes only.

The major drawback of the EMD method is mode mixing, for which the EEMD method was introduced [26]. Mode mixing means that different modes of oscillations coexist in the same IMF. EEMD (Ensemble EMD) consists in adding white noise to the original signal. This procedure is run for a number of times, thus an ensemble of datasets with different added white noise is generated. The new obtained data are then decomposed into IMFs with the sifting procedure. Being the added noise different in each run, the IMFs of the various runs are uncorrelated. Averaging the IMFs eliminates the added noise and yields then the final result. The truth IMF, $c_j(t)$, defined by EEMD is then obtained for an ensemble number approaching infinity:

$$c_j(t) = \lim_{N \rightarrow \infty} \sum_{k=1}^N c_{jk}(t) \quad (4)$$

where

$$c_{jk}(t) = c_j(t) + r_{jk}(t) \quad (5)$$

is the k th trial of the j th IMF in the noise added signal, being $r_{jk}(t)$ the contribution from the added white noise of the k th trial to the j th IMF. To minimize the difference between the truth IMF $c_j(t)$ and the IMF $c_{jk}(t)$ obtained with N trials, N must be large, as for the well-known statistical rule the difference between the truth and the result of the ensemble for a finite number of elements of the ensemble decreases as $1/\sqrt{N}$.

EEMD represents a major improvement to EMD as it eliminates mode mixing; however, the major drawback is that the result of EEMD does not strictly satisfy the definition of IMF, as the sum of IMFs is not necessarily an IMF. A possible solution to this problem is to apply EMD to the IMFs produced by EEMD.

3. Results

3.1. Introduction and Reference Case

Regarding the accuracy of the estimated amplitude, it is difficult to establish a reference case for this kind of signals. In other words, what is the real amplitude of the spectrum components of the signal?

The STFT gives a first indication, although the amplitude is highly variable, as a function of the frequency resolution, its implicit averaging and the amount of spectral leakage depending on the characteristics of the adopted tapering window.

It may be objected that an EMI receiver scan returns the reference spectrum, since after all it is the reference method adopted by EMC standards, against which we check the compliance of emissions. The "EMC" resolution bandwidth (RBW) values of 200 Hz and 9 kHz used, respectively, below and above 150 kHz have been considered as a starting point, assessing the variability of the measured spectrum by changing RBW from 200 Hz to 1 kHz, 2 kHz, 3 kHz and 5 kHz, looking for a compromise between a neat frequency resolution and an accurate amplitude estimate. The results are reported in Figure 4 showing a progressive increase of the noise floor (as expected), a substantially stable amplitude

of the switching peaks at 43.3 kHz and 87 kHz and above, and a variable estimated amplitude for the low-frequency nonstationary components (with a behavior similar to that of background noise). The result with 1 kHz RBW is retained for further analysis as a good compromise, also in view of the necessary time resolution settings in STFT and WPT.

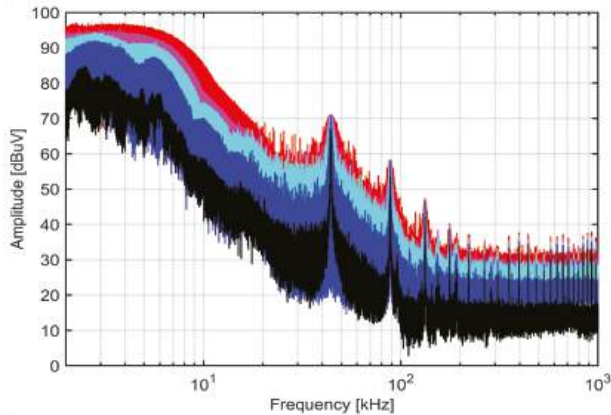


Figure 4. EMI receiver spectra with variable RBW (200 Hz, black; 1 kHz, blue; 2 kHz, light blue; 3 kHz, magenta; 5 kHz, red) for a SMPS featuring fixed switching frequency (type Black at 90% of rated power).

A slower narrow-RBW scan should be used instead (e.g., with RBW = 10 Hz or 30 Hz): the dynamic range will be maximized and, using the “max hold” setting at each frequency bin (or step), it is ensured that the repeatability of the measurement is also maximized. However, such setting is quite far from those used for measurement of emissions and the necessary scan time is extremely long (about 8 h), yielding issues of long-term stability of the setup.

3.2. Performance of WPT

3.2.1. Basic Time and Frequency Resolution Performance of WPT

The time resolution of both WPT spectra in Figure 5b,c is superior to that of STFT tracking the signal with 500 μ s and 125 μ s steps, respectively; considering the visible signal dynamics and what is offered by alternative approaches (such as a narrowband DFT or a real-time spectrum analyzer), a time step in this range is more than adequate. Correspondingly, the frequency resolution also varies by a factor of 4 in the opposite direction: when using 976 Hz in Figure 5b, the low-frequency portion of the spectrum is enriched with the details between the second and the sixth bin, which hold alternatively the maximum of the spectrum around $t = 5$ ms; this is evident from the asymmetry of the half-cycles of the oscillatory spike in the center of the waveform of Figure 5a. The comparison of the estimated amplitudes for the two spectra with different frequency and time resolution indicates that a finer time resolution gives slightly larger amplitudes (Figure 5c), avoiding the averaging implicit in a larger time interval. This behavior is common with the DFT and is hardly predictable quantitatively, as it depends on the characteristics of the signal components (narrowband/broadband and steady/transient). The average of four adjacent time bins in Figure 5c gives approximately the value of one bin of Figure 5b (within 1 dB). Nonetheless, the maximum value can differ by up to 3.4 dB, as occurring in the first frequency bin at 5 ms; this represents then the maximum absolute error between the two spectral representations.

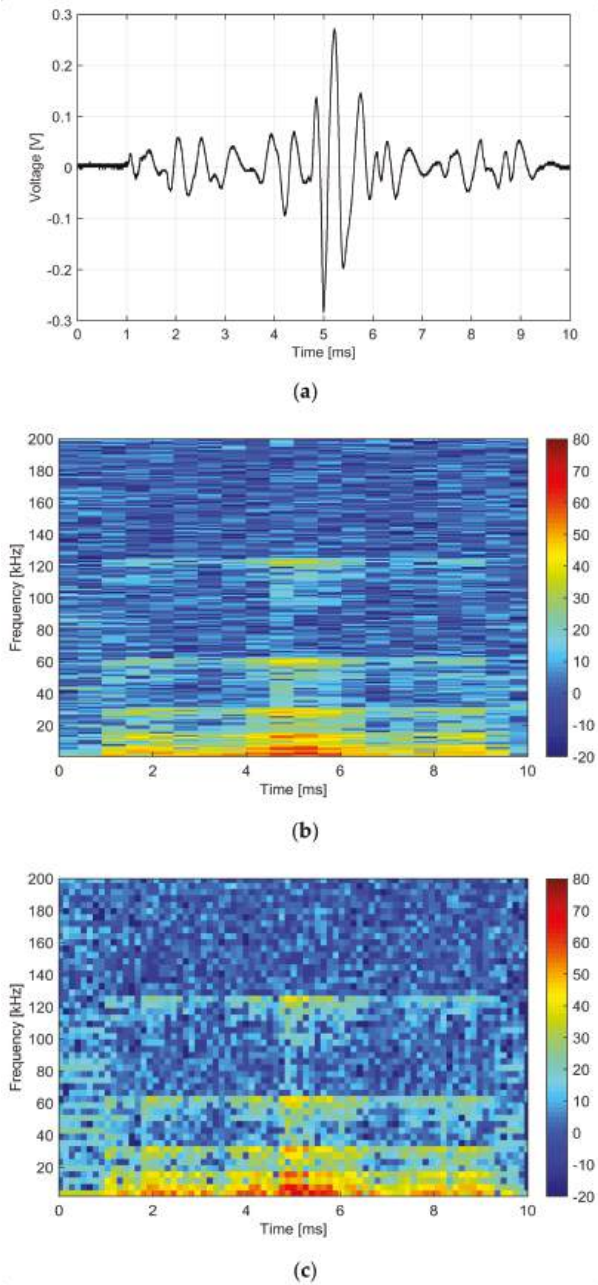


Figure 5. WPT spectrum in dB μ V/Hz (normalized by frequency resolution). An example of change of dilation in time and frequency by a factor of 4 with *symlet1* wavelet: (a) signal waveform (10 MSa/s); (b) *symlet1* with $L = 9$ levels and a downsampling of $q = 10$; and (c) *symlet1* with $L = 8$ levels and $q = 5$. SMPS type Black at 25% of rated power.

The case of two different wavelets is shown in Figure 6, applied to the signal using the same scaling: the amplitude estimates are quite similar, with the *bior1.3* in Figure 6b, showing slightly smoother amplitude profile than the *symlet1*. Quantitatively, the average difference for the bins with the largest amplitude (those in Figure 6 with amplitude above 50 dB) is only 1.3 dB; the peaks, which are the most relevant for compliance to limits, are reproduced quite reliably with almost identical values (average difference of less than 0.25 dB). Thus, at least for the considered case, the choice of wavelets with “similar” characteristics and of suitable order for the observed time support gives repeatable results, although it represents a source of systematic error and the contribution to the uncertainty of the estimate of spectrum amplitude is not negligible (0.25 dB on average for the considered case).

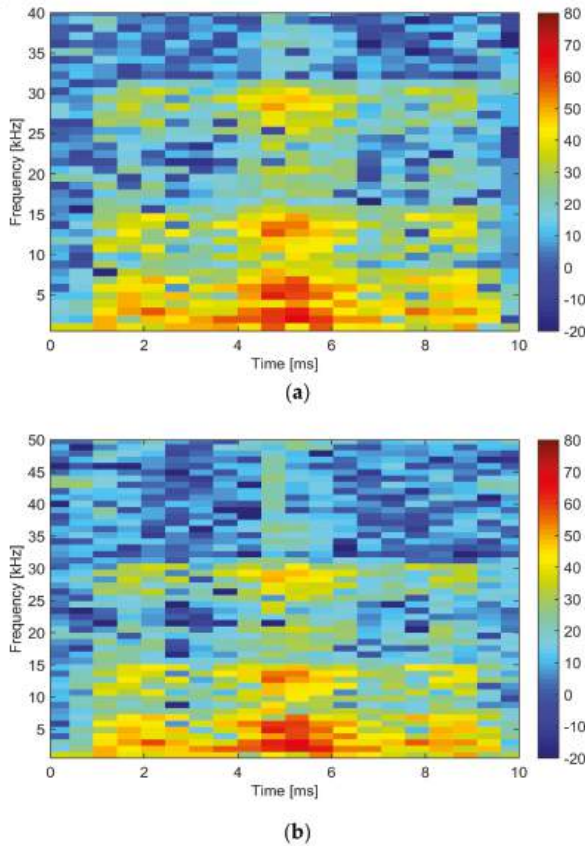


Figure 6. (a) Zoom on the frequency axis of Figure 5b for the frequency resolution of 976 Hz, where the change of the instantaneous frequency between 4 and 6 ms is well visible; and (b) additional spectrum obtained by replacing *symlet1* with *bior1.3*.

The compactness in time and frequency was evaluated considering two wavelets extensively used for PQ studies, the *db15* (equivalent to the *db20*) and the *sym8*. The results shown in Figure 7 (for the SMPS type Black at 90% of the rated power) reveal that *sym8* has some spectral leakage at the occurrence of the two peaks of the signal, at 1 ms and 4.5 ms; *db15* instead shows a limited increase of some scattered components without any visible burst of spectral leakage. Regarding the low frequency components, *db15* also shows a more coherent behavior where the second frequency bin keeps the lead

for 2 ms giving yield then to fourth bin, with a return around 4 ms. Behavior of *sym8* instead is more chaotic with no definite bin prevailing for at least some ms.

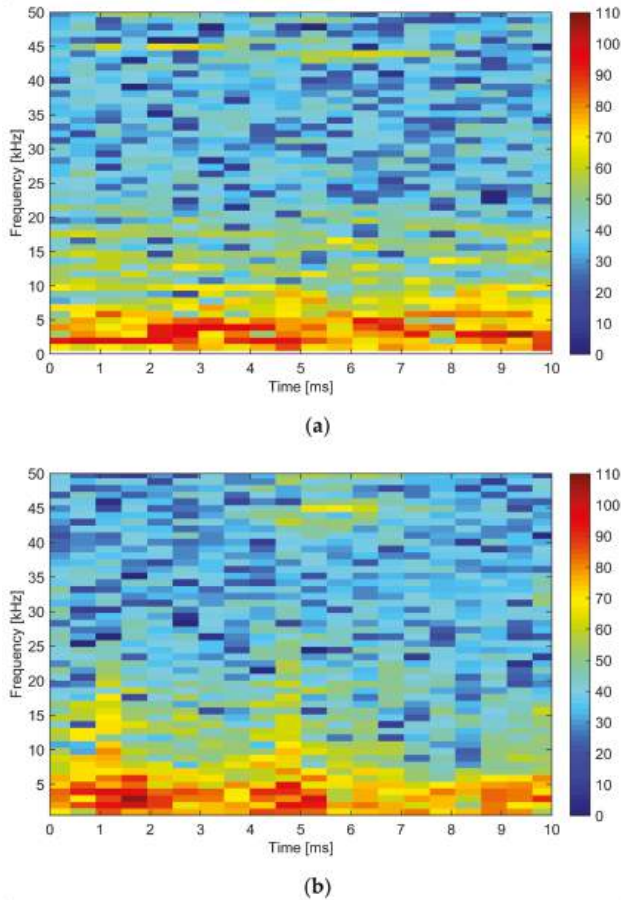


Figure 7. Comparison of two different wavelets in relation to localization on the time axis and spread to adjacent frequency bins; frequency resolution $\Delta f = 976$ Hz, number of levels $L = 9$: (a) *db15*; and (b) *sym8*. SMPS type Black at 90% of rated power.

As observed for the EEMD in Section 3.3, the best amplitude accuracy is reached for the faster components (those at about 44 and 88 kHz) that have better localization in both time and frequency: in this case, agreement for different frequency and time resolutions is within 0.6 dB for the results shown in Figure 5 (confirmed by some other tests done on different SMPSs). For nonstationary low-frequency components, the reference measurements themselves for assessment of accuracy are deemed by variability and uncertainty caused by the very nature of the signals.

3.2.2. Amplitude Accuracy and Spectrum Representation of WPT

The WPT behavior for the SMPS with constant switching frequency (named “Black” SMPS in the following) is analyzed showing the elements that concur to determine the amplitude accuracy.

As introduced in Section 2.3, the WPT spectra built with `wpspectrum()` is artificially adjusted so that the local intensity of each tile can be evaluated standalone. The adjustment consists in the

multiplication by the square root of the number a of tiles in the time direction ($a = 20$ in the present case) that is re-absorbed when aggregating in the rms sense all such tiles for each frequency bin to recover its rms, which for single tone calibration signals corresponds to the rms amplitude of the test signal itself.

The results of a comparison with STFT with 1 kHz frequency resolution and calculated using the Flat Top window are shown in Figure 8.

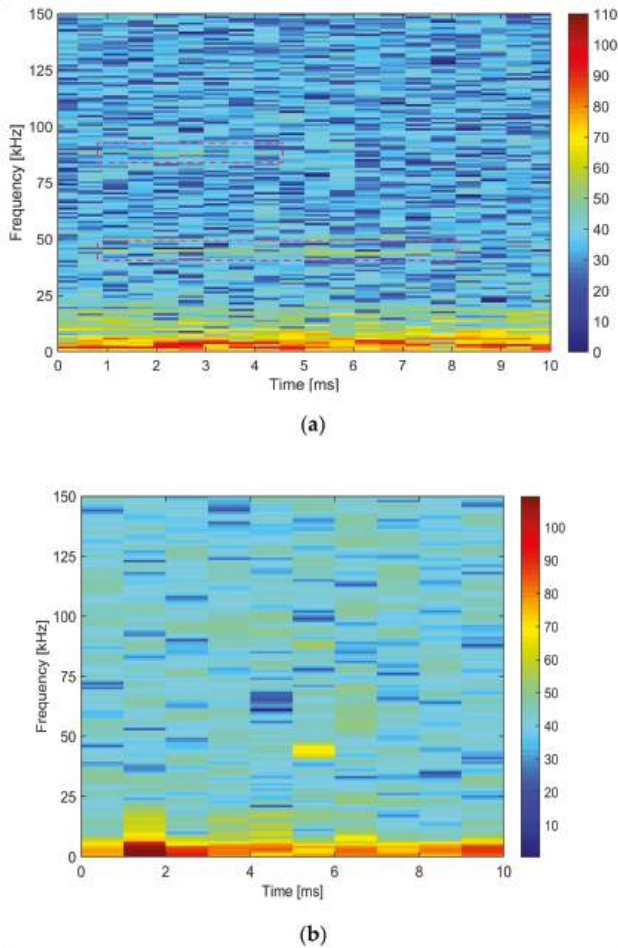


Figure 8. Black SMPS tested at 90% of rated power: (a) WPT spectrum obtained with $db15$, $L = 9$, $\Delta f = 976$ Hz; and (b) STFT spectrum with $\Delta f = 1$ kHz and time step $\Delta t = 1$ ms.

The two areas encircled by the pink rectangles are those of the 44 kHz and 88 kHz components, for which the WPT provides a thorough tracking (see Figure 8a), better than that appearing in the STFT spectrum (Figure 8b). The comparison between WPT spectrum and STFT shown in Figure 8 reveals that:

- WPT frequency resolution is superior, in terms of spectrum details and reduced leakage, which instead affect the STFT results (see, for instance, the central portion of the spectrum between 4 ms and 6 ms and the dynamic range of more than 30 dB for the background components (blue to light blue color)).
- The time resolution is also superior with the ability of tracking more closely signal dynamics.

- Regarding amplitude accuracy, we must distinguish between: (i) For narrowband switching components visible at 44 kHz and 88 kHz, there is a general agreement among WPT, STFT and the EMI receiver scan in frequency domain. We must observe that the receiver scan was made for a time interval much longer than the one covered by WPT and STFT, so that using max hold slightly larger values may be expected. (ii) The low frequency components are a byproduct of the switching pulses and evidently the instantaneous frequency is slightly variable, as result of non-linearity during oscillations. WPT confirms good tracking of such components and averaged values over adjacent bins are quite stable with respect to different frequency resolutions Δf .

Table 1 reports the results of the assessment of the amplitude accuracy for the three most prominent frequency bins shown in the first column. Reported values are the maxima, in line with the use of Flat Top for the STFT and max hold for the EMI receiver.

Table 1. Comparison of amplitudes of main spectrum components calculated with WPT and STFT and measured with EMI receiver (using the 1 kHz RBW results in Figure 4).

Frequency (kHz)	EMI Rec. (dB μ V)	WPT (dB μ V)	STFT (dB μ V)
2–5	93.0	93.75–105.5 ⁽¹⁾	82.73–106.7 ⁽¹⁾
44	70.5	68.07, 71.51 ⁽²⁾	69.04
88	57.5	60.60 ⁽³⁾	53.27

⁽¹⁾ Range of maxima in the 2–4 kHz bins over 10 ms for 90% of bins; implicit averaging in this case is extremely important and WPT has the best resolution and the least averaging. ⁽²⁾ Five bins between 60.64 dB μ V and 65.87 dB μ V; with rms summation of adjacent bins carried out to cope with the 1 ms time resolution of the STFT, the results are 71.51 dB μ V and 68.07 dB μ V centered at 2.5 ms and 6.5 ms. ⁽³⁾ Two bins with 55.27 dB μ V and 53.83 dB μ V; with rms summation of adjacent bins carried out to cope with the 1 ms time resolution of the STFT, the result is 60.60 dB μ V centered at 2.5 ms.

3.3. EMD and EEMD Performance

The EMD and EEMD were used in the R interface implementation Rlibeemd [30,31]. The measured voltage is analyzed first using EMD. As the boundaries of the signal may affect the decomposition of EMD-based algorithms [32], to avoid boundary problems, particular care was taken in the choice of an appropriate time record of 10 ms. Figure 9 shows the 12 IMFs extracted from the original signal. As demonstrated in [33], the EMD performs as a filter-bank sifting out the high-frequency harmonics first, whereas the low-frequency ones pass through the filter. IMFs 2 and 3 contain the information needed to represent the significant part of the frequency spectrum, i.e., the three peaks corresponding to the switching frequency (about 44 kHz) of the SMPS and its second and third harmonics. IMF 2 contains the information related to the second and third harmonics of the fundamental frequency, whereas IMF 3 contains the information of the switching frequency. Performing a FFT on the sum of these two IMFs yields the red spectrum in Figure 10, whereas the blue spectrum is the FFT of the original signal. A Flat Top window is applied to the original signal and IMFs in order to maximize the amplitude estimate [15].

As shown in Figure 10, the three peaks are predicted with good accuracy, although there is a difference of about 1 dB with the FFT of the original signal for the peak at the fundamental frequency. Considering these two IMFs 2 and 3 only has the effect of filtering the low-frequency content of the measured voltage, which is collected in IMFs 4–13. IMFs 4 and 5 contain the information related to the 100 Hz ripple components (whose period corresponds to 10 ms, as shown in Figure 2). These IMFs are those with the largest amplitude and represent the low-frequency part of the signal in the frequency domain. IMFs 2–5 thus contain sufficient information to represent the signal, as shown in Figure 11. As can be seen, this spectrum slightly differs from the spectrum of the original signal up to 150 kHz. The fundamental, second and third harmonics are predicted with good accuracy with respect to the FFT of the original signal. Some information on the fundamental frequency may then be contained in IMFs 4 and 5 due to mode mixing, as mentioned in Section 2.4. Of course, the upper part of the frequency range is not predicted accurately, as the lowest order IMF (that containing the information on

higher frequencies) has not been considered. Nevertheless, the supraharmonics spectrum 2–150 kHz is well represented with just four IMFs obtained with EMD.

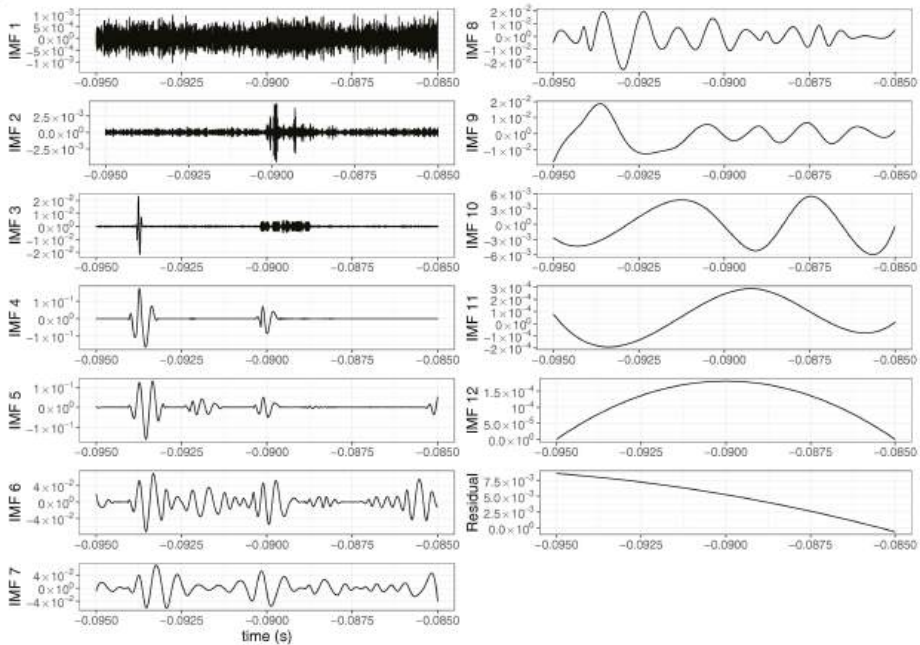


Figure 9. IMFs extracted with the EMD procedure.

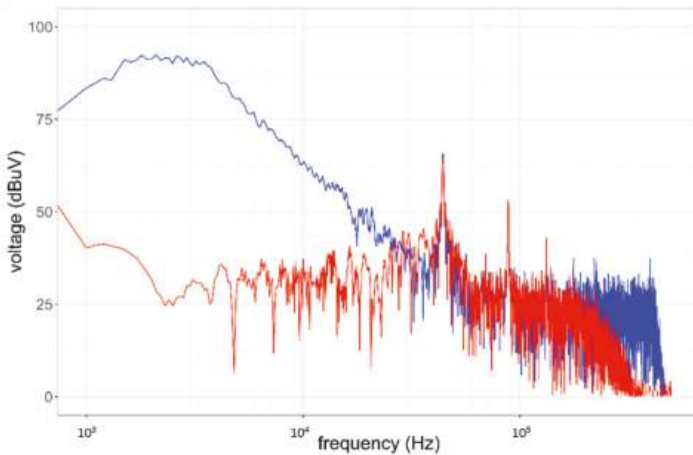


Figure 10. Comparison of the FFT spectra obtained from IMFs 2 and 3 extracted with EMD (red) and from the original signal (blue).

The application of the EEMD yields the same number of IMFs as EMD, 12, as shown in Figure 12. The information related to the 100 Hz ripple components is contained in IMFs 5–9, being IMFs 6 and 7 those with the largest amplitude. To represent the signal in the frequency domain, only IMFs 2–7 are needed. The high-frequency information of the signal is now distributed over three IMFs (IMFs 2–4), as shown in Figure 13. The accuracy with which the first two peaks are determined is very

good; however, although the amplitude of the third harmonic of the fundamental is predicted quite accurately, the noise floor beyond 100 kHz raises making it less clearly visible than in the case of the EMD. The filtering effect on the low-frequency components of the spectrum is still evident. By adding IMFs 5–7 and performing the FFT on the sum of these six IMFs, the red spectrum of Figure 14 is obtained, which is in fairly good agreement with that of the original signal.

By means of the application of FFT to the relevant modal components obtained with EMD, it is shown that the frequency extraction ability of the EMD is consistent and strong [34].

The results of comparison with STFT with 1 kHz frequency resolution, a 1 ms time step and a Flat Top window are shown in Figures 15 and 16. The former figure refers to the application of STFT to the signal obtained composing IMFs 2 and 3 extracted with EMD; the latter to the application of STFT to the signal obtained composing IMFs 2–4 extracted with EEMD. The amplitudes are the maximum values obtained by the successive FFTs that compose the STFT, as it would be with a spectrum analyzer set to max hold. It can be noticed that the amplitudes of the first peak (at 44 kHz, with 68.27 dB μ V and 69.97 dB μ V, respectively) and of the second peak (at 88 kHz, with 57.59 dB μ V and 58.51 dB μ V, respectively) are in agreement with those shown in Table 1 for WPT and EMI receiver data, thus confirming the suitability of the approach in the analysis of EMI.

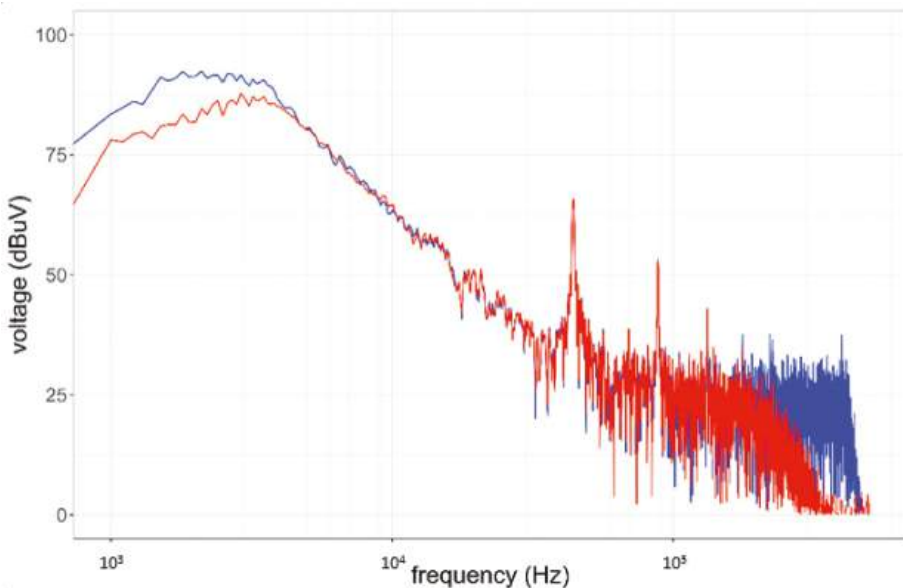


Figure 11. Comparison of the FFT spectra obtained from IMFs 2–5 extracted with EMD (red) and from the original signal (blue).

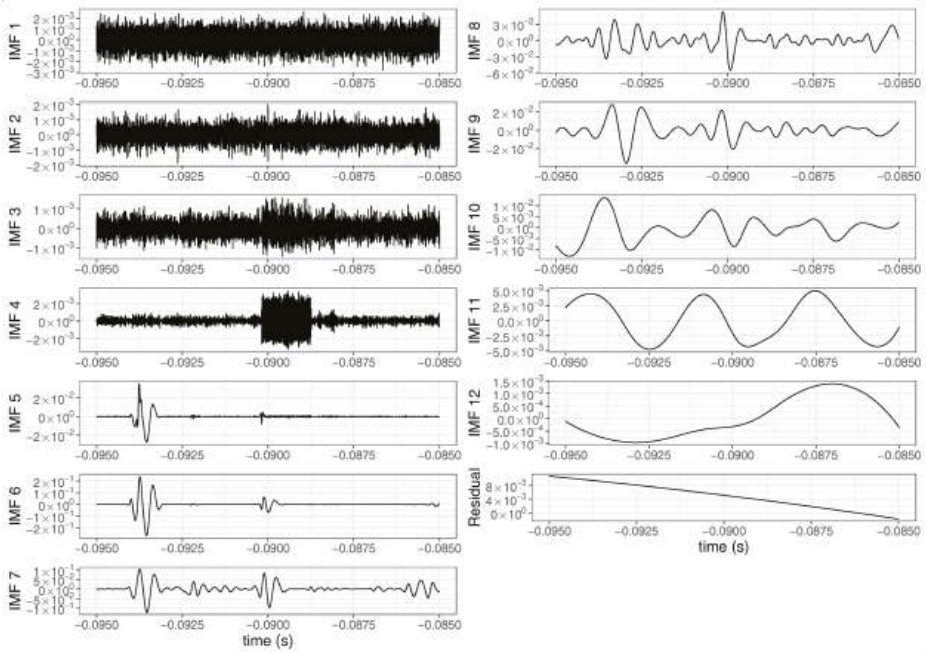


Figure 12. IMFs extracted with the EEMD procedure.

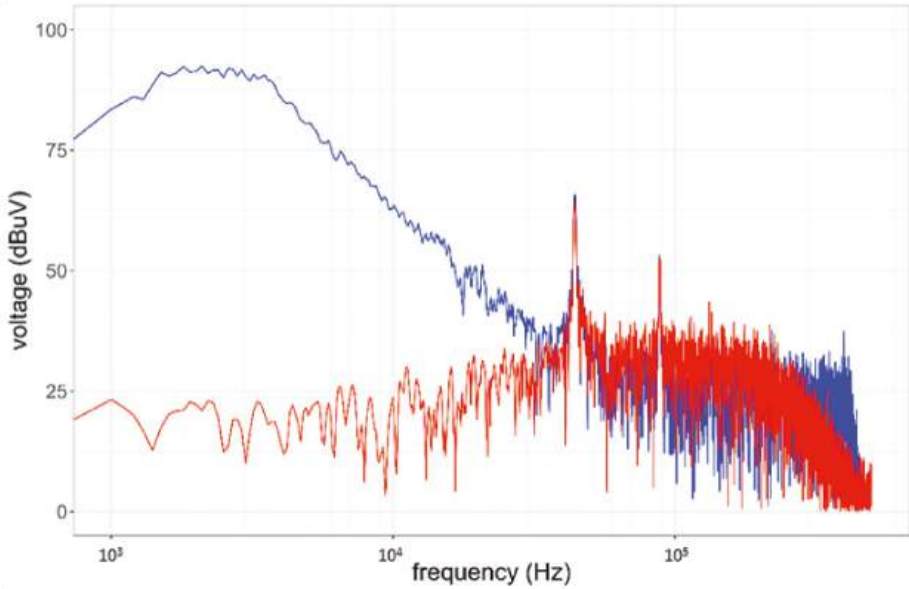


Figure 13. Comparison of the FFT spectra obtained from IMFs 2–4 extracted with EEMD (red) and from the original signal (blue).

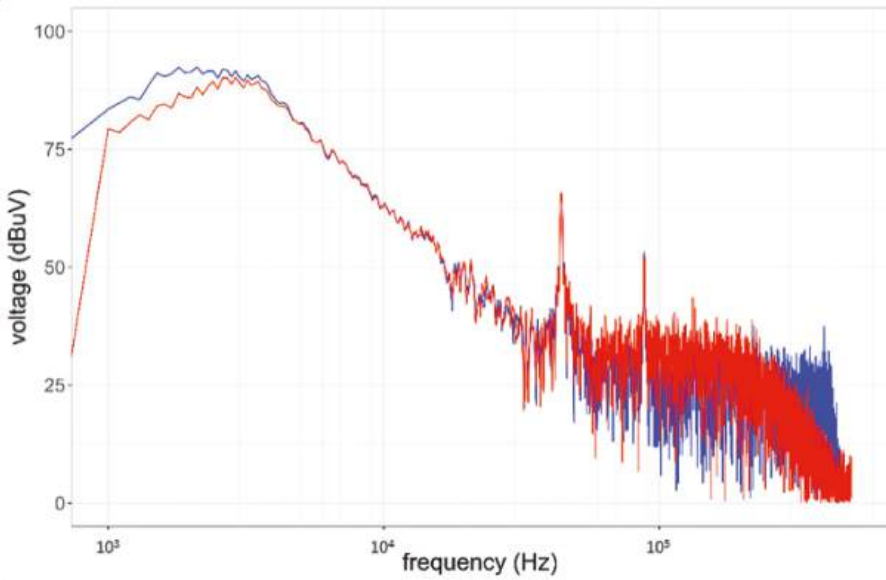


Figure 14. Comparison of the FFT spectra obtained from IMFs 2–7 extracted with EEMD (red) and from the original signal (blue).

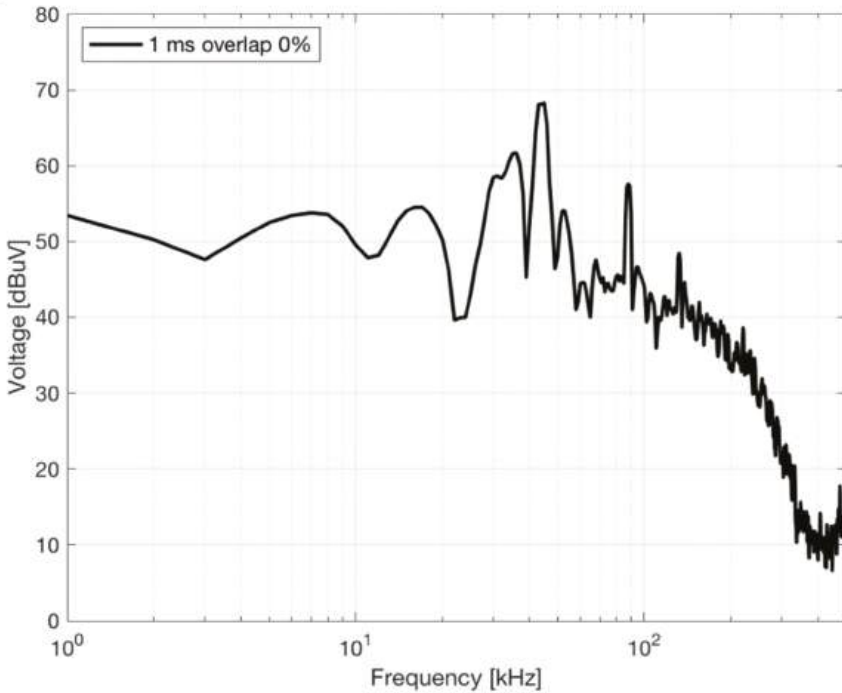


Figure 15. STFT spectrum with $\Delta f = 1$ kHz and time step $\Delta t = 1$ ms of the signal resulting from the composition of IMFs 2 and 3 extracted with EMD.

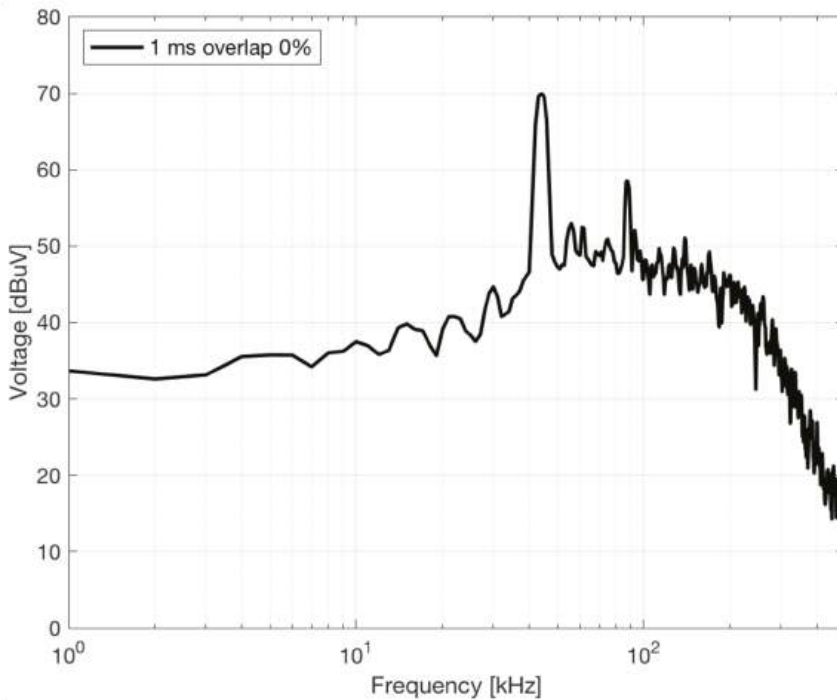


Figure 16. STFT spectrum with $\Delta f = 1$ kHz and time step $\Delta t = 1$ ms of the signal resulting from the composition of IMFs 2 to 4 extracted with EEMD.

4. Conclusions

The problem of the assessment of conducted emissions of Switched Mode Power Supplies (SMPSs) using time-domain sampled data is considered. Emissions measured with a Digital Sampling Oscilloscope using a Line Impedance Stabilization Network are characterized by fast switching pulses and damped oscillations, posing a problem for reconciling amplitude accuracy, suitable frequency resolution and fast time response to track signal dynamics.

Suitable processing techniques are discussed, contrasted to the most popular approach of using Discrete Fourier Transform analysis. The DFT drawbacks are pointed out in Section 2, in relation to the unfavorable time support and frequency resolution, as well as to the known issues of amplitude accuracy and spectral leakage. Two techniques (Wavelet Packet Transform (WPT) and Empirical Mode Decomposition (EMD)) based on different principles are then evaluated, with the objective of an adequate and accurate handling of signal characteristics, as reflected in its spectral components and their amplitude, for the assessment of SMPS conducted emissions.

WPT and EMD are compared for complexity, ease of implementation and, most of all, usability of the output and suitability to identify and represent the relevant spectral components. The objective is that of an accurate amplitude estimate and assessment of hypothetical compliance to limits of emissions. The output representation of the WPT is more effective, in that the data are represented as one might expect for not only comparison with limits, but also analysis of short-term disturbance (e.g., for victim circuits characterized by some transient susceptibility) and in general tracking and troubleshooting of byproducts along the evolution of the signal.

WPT shows a general consistency and robustness with respect to the change of the number of levels L and downsampling q (applied to the original 10 MSa/s sample rate). Similarly, the change of mother wavelet is verified, passing in one case from the *symlet* (linear phase and asymmetric)

to the *biorthogonal* (linear phase and symmetric), using for each the minimum order, and in a second case using db15 ad sym8, observing a larger spectrum leakage for the latter. The sensitivity analysis indicates a variability of less than 1 dB when comparing values averaged with the adjacent time and frequency bins; maximum observed difference for the peak values is 3.6 dB for the broad 2.2 kHz component that suffers the largest variability.

The application of EMD and EEMD algorithms yields a limited number of IMFs that are sufficient to represent the original signal fairly accurately (four and six, respectively). Moreover, the representation can be made even more compact by exploiting the filtering effect of the IMFs on the low-frequency components of the signal, thus reducing the number of IMFs necessary to represent the most significant part of the spectrum to two and three, respectively. EMD represents the spectrum for frequencies larger than 100 kHz better than EEMD, which seems to produce a higher noise floor.

Future work will be focused on the identification of quantitative indices of performance and a framework to evaluate systematically the performances of the various implementations, especially for the WPT, where the number of mother wavelets and filter implementations is almost uncountable.

Author Contributions: The contribution of L.S. and A.M. to conceptualization, methodology, software, experimental validation, and writing is the same. All authors have read and agreed to the published version of the manuscript.

Funding: This research received no external funding.

Conflicts of Interest: The authors declare no conflict of interest.

References

1. Thomas, D. Conducted emissions in distribution systems (1 kHz–1 MHz). *IEEE Electromagn. Compat. Mag.* **2013**, *2*, 101–104. [[CrossRef](#)]
2. Larsson, E.A.; Bollen, M.H.; Wahlberg, M.G.; Lundmark, C.M.; Ronnberg, S.K. Measurements of high-frequency (2–150 kHz) distortion in low-voltage networks. *IEEE Trans. Power Deliv.* **2010**, *25*, 1749–1757. [[CrossRef](#)]
3. Frey, D.; Schanen, J.; Quintana, S.; Bollen, M.; Conrath, C. Study of high frequency harmonics propagation in industrial networks. In Proceedings of the EMC Europe, Rome, Italy, 17–21 September 2012.
4. Bartak, G.F.; Abart, A. EMI in the frequency range 2 kHz–150 kHz. In Proceedings of the 22nd International Conference and Exhibition on Electricity Distribution (CIRED 2013), Stockholm, Sweden, 10–13 June 2013.
5. Klatt, M.; Meyer, J.; Schegner, P. Comparison of measurement methods for the frequency range of 2 kHz to 150 kHz. In Proceedings of the 2014 16th International Conference on Harmonics and Quality of Power (ICHQP), Bucharest, Romania, 25–28 May 2014.
6. Sandrolini, L.; Thomas, D.W.P.; Sumner, M.; Rose, C. Measurement and Evaluation of the Conducted Emissions of a DC/DC Power Converter in the Frequency Range 2–150 kHz. In Proceedings of the 2018 IEEE Symposium on Electromagnetic Compatibility, Signal Integrity and Power Integrity (EMC, SI & PI), Long Beach, CA, USA, 30 July–3 August 2018.
7. Sandrolini, L.; Mariscotti, A. Techniques for the Analysis of Time-Domain Conducted Emissions of SMPS in Smart Grids. In Proceedings of the 2019 IEEE International Conference on Environment and Electrical Engineering and 2019 IEEE Industrial and Commercial Power Systems Europe, Genova, Italy, 11–14 June 2019.
8. Ensini, L.; Sandrolini, L.; Thomas DW, P.; Sumner, M.; Rose, C. Conducted Emissions on DC Power Grids. In Proceedings of the International Symposium on Electromagnetic Compatibility (EMC EUROPE), Amsterdam, The Netherlands, 27–30 August 2018.
9. Sandrolini, L.; Pasini, G. Study of the Conducted Emissions of an SMPS Power Converter from 2 to 150 kHz. In Proceedings of the IEEE International Conference on Environment and Electrical Engineering and 2018 IEEE Industrial and Commercial Power Systems Europe, Palermo, Italy, 12–15 June 2018.
10. CENELEC EN 61000-4-19. *Electromagnetic Compatibility (EMC)—Part 4-19: Testing and Measurement Techniques—Test for Immunity to Conducted, Differential Mode Disturbances and Signalling in the Frequency Range 2 kHz to 150 kHz at a.c. Power Ports*; European Committee for Electrotechnical Standardization: Brussels, Belgium, 2014.

11. CENELEC EN 55014-1. *Electromagnetic Compatibility—Requirements for House—Hold Appliances, Electric Tools and Similar Apparatus—Part 1: Emission*; European Committee for Electrotechnical Standardization: Brussels, Belgium, 2017.
12. CENELEC EN 55015. *Limits and Methods of Measurement of Radio Disturbance Characteristics of Electrical Lighting and Similar Equipment*; European Committee for Electrotechnical Standardization: Brussels, Belgium, 2014.
13. CENELEC EN 61000-4-30. *Electromagnetic Compatibility—Part 4-30: Testing and Measurement Techniques—Power Quality Measurement Methods*; European Committee for Electrotechnical Standardization: Brussels, Belgium, 2015.
14. CENELEC EN 50065-1. *Signalling on Low-Voltage Electrical Installations in the Frequency Range 3 kHz to 148.5 kHz—Part 1: General Requirements, Frequency Bands and Electromagnetic Disturbances*; European Committee for Electrotechnical Standardization: Brussels, Belgium, 2012.
15. Sandrolini, L.; Mariscotti, A. Impact of Short-Time Fourier Transform Parameters on the Accuracy of EMI Spectra Estimates in the 2–150 kHz Supraharmonics Interval. *Electr. Power Syst. Res.* under review.
16. Barros, J.; Diego, R.I. Analysis of Harmonics in Power Systems Using the Wavelet-Packet Transform. *IEEE Trans. Instrum. Meas.* **2008**, *57*, 63–69. [CrossRef]
17. Masoum, M.A.S.; Jamali, S.; Ghaffarzadeh, N. Detection and classification of power quality disturbances using discrete wavelet transform and wavelet networks. *IET Sci. Meas. Technol.* **2010**, *4*, 193–205. [CrossRef]
18. Lodetti, S.; Bruna, J.; Melerio, J.J.; Sanz, J.F. Wavelet Packet Decomposition for IEC Compliant Assessment of Harmonics under Stationary and Fluctuating Conditions. *Energies* **2019**, *12*, 4389. [CrossRef]
19. Zhu, S.-X.; Liu, H. Simulation study of power harmonic based on Daubechies wavelet. In Proceedings of the 2010 International Conference on E-Product E-Service and E-Entertainment, Henan, China, 7–9 November 2010.
20. Mariscotti, A. Characterization of Power Quality transient phenomena of DC railway traction supply. *Acta Imeko* **2012**, *1*, 26–35. [CrossRef]
21. Mariscotti, A. Methods for Ripple Index evaluation in DC Low Voltage Distribution Networks. In Proceedings of the IEEE Instrumentation and Measurement Technical Conference (IMTC), Warsaw, Poland, 2–4 May 2007.
22. Hai, Y.; Chen, J.-Y. RMS and power measurements based on wavelet packet decomposition using special IIR filter bank. In Proceedings of the 2011 International Conference on Electronic & Mechanical Engineering and Information Technology, Harbin, China, 12–14 August 2011.
23. Huang, N.E.; Wu, Z. A review on Hilbert-Huang transform: Method and its applications to geophysical studies. *Rev. Geophys.* **2008**, *46*, 1–23. [CrossRef]
24. Li, H.; Zhang, Y.; Zheng, H. Hilbert-Huang transform and marginal spectrum for detection and diagnosis of localized defects in roller bearings. *J. Mech. Sci. Technol.* **2009**, *23*, 291–301. [CrossRef]
25. Fu, K.; Qu, J.; Chai, Y.; Zou, T. Hilbert marginal spectrum analysis for automatic seizure detection in EEG signals. *Biomed. Signal Proc. Control* **2015**, *18*, 179–185. [CrossRef]
26. Zhaohua, W.; Huang, N.E. Ensemble Empirical Mode Decomposition: A Noise-Assisted Data Analysis Method. *Adv. Adapt. Data Anal.* **2009**, *1*, 1–41.
27. Gong, X.; Ferreira, J.A. Comparison and Reduction of Conducted EMI in SiC JFET and Si IGBT-Based Motor Drives. *IEEE Trans. Power Electron.* **2014**, *29*, 1757–1767. [CrossRef]
28. Mariscotti, A. Normative Framework for the Assessment of the Radiated Electromagnetic Emissions from Traction Power Supply and Rolling Stock. In Proceedings of the 2019 IEEE Vehicle Power and Propulsion Conference (VPPC), Hanoi, Vietnam, 14–17 October 2019.
29. IEC 61000-4-7. *Electromagnetic Compatibility (EMC)—Part 4-7: Testing and Measurement Techniques—General Guide on Harmonics and Interharmonics Measurements and Instrumentation, for Power Supply Systems and Equipment Connected Thereto*; International Electrotechnical Commission: Geneva, Switzerland, 2009.
30. Helseke, J.; Luukko, P.J. Rlibeemd: Ensemble Empirical Mode Decomposition (EEMD) and Its Complete Variant (CEEMDAN); R Package Version 1.4.1. 2018. Available online: <https://github.com/helseke/Rlibeemd> (accessed on 1 October 2020).
31. Luukko, P.J.; Helseke, J.; Räsänen, E. Introducing libeemd: A program package for performing the ensemble empirical mode decomposition. *Comput. Stat.* **2006**, *31*, 545–557. [CrossRef]
32. Stallone, A.; Cicone, A.; Materassi, M. New insights and best practices for the successful use of Empirical Mode Decomposition, Iterative Filtering and derived algorithms. *Sci. Rep.* **2020**, *10*, 15161. [CrossRef] [PubMed]

33. Feldman, M. Analytical basics of the EMD: Two harmonics decomposition. *Mech. Syst. Signal Process.* **2009**, *23*, 2059–2071. [[CrossRef](#)]
34. Ge, H.; Chen, G.; Yu, H.; Chen, H.; An, F. Theoretical Analysis of Empirical Mode Decomposition. *Symmetry* **2018**, *10*, 623. [[CrossRef](#)]

Publisher’s Note: MDPI stays neutral with regard to jurisdictional claims in published maps and institutional affiliations.



© 2020 by the authors. Licensee MDPI, Basel, Switzerland. This article is an open access article distributed under the terms and conditions of the Creative Commons Attribution (CC BY) license (<http://creativecommons.org/licenses/by/4.0/>).

Article

Modeling and Optimization of Impedance Balancing Technique for Common Mode Noise Attenuation in DC-DC Boost Converters

Shuaitao Zhang ^{1,*}, Baihua Zhang ², Qiang Lin ¹, Eiji Takegami ³, Masahito Shoyama ¹ and Gamal M. Dousoky ^{1,4,5}

¹ Graduate School of Information Science and Electrical Engineering, Kyushu University, Fukuoka 819-0395, Japan; lin@ckt.ees.kyushu-u.ac.jp (Q.L.); shoyama@ees.kyushu-u.ac.jp (M.S.); dousoky@mu.edu.eg (G.M.D.)

² Institute of Engineering Thermophysics, China Academy of Science, Beijing 100190, China; 09291159@bjtu.edu.cn

³ Technology Development Department, TDK-Lambda Corporation, Niigata 940-1195, Japan; e.takegami@jp.tdk-lambda.com

⁴ Electrical Engineering Department, Minia University, Minia 61517, Egypt

⁵ Department of Communications and Computer Engineering, Nahda University, New Beni Suef 62513, Egypt

* Correspondence: szhang@ckt.ees.kyushu-u.ac.jp

Received: 13 February 2020; Accepted: 13 March 2020; Published: 14 March 2020

Abstract: As an effective means of suppressing electromagnetic interference (EMI) noise, the impedance balancing technique has been adopted in the literature. By suppressing the noise source, this technique can theoretically reduce the noise to zero. Nevertheless, its effect is limited in practice and also suffers from noise spikes. Therefore, this paper introduces an accurate frequency modeling method to investigate the attenuation degree of noise source and redesign the impedance selection accordingly in order to improve the noise reduction capability. Based on a conventional boost converter, the common mode (CM) noise model was built by identifying the noise source and propagation paths at first. Then the noise source model was extracted through capturing the switching voltage waveform in time domain and then calculating its Fourier series in frequency domain. After that, the conventional boost converter was modified with the known impedance balancing techniques. This balanced circuit was analyzed with the introduced modeling method, and the equivalent noise source was precisely estimated by combining the noise spectra and impedance information. Furthermore, two optimized schemes with redesigned impedances were proposed to deal with the resonance problem. A hardware circuit was designed and built to experimentally validate the proposed concepts. The experimental results demonstrate the feasibility and effectiveness of the proposed schemes.

Keywords: common mode noise; EMI modeling; Fourier series; impedance balancing; resonant frequency

1. Introduction

The switch-mode power supply (SMPS) has played an important role in power generation and conversion systems, which tend to require a higher reliability, a higher power density, and a longer working life. However, the controllable switches adopted in SMPS, like metal-oxide-semiconductor field-effect transistors (MOSFETs), insulated gate bipolar transistors (IGBTs) and especially, the newest wide bandgap (WBG) semiconductor switches, may generate violent voltage and current gradients (dv/dt and di/dt). Those gradients bring a serious EMI problem and threaten the normal operation of electrical equipment. Typically, relevant electromagnetic compatibility (EMC) standards which include conducted emission and radiated emission must be fulfilled before the products enter the market [1,2].

Plenty of efforts have been made to investigate the generation and propagation mechanisms of the conducted noise. Among these investigation approaches, establishing an EMI noise model helps to predict noise spectrum results and adopt appropriate attenuation strategies in the early stage [3–15]. The lumped circuit modeling method, which depends on the time-domain circuit simulation has been introduced in [3,4]. This general model contains the coefficients of each element and then give EMI prediction result by utilizing simulation software. This model exactly corresponds to the actual circuit, with traits of intuitive and easy to understand. The results comparison shows that the established noise model gives an accurate prediction of conducted noise up to several MHz. However, the extraction of detailed parasitic parameters is difficult in practice, not to mention that the simulation process is time-consuming and may encounter convergence problems.

To process faster and get stable predictions, the frequency domain approach has been developed [5–15]. The early-stage modeling methods used simplified lumped parameters and ideal geometric shapes to replace the circuit impedance and the noise source, respectively [5,6]. However, such approximation has to deal with over-simplification and the accuracy of noise prediction needs further improvement.

Recently, a new branch of frequency domain modeling, namely the “behavioral modeling method” has been proposed and received extensive attention [7–9]. Instead of establishing the common (CM) noise model and differential mode (DM) noise model respectively, the behavioral model could predict the CM and DM noise in one integrated model. Both the two-terminal (one port) model and three-terminal (two ports) model have been extracted based on Thevenin or Norton theorems. This method would work well when the object topology is not very complicated, like non-isolated converters and half-bridge circuits. Nevertheless, without the analysis of noise propagation, the impedance identification has always troubled by the lack of a physical meaning. This problem becomes especially significant when modeling complex circuits. The impedance error would continue to affect the precision of the prediction results. Even repeating measurements under different series and shunt conditions may not help to reduce the error.

In order to do further research on the noise generation mechanism and improve the accuracy of the frequency domain model, some works have been focused on the switch voltage waveform [10–15]. Generally speaking, the switch has been substituted by a voltage or current source to represent the electric potential fluctuation. By replacing the switch waveform with the trapezoid, the simulation process was simplified and the predicted conducted emissions could match the experimental results around 3MHz [10]. Nevertheless, the fact that the real voltage waveform is not exactly a standard trapezoid should not be neglected. The authors of [11–15] have studied the switching dynamic process of the semiconductor in depth. More details have been concluded in the noise source model and thus help to improve the accuracy of the predicted results.

As an effective method to reduce the conducted noise, the impedance balancing technique has been discussed and implemented in many articles [16–21]. In this technique, the switch is surrounded by the impedance bridges while the impedance ratios of each two bridge arms remain the same. Therefore, the noise source could be greatly attenuated and the explanation can stem from the Wheatstone bridge theory. This technique can be flexibly applied to different circuits by adjusting the propagation impedance. The conventional boost converter (CBC) is handled so that the power inductor is spilled into two parts and the parasitic capacitances are adjusted. Furthermore, in the case of inverters, the general method is to coordinate with the external CM choke circuit [18]. The noise level has been suppressed well in these situations, but there are still some problems. Firstly, a serious noise peak occurred because of the impedance resonance. Moreover, it lacks an accurate model that could effectively estimate attenuation effects.

In this work, a novel CM noise modeling method was introduced to analyze and optimize the impedance balancing technique. Specifically, the attenuation degree of noise source was investigated by comparing the impedance and spectra information, and the resonance problem was solved effectively by redesigning the bridge impedances. Since the application of balance would not affect the operation

of the switch, the CBC was modeled at first. The accurate noise source method plays a vital role in improving the accuracy of the overall model.

This paper is organized as follows. Section 2 introduces the CM noise model of CBC and gives details of noise source modeling. Section 3 analyzes the mechanism of balancing impedance technique and evaluates the results in the view of impedance and equivalent noise source. Section 4 proposes two schemes to solve the resonance problem and gives experimental results to certify their validity. Finally, Section 5 provides conclusions of this work.

2. Formulation of the Modeling Method with an Accurate Noise Source

Figure 1 shows the configuration of a conventional boost converter connecting with the Line Impedance Stabilization Network (LISN). The LISN is placed between the DC power supply and the boost converter circuit, which provides a standard impedance to the equipment under test (EUT) and evaluates the conducted noise level by integrating with a spectrum analyzer. P and N are the positive pole and negative pole of converter input and G is the frame ground of circuit and LISN. In CBC, C_i and C_o are the input side and output side capacitances, and L is the power inductor. C_g is the capacitor that connects the ground and the drain of the MOSFET switch, which simulates the parasitic capacitors between the switch and the heatsink as well as the capacitors between the heatsink and the frame ground.

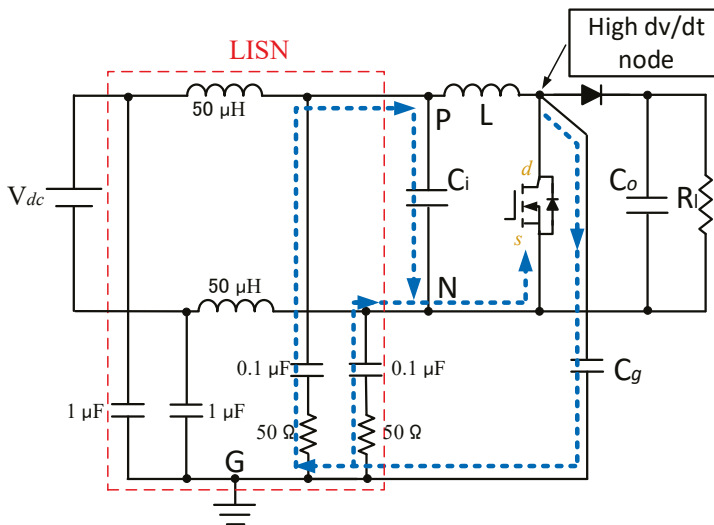


Figure 1. Configuration of the conventional boost circuit (CBC) and LISN setup.

2.1. Propagation Path of CM Noise Current and the Equivalent Model

At the conducted noise frequency band (from 150 kHz to 30 MHz), the relative impedance of the capacitor is small and the inductor is large. Therefore, C_i (100 μF) and L (500 μH) could be considered as short and open, respectively, in the CM noise model. The conducted noise was generated by the high-frequency voltage fluctuation between the drain and source of the switch. Here in the CBC, the source voltage is almost constant even when the switch is working. On the other hand, as marked as the high dv/dt node in Figure 1, the drain voltage changes rapidly and large CM current flows through C_g to the ground. In conclusion, the blue dotted line in Figure 1 indicates the flow direction of CM current.

The CM noise model resulted from the developed analysis is shown in Figure 2. Here, Z_{LISN} represents the equivalent resistance of LISN, which could be taken as a 25 Ω resistor in CM noise

calculation. V_N is the noise source, represents the voltage between drain and source of the switch (namely V_{ds}). Z_{Cg} is the impedance of C_g . According to the EMI measurement specification, the length of the connecting wire between EUT and LISN should be equal to 80 cm. Here, to improve the accuracy of the noise model, the impedance of the connecting wire is considered and represented as Z_W .

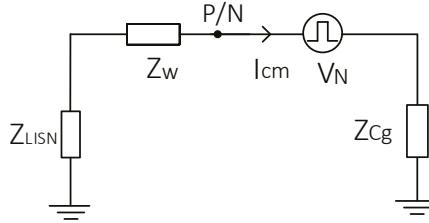


Figure 2. Common mode (CM) noise model of the conventional boost circuit.

According to the equivalent noise model, the CM noise voltage of CBC could be represented by Equation (1):

$$V_{LISN} = \frac{Z_{LISN}}{Z_{LISN} + Z_W + Z_{Cg}} V_N \tag{1}$$

This equation is true in both time and frequency domains, and the calculations in this paper are performed in a frequency domain.

2.2. Accurate Noise Source Modeling Method

As mentioned in the introduction, the precision of the noise model is largely affected by the noise source. Thus, plenty of methods have been proposed to obtain the noise source in time or in frequency domain. In this article, a novel frequency domain modeling method is introduced. The computational complexity is reduced while the accuracy is guaranteed. Specifically, the switch voltage waveform during experiment was observed and classified in time domain, and then, the overall spectrum could be obtained in frequency domain by calculating the Fourier series by parts. The accuracy of the noise source model is improved remarkably after considering the high frequency ringing.

The general steps for noise source modeling include:

- (1) Capture the turning on and turning off waveforms of the switch by the oscilloscope, while adjusting the appropriate time scale in order to observe the parameters.
- (2) Divide the overall waveform into three parts: trapezoid, turn-off ringing, and turn-on ringing. Extract the necessary parameters for the Fourier transform.
- (3) Calculate Fourier series of each component separately and then add them together. Finally, the overall spectrum could be obtained.

To specify the modeling process, an experimental setup was established according to Figure 1. Details of the experimental configuration are given in the following section. The key parameters of the circuit are given in Table 1. In addition, 1nF Y-capacitor was adopted as C_g .

Table 1. Key parameters of CBC.

Parameter	Value
Input voltage	12 V
Switch frequency	103 KHz
Duty ratio	0.75
Load	50 Ω

Figure 3 shows the voltage waveform of switch measured by oscilloscope. The ringing caused by turn-on and turn-off could be seen clearly from the following magnified images. Note that the turn-on ringing is quite limited and thus, its effectiveness could be ignored.

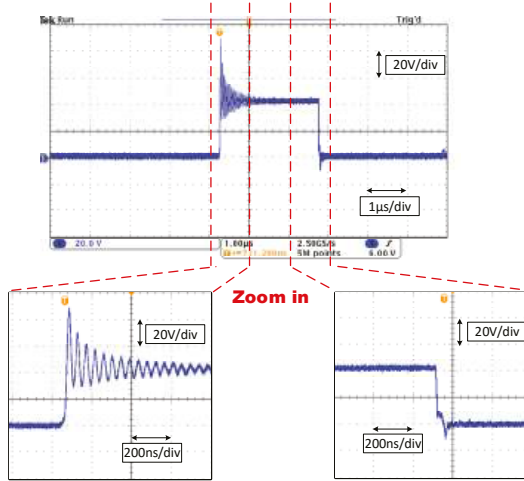


Figure 3. The experimental voltage waveform of switch measured by oscilloscope.

As the real voltage waveform is an irregular shape, it is difficult to calculate its spectrum directly. This paper decomposed the switch voltage waveform and the Fourier series could be done in steps. The corresponding decomposition process of the overall waveform is shown in Figure 4. The overall waveform is shown at the top of the figure, and it can be divided into the trapezoid component and the ringing component. This decomposition has reduced the complexity of Fourier transformation and improved the precision at the same time. The relative parameters are also marked in Figure 4, which could help to identify the corresponding symbols listed in Table 2.

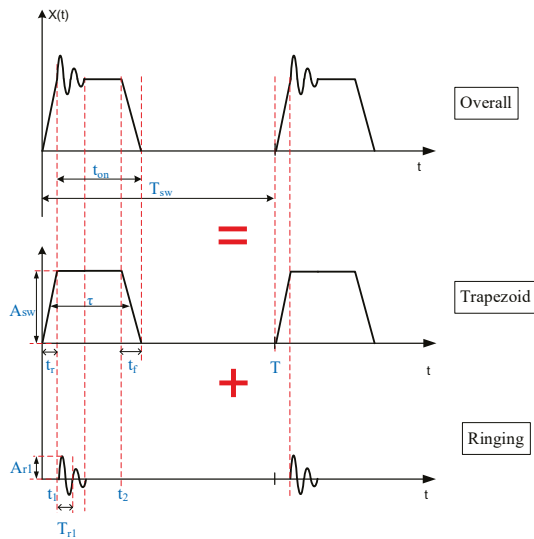


Figure 4. Decomposition diagram of the switch voltage waveform.

Table 2. Characteristic parameters of the switch voltage waveform.

Parameter	Symbol	Value
Amplitude of trapezoid	A_{sw}	42.3 V
Period of the voltage	T_{sw}	9.7 μ s
Switching time period	τ	2.47 μ s
Rising time	t_r	70 ns
Falling time	t_f	29 ns
Duration of the turn-off ringing	t_{on}	2.5 μ s
Amplitude of the turn-off ringing	A_{r1}	41.5 V
Period of the turn-off ringing	T_{r1}	42.3 ns

According to the mathematical definition [14], the formula for calculating the Fourier series corresponding to trapezoid could be expressed in Equation (2).

$$C_{n,t} = -j \frac{A_{sw}}{2\pi n} e^{-\frac{jn\pi(\tau+t_r)}{T_{sw}}} \left[\operatorname{sinc}\left(n \frac{t_r}{T_{sw}}\right) e^{-\frac{jn\pi\tau}{T_{sw}}} - \operatorname{sinc}\left(n \frac{t_f}{T_{sw}}\right) e^{-\frac{jn\pi\tau}{T_{sw}}} \right] \quad (2)$$

In order to approximate the experimental waveform, the difference of turn-on time and turn-off time was also taken into consideration.

Before calculating Fourier series of the ringing waveform, it is better to clarify the corresponding time-domain expressions. The ringing shown in Figure 4 begins after the switch turns off (t_1), and will last until the switch turns on (t_2). Therefore, it could be written as a piecewise function, as is presented in Equation (3):

$$V_r(t) = \begin{cases} 0, & 0 < t < t_1 \\ \frac{A_{r1} \sin \omega_{r1}(t-t_r)}{e^{k_{r1}(t-t_r)}}, & t_1 \leq t < t_2 \\ 0, & t_2 \leq t < T \end{cases} \quad (3)$$

According to the definition, the formula for calculating Fourier series can be written as in Equation (4). Then, the Fourier series of the ringing part can be calculated by substituting Equation (3) into Equation (4).

$$C_{n,r} = \frac{1}{T} \int_{(T)} V_r(t) \cdot e^{-jn\omega} \cdot dt \quad (4)$$

Finally, the Fourier coefficient of the overall switch waveform would be expressed as in Equation (5).

$$C_n = C_{n,t} + C_{n,r} \quad (5)$$

Figure 5 shows the experimental setup for capturing the voltage waveform and measuring the conducted EMI noise. The connection order is the same with configuration in Figure 1. In addition, the spectrum analyzer is connected with LISN to receive and analyze the signal, and the PC is used to display and record the spectra results. The EUT in this article is the conventional boost circuit and the different balanced boost circuits.



Figure 5. The experimental setup of conducted noise measurement.

According to Equations (2)–(5) and the measured data, the Fourier series calculation was completed with Matlab 2015b. Figure 6 shows the noise source spectra comparison between experimental and calculation results. The calculation results are plotted in the blue line, and the red experimental results refer to Fast Fourier Transformation (FFT) computed by the oscilloscope. The comparison shows that the calculation results match the experimental result in all frequency ranges. The high-frequency peak is caused by the ringing, and this frequency (around 23.5 MHz) agrees with the frequency of ringing waveform in Figure 3 ($T_{r1} = 42.3$ ns). The effectiveness of this frequency domain modeling method and the obtained parameters was well verified.

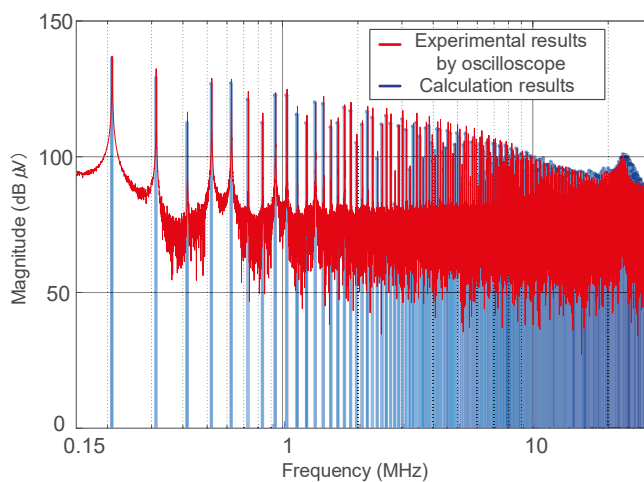


Figure 6. The frequency spectra of switch voltage (noise source) comparison between calculation and measured results.

Furthermore, based on Equation (1), Figure 7 shows the prediction result of CBC by utilizing the calculated noise source. The experimental result measured by LISN is also given in green. It can be

observed that the prediction result matches the measurement in the whole frequency band, and this model is able to predict CM noise with good accuracy.

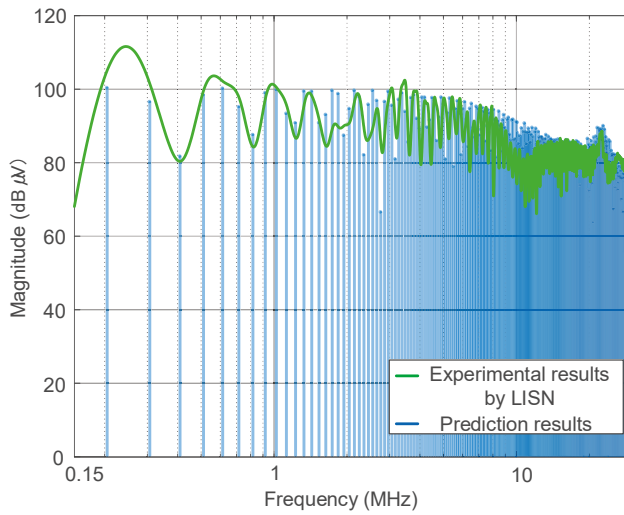


Figure 7. CM noise spectra comparison of a conventional boost converter (CBC) between prediction and measured results.

3. Analysis and Modeling of Impedance Balancing Technique

Instead of adding conventional passive or active EMI filters, the impedance balancing technique could reduce the conducted noise by changing the topology of CBC. The configuration of balanced boost converter along with LISN is shown in Figure 8. Compared with Figure 1, the power inductor L was split into two parts (L_1 and L_2) and another capacitor C_2 was placed between the N phase and the ground. This action changes the path of the noise current without affecting the efficiency of the circuit.

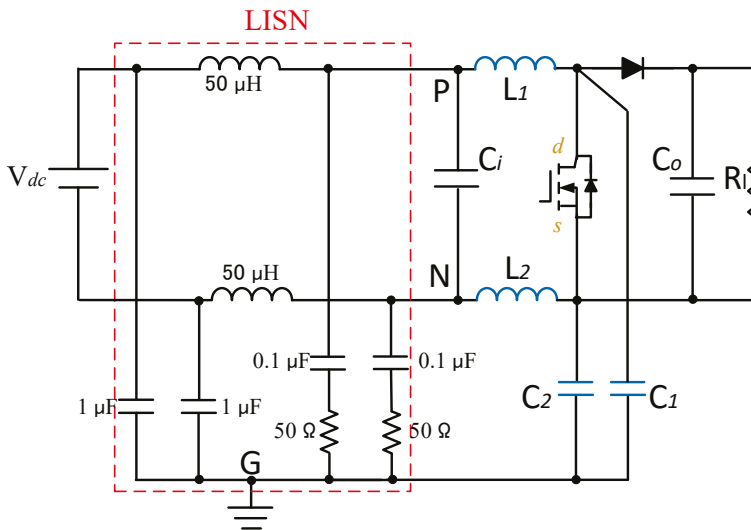


Figure 8. Configuration of the balanced boost converter and LISN.

In this article, as the power inductor in the CBC is 500 μH , two 250 μH inductors (L_1, L_2) and two 1nF Y-capacitors (C_1, C_2) were utilized to build the balanced circuit. The magnitude spectra of impedance bridge arms are shown in Figure 10. The figure shows that both inductors and capacitances are well matched over the frequency range. The condition of balancing impedance is properly satisfied.

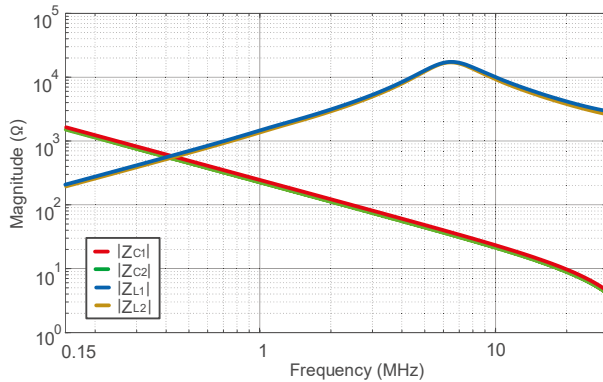


Figure 10. Magnitude comparison of bridge arms impedance (Z_{C1} VS. Z_{C2} and Z_{L1} VS. Z_{L2}).

Figure 11 shows the experimental CM noise spectrum of balanced boost circuit, which is plotted in red. Meanwhile, the green envelope is the CM noise of CBC (same as in Figure 7). By utilizing the balanced technique, the noise level was well attenuated from 0.5 MHz and upwards. The effect of this technique is obvious, as much as 40 dB reduction was done at some frequency points. Nevertheless, the noise peak at low frequency bands degraded the performance. The relative analysis and solution are given in the following sections.

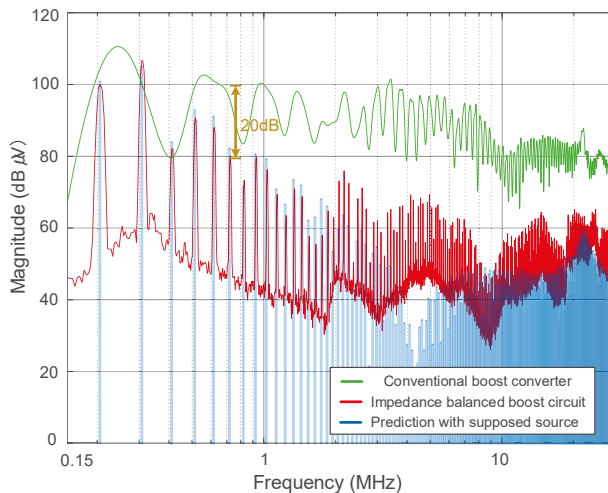


Figure 11. CM noise spectra comparison of balanced impedance circuit.

3.2. Noise Source Evaluation and Noise Spectrum Prediction

As is shown in Figure 11, the CM noise of balanced boost circuit did not dropped to zero, even if the impedance arms are almost balanced. This means that Equation (7) could not calculate the equivalent noise source accurately. This error may be caused by the interference of the PCB layout and

the inevitable mismatch of the impedance. Therefore, this article proposed a novel method to evaluate the attenuation level of the noise source and give prediction accordingly.

Comparing the voltage of LISN in the CBC and the balanced boost circuits, which are represented in Equations (1) and (8), respectively, it should be noted that the two formulas have the same form and the difference is the impedance Z_E and Z_{C_g} in the denominator. This also means that the first half of Equations (1) and (8) are the same when Z_E equals to Z_{C_g} , and then the differences of the two noise sources can be directly deducted from the CM noise spectra, as shown in Figure 11.

The equivalent impedance of balanced boost circuit Z_E could be calculated by Equations (6), or measured directly. The error between the two results is small. Referring to Equation (6), Z_{E0} represents the entire impedance of 250 μH inductors (L_1, L_2) paralleled with 1 nF capacitors (C_1, C_2). Figure 12 shows the impedance variation of Z_{C_g} and Z_{E0} through frequency. The Z_{C_g} is larger than Z_{E0} from 0.15 MHz to 0.69 MHz, and then the Z_{E0} becomes larger from 0.69 MHz.

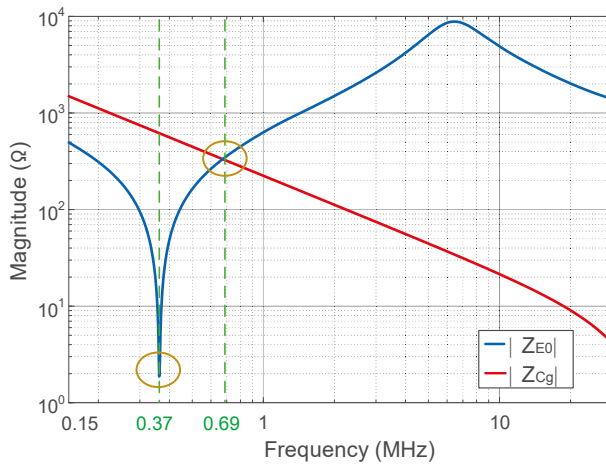


Figure 12. Magnitude spectra comparison between Z_{E0} (250 μH and 1 nF) and Z_{C_g} .

According to Figure 12, it should be noted that Z_{C_g} equals Z_{E0} at the point of 0.69 MHz, where the noise of balanced circuit is 80 $\text{dB}\mu\text{V}$ and the CBC is about 100 $\text{dB}\mu\text{V}$. This spectra difference equals to 20 $\text{dB}\mu\text{V}$, which means that V_N is about 10 times of V_E according to the definition. Therefore, this paper assumed that V_E is one-tenth of V_N and then substituted other measured impedance values into Equations (8) for calculation.

The prediction results are plotted in translucent blue in Figure 11 and are basically consistent with the measured spectrum except for the medium frequency band. This comparison confirms the hypothesis.

In addition, the resonance frequency of impedance arms could be calculated by Equations (10).

$$f_c = \frac{1}{2\pi \sqrt{(L_1 // L_2)(C_1 // C_2)}} \quad (10)$$

Specially, when L_1 and L_2 equal to 250 μH , C_1 and C_2 equal to 1nF, the series resonance of Z_{E0} happens at 0.37 MHz, which agrees with the noise peak in Figure 10. Therefore, it is necessary to find corresponding countermeasures to optimize the known impedance balancing technique.

4. Optimized Schemes with Redesigned Impedance Arms

As shown in Figure 11, the noise peak occurs at the resonant frequency; thus, several researchers have proposed different methods to solve the spike problem. In [17], the authors changed the inductance

value and added a pF-class capacitor to cooperate with the impedance ratio in Equation (9). However, this may push the noise spike to the middle or high frequency band. The designing method of the inductor in [21] achieved satisfactory results, but this result is based on an additional CM choke filter. As opposed to previous methods, this paper adjusted the values of passive elements to move the resonance peak out of the conductive frequency range.

As was mentioned in the previous section, a low-frequency peak occurs because of the series resonance among the four impedance bridge arms. On the other hand, it is hard to further suppress the equivalent noise source because the impedance arms are well matched, especially at a low frequency. Thus, the more practical method is to redesign the value of inductors or capacitors. Without changing the balancing configuration shown in Figure 8. This paper has proposed two alternative schemes to attenuate the noise peak according to Equations (10). One is increasing the inductor to 1.4 mH and the other is increasing the value of Y-capacitors to 4.7 nF. The following sections will investigate and compare the two approaches.

4.1. Balanced Boost Circuit with 1.4 mH Inductors and 1 nF Y-capacitors

After calculation using Equations (10), the inductance should be larger than 1.3 mH if the capacitors C_1 and C_2 are kept constant. Here, two 1.4mH inductors were utilized to replace the 250 μ H inductors. The experimental results were recorded and drawn with black in Figure 13, compared with the former balanced boost circuit in red and the green envelope of CBC. These experimental results show that the proposed balanced scheme with 1.4 mH inductors and 1nF capacitors could attenuate noise level over all frequency range compared with CBC. Furthermore, the spike at 0.37 MHz was effectively suppressed. However, the noise at high frequency increased in contrast with the former balanced boost circuit (250 μ H and 1 nF). The valley at 0.8 MHz is due to the self-resonance between the 1.4 mH inductor and its EPCs.

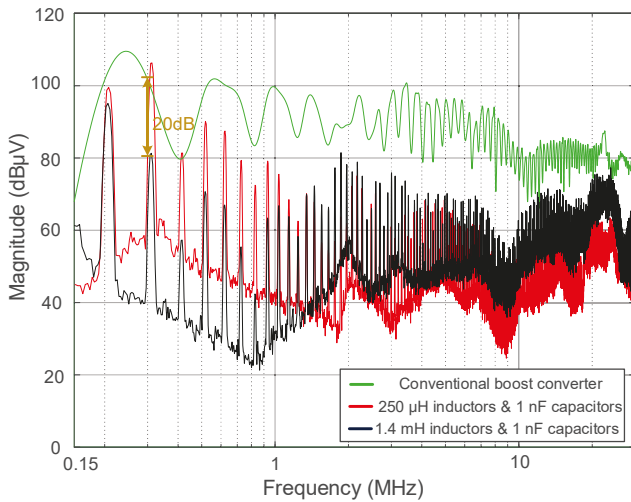


Figure 13. CM noise comparison after replacing the 250 μ H inductors with 1.4 mH inductors.

Referring to Equations (6), Z_{E1} identifies the whole impedance including 1.4 mH inductors and 1nF Y-capacitors. Figure 14 gives its magnitude in black and makes comparison with Z_{Cg} in red. Note that Z_{E1} equals to Z_{Cg} at 0.24 MHz, which means that the noise source attenuation degree could be speculated quickly With the same analysis method as the one in Section 3. According to Figure 13, the noise spectra difference around 0.24 MHz reached about 20 dBμV, which indicates that

the equivalent noise source V_E in the optimized scheme was attenuated well compared with CBC. However, a drawback of this approach is the increased weight and volume of the circuit.

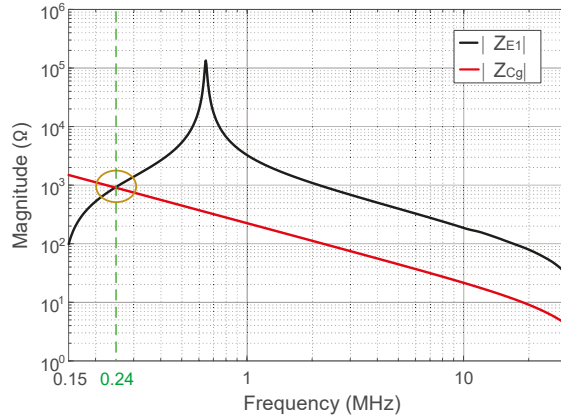


Figure 14. Impedance comparison between Z_{E1} (1.4 mH and 1 nF) and Z_{Cg} .

4.2. *Balanced Boost Circuit with 250 μ H Inductors and 4.7 nF Y-capacitors*

Other than using a pair of larger inductors, this scheme utilized greater Y-capacitors to decrease the series resonant frequency. After calculation, 4.7 nF capacitors were selected to replace the former 1nF capacitors and the other experimental conditions were kept the same.

The CM noise spectra comparison is shown in Figure 15. The purple curve is for the case of an optimized solution after replacing the 1 nF Y-capacitors with 4.7 nF, the green one is the noise envelope of CBC, and the red one is for the former balanced circuit boost (250 μ H and 1 nF). The comparison shows that after utilizing the scheme with 4.7 nF capacitors, a low-frequency spike was also moved out from the frequency band of interest and the CM noise was significantly attenuated. Meanwhile, at a high frequency, the noise after adopting 4.7 nF capacitors is lower than the former case using 1 nF capacitors.

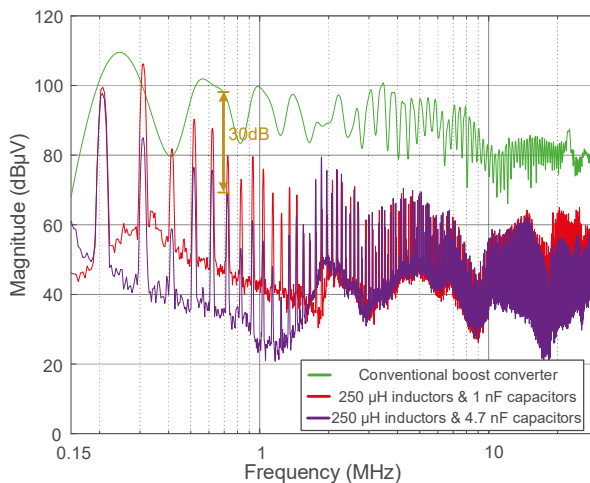


Figure 15. CM noise comparison after replacing the 1 nF Y-capacitors with 4.7 nF Y-capacitors.

Similarly to Z_{E1} , Z_{E2} represents the whole bridge impedance of 250 μH inductors and 4.7 nF Y-capacitors. The comparison between Z_{E2} (purple) and Z_{Cg} (red) is shown in Figure 16. The resonant frequency of optimized impedance Z_{E2} was removed to around 0.16 MHz and the performance at high frequency is almost the same compared to that in Figure 12. At 0.68 MHz, where Z_{E2} equals Z_{Cg} , about 30 dB reduction was achieved according to Figure 15. Compared with the former balanced boost circuit (250 μH and 1 nF), the noise source was significantly attenuated and the performance was improved over the entire frequency range.

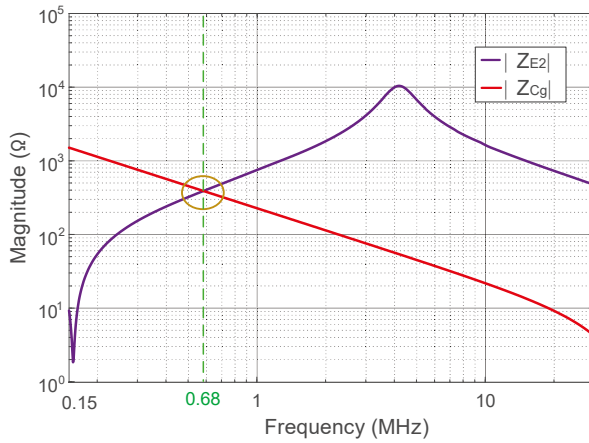


Figure 16. Impedance comparison between Z_{E2} (250 μH and 4.7 nF) and Z_{Cg} .

There may be some concerns that the greater capacitor may increase the CM current and exceed relative standards. Figure 17 shows the CM currents comparison between CBC and the optimized balanced boost circuit (250 μH and 4.7 nF). The results show that with optimized schemes, the CM current becomes even smaller because the noise source has been effectively attenuated.

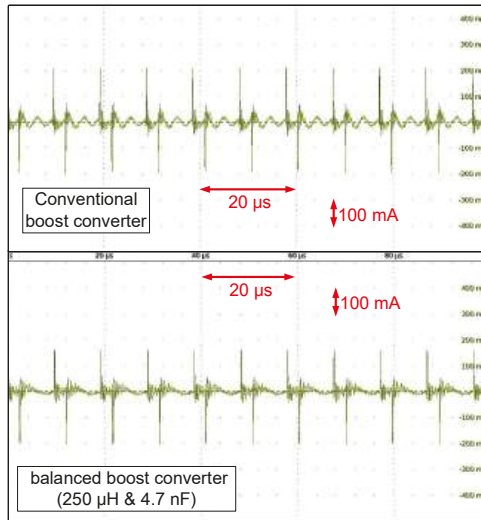


Figure 17. Experimental CM current waveforms comparison between CBC and optimized impedance balancing boost converter (250 μH and 4.7 nF).

In summary, the optimized scheme of changing the capacitors is more effective than replacing the inductors, which not only considers the attenuation results but also the cost and the difficulty of implementation.

A comparative investigation between the proposed work and the previously published relevant arts was carried out and is addressed in Table 3. The comparison reveals the effectiveness and practicability of the proposed schemes.

Table 3. Comparison of noise optimization effects.

	Noise Reduction Effect	Attenuated the Resonance Peak?	Required Additional Filter?	Practicability and Feasibility
[16]	Medium	No	Yes	Medium
[17]	Medium	No	No	Medium
[18]	Limited	No	Yes	Limited
[19,20]	Medium	Yes	Yes	Medium
Proposed work	Medium	Yes	No	High

5. Conclusions

Focusing on the noise attenuation with impedance balancing technique, a frequency domain modeling method and two optimized schemes are introduced in this paper. The accurate noise source model was extracted by capturing the switch voltage waveform and then calculating its Fourier series. Furthermore, for both noise source and CM noise of the conventional boost circuit, the accuracy of the noise model were verified by comparing the prediction results with the experimental measurements.

Then, the impedance balancing technique was adopted to attenuate the noise. Although this technique is effective to some extent, it suffers from noise spikes and also lacks a model that can predict the noise quantitatively. In this research, the noise source attenuation degree was evaluated by combining the noise spectra and impedance information. Furthermore, a quantitative prediction based on the proposed noise model is provided. A comparison between prediction and experimental results was conducted and the accuracy of the proposed noise model was practically verified.

Based on the basic impedance balancing configuration and the calculation formula of resonance frequency, two optimized schemes were proposed to deal with the noise peak in the low-frequency band. The size of the impedance arms was redesigned and the two schemes were investigated in different aspects. Finally, the experimental results were presented to demonstrate the analysis. The contribution of this research is enhancing the feasibility and effectiveness of the known impedance balancing technique.

Author Contributions: Conceptualization, methodology, investigation, S.Z., B.Z., M.S., and G.M.D.; validation, S.Z. and Q.L.; writing—review and editing S.Z. and G.M.D.; supervision M.S. and G.M.D.; project administration, E.T. All authors have read and agreed to the published version of the manuscript.

Funding: This research received no external funding.

Conflicts of Interest: The authors declare no conflict of interest.

References

1. Mainali, K.; Oruganti, R. Conducted EMI Mitigation Techniques for Switch-Mode Power Converters: A Survey. *IEEE Trans. Power Electron.* **2010**, *25*, 2344–2356. [[CrossRef](#)]
2. Tarateeraseth, V.; Hu, B.; See, K.Y.; Canavero, F.G. Accurate Extraction of Noise Source Impedance of an SMPS Under Operating Conditions. *IEEE Trans. Power Electron.* **2010**, *25*, 111–117. [[CrossRef](#)]

3. Yang, L.; Lu, B.; Dong, W.; Lu, Z.; Xu, M.; Lee, F.C.; Odendaal, W.G. Modeling and characterization of a 1 KW CCM PFC converter for conducted EMI prediction. In Proceedings of the Nineteenth Annual IEEE Applied Power Electronics Conference and Exposition, APEC'04, Anaheim, CA, USA, 22–26 February 2004; Volume 2, pp. 763–769.
4. Lai, J.; Huang, X.; Pepa, E.; Chen, S.; Nehl, T.W. Inverter EMI modeling and simulation methodologies. *IEEE Trans. Ind. Electron.* **2006**, *53*, 736–744.
5. Gubia, E.; Sanchis, P.; Ursua, A.; Lopez, J.; Marroyo, L. Frequency domain model of conducted EMI in electrical drives. *IEEE Power Electron. Lett.* **2005**, *3*, 45–49. [\[CrossRef\]](#)
6. Pei, X.; Zhang, K.; Kang, Y.; Chen, J. Prediction of common mode conducted EMI in single phase PWM inverter. In Proceedings of the 2004 IEEE 35th Annual Power Electronics Specialists Conference (IEEE Cat. No.04CH37551), Aachen, Germany, 20–25 June 2004; Volume 4, pp. 3060–3065.
7. Liu, Q.; Wang, F.; Boroyevich, D. Modular-Terminal-Behavioral (MTB) Model for Characterizing Switching Module Conducted EMI Generation in Converter Systems. *IEEE Trans. Power Electron.* **2006**, *21*, 1804–1814.
8. Bishnoi, H.; Mattavelli, P.; Burgos, R.; Boroyevich, D. EMI Behavioral Models of DC-Fed Three-Phase Motor Drive Systems. *IEEE Trans. Power Electron.* **2014**, *29*, 4633–4645. [\[CrossRef\]](#)
9. Kerrouche, B.; Bensetti, M.; Zaoui, A. New EMI Model with the Same Input Impedances as Converter. *IEEE Trans. Electromagn. Compat.* **2019**, *61*, 1072–1081. [\[CrossRef\]](#)
10. Mainali, K.; Oruganti, R. Simple Analytical Models to Predict Conducted EMI Noise in a Power Electronic Converter. In Proceedings of the IECON 2007—33rd Annual Conference of the IEEE Industrial Electronics Society, Taipei, Taiwan, 5–8 November 2007; pp. 1930–1936.
11. Jin, M.; Weiming, M. Power Converter EMI Analysis Including IGBT Nonlinear Switching Transient Model. *IEEE Trans. Ind. Electron.* **2006**, *53*, 1577–1583. [\[CrossRef\]](#)
12. Xia, Y.; Gu, Y.; Shen, J. Conducted EMC Modeling for EV Drives Considering Switching Dynamics and Frequency Dispersion. In Proceedings of the 2018 IEEE Energy Conversion Congress and Exposition (ECCE), Portland, OR, USA, 23–27 September 2018; pp. 4195–4202.
13. Xiang, Y.; Pei, X.; Zhou, W.; Kang, Y.; Wang, H. A Fast and Precise Method for Modeling EMI Source in Two-Level Three-Phase Converter. *IEEE Trans. Power Electron.* **2019**, *34*, 10650–10664. [\[CrossRef\]](#)
14. Zhang, B.; Zhang, S.; Li, H.; Shoyama, M.; Takegami, E. An Improved Simple EMI Modeling Method for Conducted Common Mode Noise Prediction in DC-DC Buck Converter. In Proceedings of the IEEE ICDCM'19, Matsue, Japan, 20–23 May 2019; pp. 1–6.
15. Kim, T.; Feng, D.; Jang, M.; Agelidis, V.G. Common Mode Noise Analysis for Cascaded Boost Converter with Silicon Carbide Devices. *IEEE Trans. Power Electron.* **2017**, *32*, 1917–1926. [\[CrossRef\]](#)
16. Shoyama, M.; Li, G.; Ninomiya, T. Balanced switching converter to reduce common-mode conducted noise. *IEEE Trans. Ind. Electron.* **2003**, *50*, 1095–1099. [\[CrossRef\]](#)
17. Wang, S.; Kong, P.; Lee, F.C. Common Mode Noise Reduction for Boost Converters Using General Balance Technique. *IEEE Trans. Power Electron.* **2007**, *22*, 1410–1416. [\[CrossRef\]](#)
18. Xing, L.; Sun, J. Conducted Common-Mode EMI Reduction by Impedance Balancing. *IEEE Trans. Power Electron.* **2012**, *27*, 1084–1089. [\[CrossRef\]](#)
19. Kong, P.; Wang, S.; Lee, F.C. Improving balance technique for high frequency common mode noise reduction in boost PFC converters. In Proceedings of the 2008 IEEE Power Electronics Specialists Conference, Rhodes, Greece, 15–19 June 2008; pp. 2941–2947.
20. Kong, P.; Wang, S.; Lee, F.C. Common Mode EMI Noise Suppression for Bridgeless PFC Converters. *IEEE Trans. Power Electron.* **2008**, *23*, 291–297. [\[CrossRef\]](#)
21. Zhang, Y.; Zheng, F.; Wang, Y. Alleviation of Electromagnetic Interference Noise Using a Resonant Shunt for Balanced Converters. *IEEE Trans. Power Electron.* **2015**, *30*, 4762–4773. [\[CrossRef\]](#)



© 2020 by the authors. Licensee MDPI, Basel, Switzerland. This article is an open access article distributed under the terms and conditions of the Creative Commons Attribution (CC BY) license (<http://creativecommons.org/licenses/by/4.0/>).

Article

Electromagnetic Susceptibility of Battery Management Systems' ICs for Electric Vehicles: Experimental Study

Orazio Aiello

Department of Electronics and Telecommunications, Politecnico di Torino, Corso Duca degli Abruzzi 24, I-10129 Torino, Italy; orazio.aiello@polito.it

Received: 20 January 2020; Accepted: 13 March 2020; Published: 19 March 2020

Abstract: The paper deals with the susceptibility to electromagnetic interference (EMI) of battery management systems (BMSs) for Li-ion and lithium-polymer (LiPo) battery packs employed in emerging electric and hybrid electric vehicles. A specific test board was developed to experimentally assess the EMI susceptibility of a BMS front-end integrated circuit by direct power injection (DPI) and radiated susceptibility measurements in an anechoic chamber. Experimental results are discussed in reference to the different setup, highlighting the related EMI-induced failure mechanisms observed during the tests.

Keywords: battery management system (BMS); Li-ion battery pack; electric vehicles (EVs); hybrid electric vehicles (HEVs); IC-level EMC; susceptibility to electromagnetic interference (EMI); direct power injection (DPI); anechoic chamber

1. Introduction

A greater and greater increase in the amount of electronic devices is expected in new vehicles to make cars capable of running self-diagnostics and interacting with the surrounding environment. On-board electronics systems for implementing safety features to reduce the number of accidents and fatalities on the roads have to properly operate in any operating conditions [1]. Smart power integrated circuits (ICs) employed in automotive front-end electronics have stringent requirements in terms of accuracy, even in an electromagnetically polluted environment, where relevant conducted and radiated interference are generated by the electric powertrain, by on-vehicle electronics and by mobile phones and/or other information and communication equipment carried by the driver and by the passengers in the cockpit [1]. Therefore, the susceptibility to electromagnetic interference (EMI) of smart power electronics and its on-board monitoring and control functions (i.e., thermal shutdown, current sensors and overvoltage protection) has to be considered. This to prevent malfunctions and guarantee the correct/expected functioning of the electronic system in any operating conditions [1–6].

Critical safety EMI-induced failures could be also a major threat to the safety in emerging electric and hybrid electric (EV/HEV) vehicles powered by batteries [7]. A battery management system (BMS) IC manages the state of charge of the battery pack, protecting it from operating outside its safe operating conditions [8–13]. Electromagnetic interference can be easily picked up by the long wires that connect BMS front-end ICs to each other, to the BMS control unit, to the terminals of the electrochemical cells and to the temperature sensors, which are spatially distributed over the whole battery pack module [14], and can easily impair the operation of data acquisition circuits [15–18].

Battery packs based on the most advanced lithium-ion (Li-ion) and lithium-polymer (LiPo) electrochemical technologies are nowadays the only viable options to address the challenging demands in terms of the electric energy storage and deliverable power per unit mass of electric vehicles (EVs) and hybrid electric vehicles (HEVs) [19–22]. Unfortunately, unlike lead-acid batteries and

other more conventional electrochemical accumulators, Li-ion and LiPo cells can be permanently damaged and can also originate life-threatening hazards such as fires and explosions in the event of overdischarging, overcharging and/or overtemperature operation [21–23]. An electronic battery management system (BMS), which quickly detects the onset of dangerous conditions and takes the appropriate countermeasures to avoid hazards, is therefore necessary to safely operate Li-ion and LiPo cells in vehicles [21–23]. A BMS, which is schematically depicted in Figure 1, typically includes several front-end modules that acquire critical cell information, such as terminal voltages and temperatures, and a digital control unit that runs specific control and management algorithms.

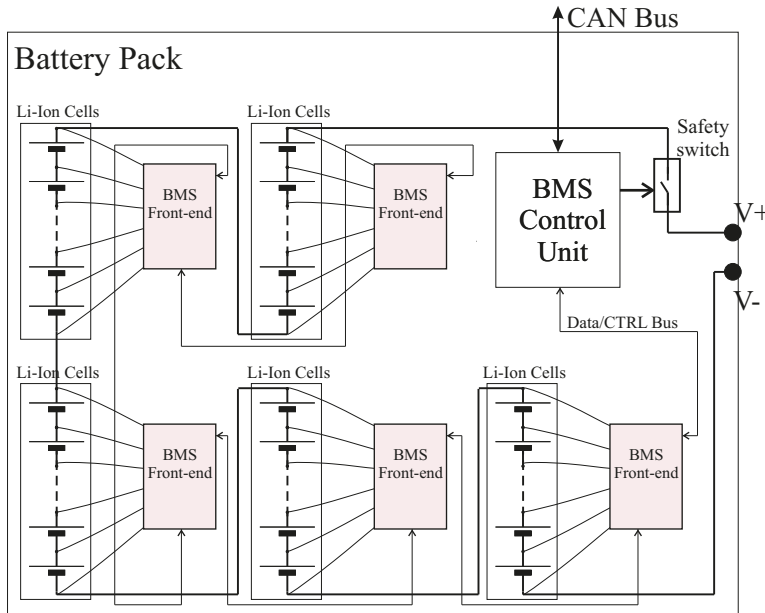


Figure 1. Architecture of a battery management system (BMS) for EV/HEV applications.

The typical BMS application scenario in Figure 1 and the EMI susceptibility issues of BMS systems for electric vehicles are addressed in this paper on the basis of the results of direct power injection (DPI) tests (IEC-62132-4 standard [24,25]) and radiated susceptibility tests (ISO11452-2 standard [26]) on a commercial smart power IC, widely employed as a BMS front-end in EV/HEV applications. In particular, the specific susceptibility level of the main IC pins and their different EMI-induced failure mechanisms were observed. The effectiveness of filtering techniques that can be adopted to enhance the immunity to EMI of a BMS, is also discussed.

The paper is organized as follows: in Section 2, the BMS IC is presented, and the printed circuit board (PCB) developed to perform EMC tests is introduced; in Section 3 the test bench and the test procedure adopted for DPI measurements are described. DPI test results are presented in Section 4 and discussed in Section 5. The results of radiated susceptibility measurements are presented in Section 6 and compared to the DPI tests in Section 7, and finally, in Section 8, some concluding remarks are drawn.

2. The BMS Front-End for the Tests

In order to investigate the susceptibility to EMI of a BMS for electric vehicles and perform the related conducted (DPI) and radiated (in anechoic chamber) tests, a PCB was specifically designed, and it is described in this Section.

2.1. BMS Front-End IC Structure and Operation

The simplified block diagram of the BMS front-end IC, which is considered in what follows as the device under test (DUT), is reported in the pink box of Figure 2. Such an IC is designed to monitor the terminal voltages of up to twelve series-connected electrochemical cells using a 12-bit analog-to-digital converter (ADC). To that end, the IC includes 12 cell input pins, internally connected to the ADC's differential input by a 12-channel, isolated, high-voltage analog multiplexer to measure the (differential) voltages across each of twelve series-connected cells, whose common-mode voltage can be up to 50 V with respect to the IC reference.

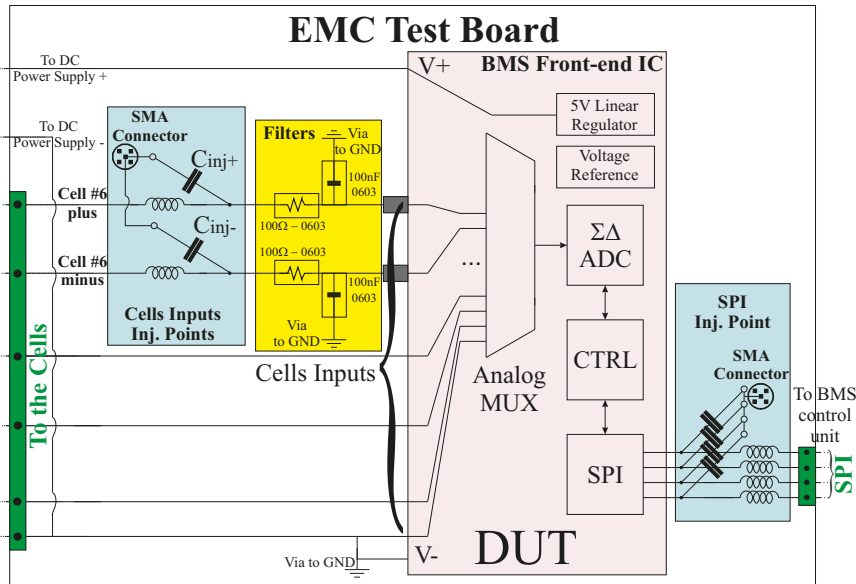


Figure 2. Simplified schematic diagram of the BMS integrated circuit (IC) direct power injection (DPI) test board.

The same IC can be also exploited for cell temperature measurements by using external negative temperature coefficient (NTC) sensors and including power drivers suitable for performing passive Li-ion cell voltage equalization. These functions have not been considered the susceptibility assessment and will not be mentioned hereafter.

The IC is designed to be operated by an external BMS control unit via a serial peripheral interface (SPI), through which acquired data can also be retrieved. The same SPI interface can be employed to connect the BMS IC to N similar devices in a daisy chain structure, as shown in Figure 1, so as to monitor up to $12N$ cells, addressing the requirements of high voltage battery packs including 100 or more series-connected cells. The frame of the specific SPI protocol implemented in the DUT includes a packet error code (PEC), by which SPI bus errors can be detected on the basis of the received data.

The IC operates from a DC supply voltage ranging from 10 V up to 55 V, which can be obtained either from the electrochemical cells to be monitored or from an external isolated DC/DC converter, and includes an internal voltage reference for the ADC and a 5 V linear voltage regulator to supply the low voltage analog and digital circuitry.

2.2. DPI Test Board

Firstly, the susceptibility to EMI of the DUT has been tested by the DPI method [24,25]. The dual layer PCB reported in Figure 2 has been designed to inject RF power into the IC pins which are

connected to the external wires. These possibly long wires are likely to collect a relevant amount of EMI in a realistic EV/HEV application. Two DPI injection points are established to superimpose an RF power into a couple of cell input pins and into the SPI pins of the IC, as depicted in Figure 2.

The cell input injection point includes an SMA connector and two RF coupling networks (each made up of a 6.8 nF capacitor and a 6 μ H inductor), designed so as to inject RF power onto the cell input pins connected to the positive and to the negative terminals of cell #6 in the stack, as depicted in Figure 2. A differential RF injection on a single cell input pin (cell #6 plus in Figure 2) can be performed by connecting only the injection capacitor C_{inj}^+ to the signal terminal of the SMA connector. A common-mode injection can be performed by connecting both the injection capacitors C_{inj}^+ and C_{inj}^- to the SMA signal line.

Figure 2 shows how the cell input injection points include an SMA connector and two RF coupling networks (each made up of a 1 nF CHECK capacitor and a 6 μ H inductor). Two RC filters with $R = 100 \Omega$, $C = 100$ nF implemented using 0603 SMD components (sketched in the yellow area) are mounted on the PCB immediately before the IC pins. The SPI injection point includes an SMA connector and four RF coupling networks (each made up of a 1 nF capacitor and a 6 μ H inductor), designed to perform DPI on all the SPI inputs at the same time, or alternatively, on a single SPI line.

3. Direct Power Injection Tests

The failure criteria considered in the DPI tests are stated along with the reasoning in this section.

3.1. DPI Test Bench

The PCB in Figure 2 has been employed to perform the DPI method according the setup in Figure 3. The DUT is operated from an external 20V power supply and the cell inputs of the DUT are connected to six series-connected commercial nickel metal hydride (NiMH) cells mounted on a separate board and tied to the DUT cell inputs by twisted wires. The current flowing through the cells during the DPI test is monitored by an amper meter, as shown in Figure 3.

The SPI lines of the DUT are connected to an automotive microcontroller evaluation board, which acts as the BMS control unit shown in Figure 1. Such a BMS control unit includes a controller area network (CAN) bus interface that is connected to a personal computer (PC) via a Vector CANCaseXL dongle. The microcontroller on the BMS control unit is programmed so as to forward the data content of the CAN packets with a specific identifier (ID) to the DUT SPI, and to send back to the CAN bus, with a different ID, the data retrieved from the DUT SPI during the same transaction. In this way, the DUT can be fully operated and monitored from the PC via the CAN bus. The CAN bus and the measurement instruments are managed by Matlab. The BMS IC is configured to be initialized, start the ADC conversion and read the register.

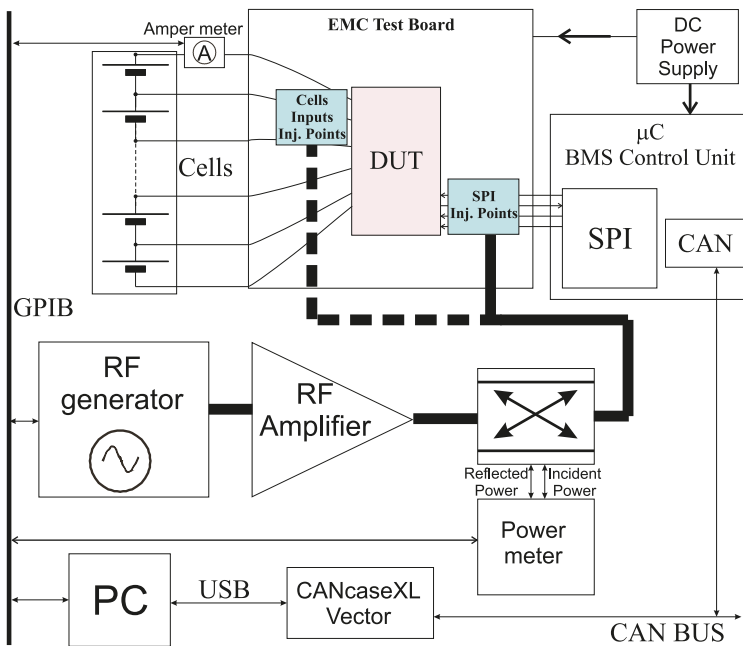


Figure 3. Direct power injection. Experimental test setup.

The continuous wave (CW) RF power injection is performed by means of an RF source connected to a 10 W RF power amplifier with a 1 MHz to 2 GHz bandwidth. The output of the power amplifier is fed to the injection points of the test board through a -20 dB directional coupler, whose forward and reverse coupled ports are connected to an RF power meter so as to monitor the incident and the reflected power. The RF source, the amper meter and the RF power meter are connected to the same PC employed to control the DUT via a general purpose interface bus (GPIB) dongle. Both the CAN bus and the GPIB are fully controlled by the PC in the Matlab environment.

3.2. DPI Test Procedure

During DPI tests, the DUT is operated from the PC in Figure 3 so as to periodically acquire the voltages of all the cells in the battery pack. The acquired data are then retrieved from the DUT SPI by the BMS control unit and forwarded to the PC via the CAN bus, together with the corresponding SPI PEC code. The same operations are first performed without injecting RF power (i.e., with the RF source in Figure 3 off) and then while injecting RF power at a given test frequency. The data retrieved from the DUT, with and without EMI injection, are finally compared and an EMI-induced failure is recorded if one of the following conditions occurs:

1. An SPI transmission error is detected (i.e., the received PEC is not consistent with the received data);
2. An EMI-induced offset in the cell voltages acquired with RF injection exceeding an error threshold V_T is detected.

Taking into account of the accuracy level that is required to safely manage Li-ion cells [23], and the declared maximum error of the IC, an error threshold $V_T = 10$ mV is considered in this paper.

Considering the above failure criteria, DPI tests have been performed for each test frequency in the 1 MHz to 2 GHz bandwidth by increasing the injected RF incident power until a failure is detected. Notice that the IEC 62132-4 frequency bandwidth (1 MHz–1 GHz) has been extended to

2 GHz to include the 1.8 GHz frequency, widely employed in wireless communications. The minimum RF incident power giving rise to the failure is then reported as the DPI immunity level at the test frequency. If no failure is detected at the maximum test incident power $P_{\max} = 37$ dBm, no immunity level indication is reported. The results of DPI tests performed according with the above procedure are presented in the next Section.

4. DPI Experimental Results

The DPI immunity tests on the DUT cell inputs and SPI injection points in Figure 2 are reported in this Section. The different failure mechanisms observed are highlighted and the effectiveness of PCB level filtering on cell inputs is discussed.

4.1. Injection of Cell Inputs

The EMI robustness of the DUT undergoing DPI on the cell input injection point is considered comparing a differential (DM) excitation and a common-mode (CM) one. Differential (DM) excitation is performed by connecting only the injection capacitor C_{inj}^+ to the signal terminal of the SMA connector in Figure 2. Common-mode (CM) excitation is performed by connecting both the injection capacitors C_{inj}^+ and C_{inj}^- to the SMA signal line. Both the tests have been repeated without the RC filters in Figure 2 (i.e., using 0 Ω 0603 SMD resistors and not mounting the filter capacitors) and with the 100 Ω –100 nF RC filters prescribed by the IC manufacturer.

The respective measurement results are reported in Figure 4. The DPI immunity level of the DUT without filters is very similar for CM and DM injection and it is mostly in the range of 5–15 dBm over the 1 MHz to 1 GHz bandwidth. A very high susceptibility to EMI (immunity level of less than 0 dBm) can be observed at 16 MHz and harmonic frequencies, which are likely to be related with the internal clock frequency of the sigma-delta converter built-in the BMS IC. As such, EMI-induced failures do not seem to be specifically related to EMI superimposed onto the differential cell voltage to be acquired, but rather to other mechanisms involving the RF voltage between each test pin and the IC reference (ground) voltage.

The presence of RC filters provides a significant immunity enhancement in the 20–600 MHz band (a single failure is experienced at 150 MHz at the 37 dBm test level), whereas their effectiveness is lower above 600 MHz. This can be explained by considering that the impedance of the 0603, 100 nF capacitor of the filter, dominated above 20 MHz by the parasitic inductance $ESL \simeq 1$ nH, in series with the PCB track and via inductance ($L_{\text{track}} \simeq 1$ nH and $L_{\text{via}} \simeq 1$ nH), gives rise to a parallel resonance with the input capacitance of the BMS IC ($C_{\text{IN}} \simeq 15$ pF from S-parameters measurements) at a frequency:

$$f_0 = \frac{1}{2\pi\sqrt{(ESL + L_{\text{track}} + L_{\text{via}})C_{\text{IN}}}} \simeq 700 \text{ MHz}. \quad (1)$$

Close to this frequency, the actual impedance of the parallel element of the RC filter (capacitor C and parasitics) is very high and its filtering effectiveness is therefore impaired.

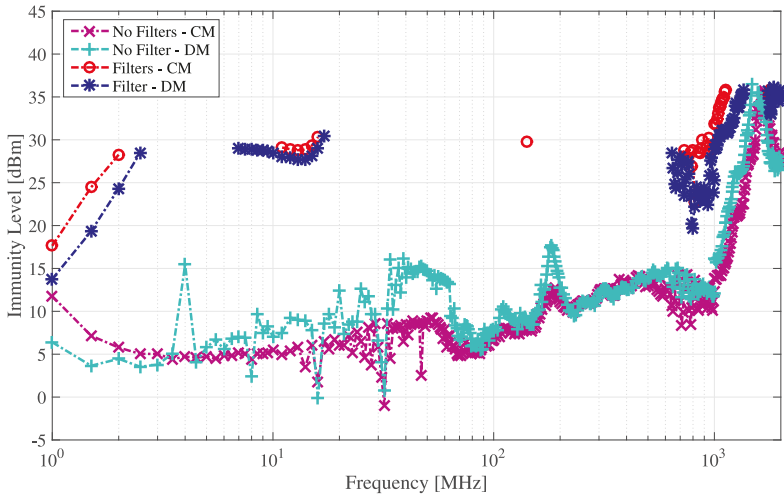


Figure 4. Measured immunity level (expressed in terms of RF incident power) for DPI on the cell input pins: differential (DM) and common-mode (CM) injection, with and without RC 100 Ω, 100 nF RC filters in Figure 2.

4.1.1. Test Port Voltage Estimation

To gain further insights into the intrinsic susceptibility level of the IC and the effectiveness of the filters, the peak RF voltage at the test board injection port giving rise to the failures reported in Figure 4 has been estimated on the basis of the reflection coefficient Γ at the test board injection port, measured by a calibrated vector network analyzer (VNA). Taking into account that the peak RF voltage at the test port V_{rf} can be expressed in terms of the RF incident power P_{inc} as

$$V_{rf} = |1 + \Gamma| \sqrt{2R_G P_{inc}}, \quad (2)$$

where $R_G = 50 \Omega$ is the reference port resistance, the incident power immunity levels have been translated into the corresponding test port voltages in Figure 5. On this basis, it can be noticed that an injected RF voltage with a peak amplitude even lower than 1 V (lower than 0.5 in the worst case) is sufficient to induce a failure in the BMS IC without filters. Moreover, by comparing the failure levels in Figure 4, expressed in terms of incident power, and the results in Figure 5, expressed in terms of injection port voltage, it can be appreciated that the immunity enhancement brought by the filters in the 800 MHz to 2 GHz range is much lower if expressed in terms of the injection port voltage than in terms of incident power, and both the filtered and the unfiltered ICs undergo a failure for an injected EMI peak amplitude of about 3 V.

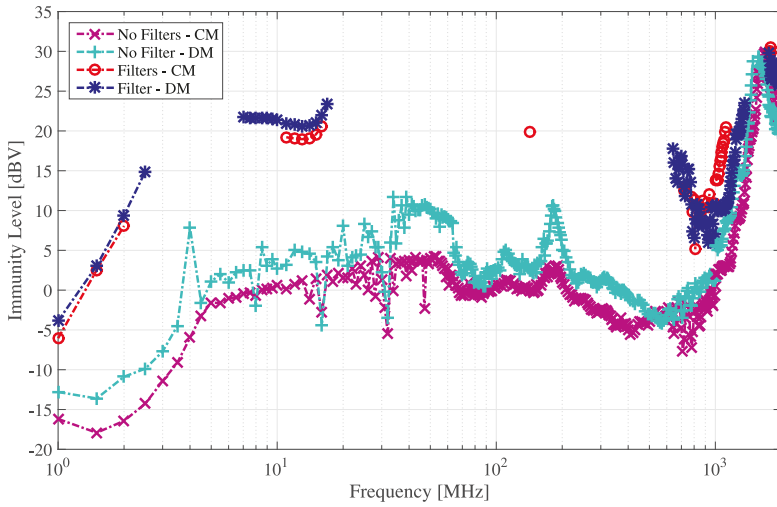


Figure 5. Total RF voltage induced at the DPI injection port corresponding to the DPI immunity levels in Figure 4.

4.1.2. Failure Mechanisms

During EMI induced failures reported in Figure 4, no SPI communication failure (inconsistent PEC) was reported when performing DPI injection on the cell inputs. In all cases, in fact, failures events were related to an EMI-induced offset exceeding 10 mV in the cell voltage readings. Such an offset voltage, defined for each cell i as

$$V_{OFF,i} = V_{ADC,i,EMI} - V_{ADC,i} \tag{3}$$

where $V_{ADC,i,EMI}$ is the i -th cell voltage acquired by the DUT while injecting an RF power corresponding to the immunity level in Figure 4, and $V_{ADC,i}$ is the voltage of the same cell acquired by the DUT without RF power injection, is plotted for each cell in Figure 6 for the unfiltered IC, and in Figure 7 for the IC including RC filters. In both cases, DM injection is considered.

Figure 6 shows how that failures up to about 300 MHz are related to an EMI-induced offset exceeding 10 mV in the acquired voltage of cell #6; i.e., on the cell on which DPI is performed. On the contrary, for EMI frequencies above 300 MHz, all the acquired cell voltages show a similar offset. Such a behavior can be related to the direct propagation of EMI to the internal ADC and/or to its reference voltage source.

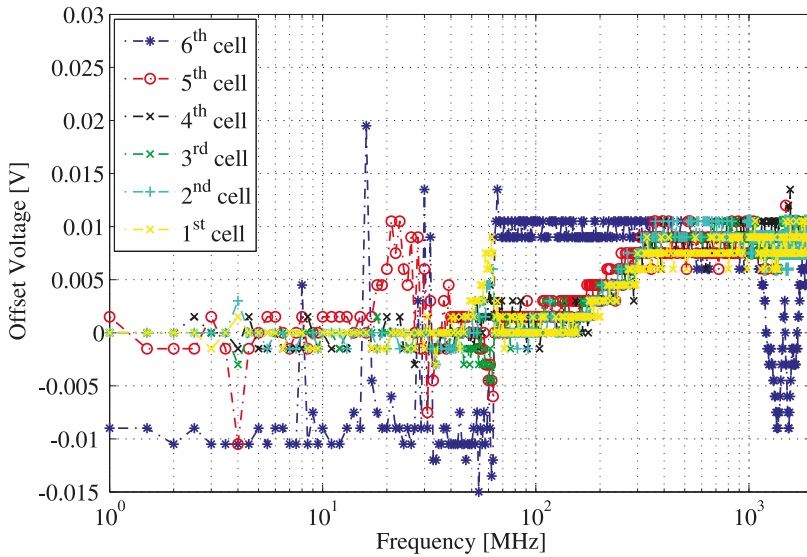


Figure 6. EMI-induced offset in the cell voltage readings obtained in accordance with DPI failure levels of Figure 4 (DM injection performed on the 6th cell positive terminal, without RC filters).

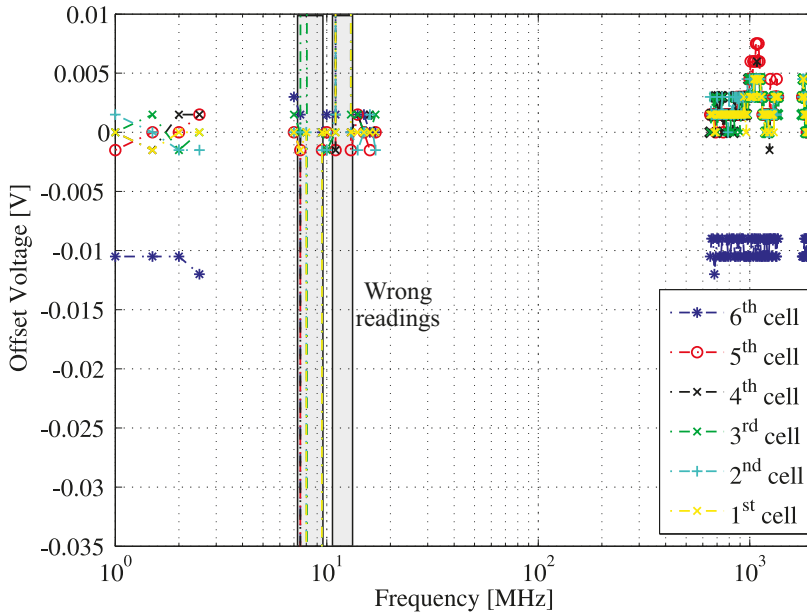


Figure 7. EMI-induced offset in the cell voltage readings obtained in accordance with DPI failures level of Figure 4 (DM injection performed on the 6th cell positive terminal, with RC filters).

Figure 7 shows a different failure mechanism for the filtered device undergoing RF DPI in the 8–12 MHz band (reported as a *wrong reading* gray area). In this case, injected EMI gives rise to completely wrong ADC readings, corresponding to the maximum or to the minimum values of the ADC range.

At lower and higher frequencies the failure mechanisms related to the offset presence are observed. Similar results have been obtained performing CM injection.

Finally, the DC current delivered by the battery pack and measured by the DC amper meter (see Figure 3) in accordance with the DPI failure levels shown in Figure 4, is plotted in Figure 8 for DM DPI performed without (a) and with (b) the RC input filters in Figure 2. Notice that such a current does not include the DC current sunk by the IC for its operation, and no external load is connected to the cells. Figure 8 shows how such a DC current delivered by the battery pack in accordance with the DPI failure levels, (whose measured value without EMI is about 170 μA), can be significative of being affected by the injected disturbances if the RC filters are not included, reaching 6 mA for a 40 MHz EMI injection frequency. It is interesting to observe that the measured DC current is negative (current delivered to the battery pack) for most EMI injection frequencies.

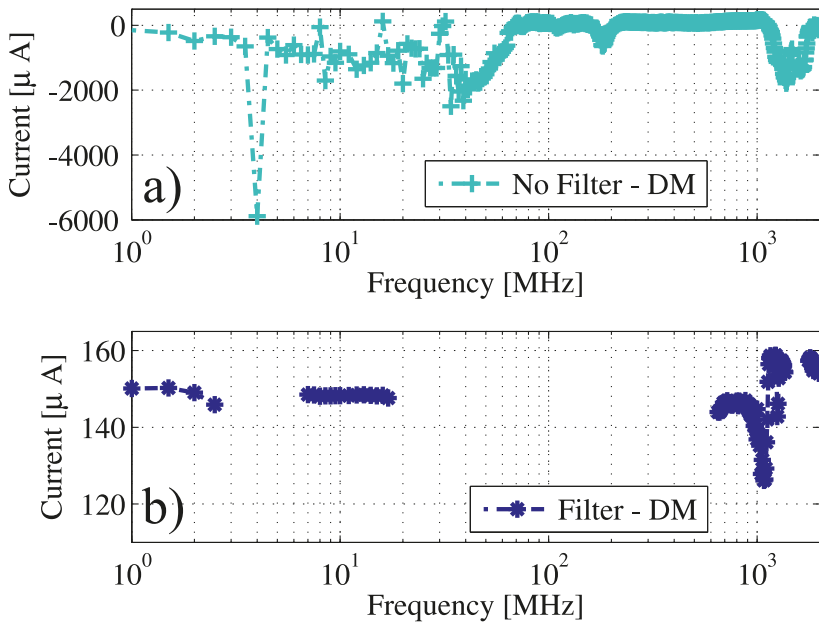


Figure 8. DC current absorbed from the battery pack by the BMS IC cell inputs in accordance with DPI failures levels in Figure 4 for DM injection performed on the 6th, without (a) and with (b) the RC filters.

4.2. SPI Injection

The immunity level of the DUT undergoing DPI on the SPI injection point in Figure 2 has also been investigated. Figure 9 reports measurement results for RF injections performed on the four SPI lines at the same time and injection performed on the SCK (serial clock) SPI line only. The respective total RF induced voltage at the same pins is reported in Figure 10. In the first case the four SPI injection capacitors to the signal terminal of the SMA connector in Figure 2 are all connected. In the latter case, only one injection capacitor between the signal terminal of the SMA connector in Figure 2 and the SCK pin of the IC is mounted on the PCB.

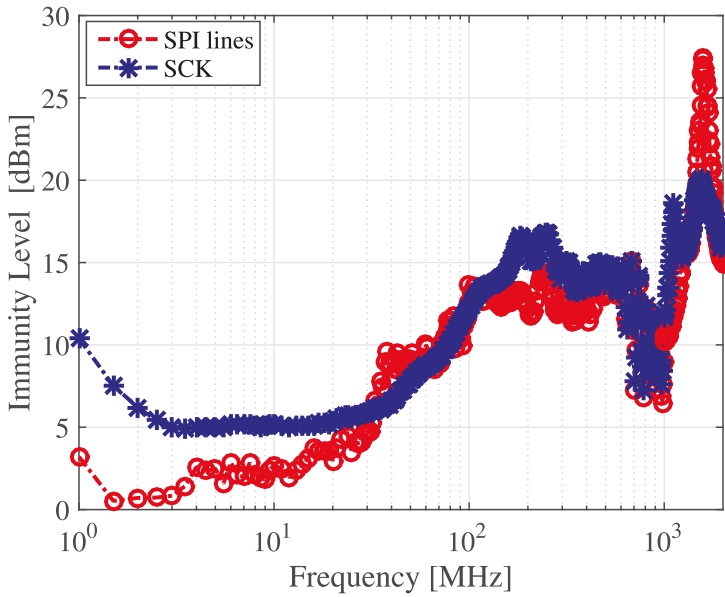


Figure 9. Measured immunity level for DPI on the SPI input pins: simultaneous injection on the four SPI lines and injection on the single SCLK line.

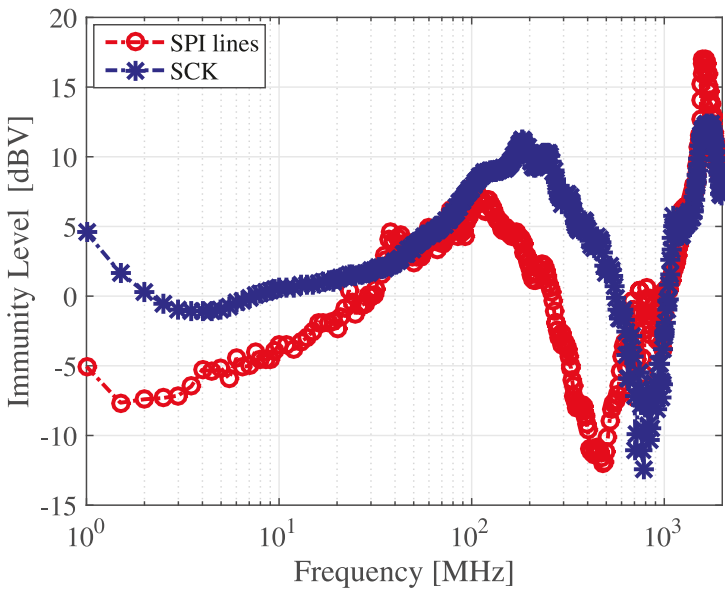


Figure 10. Total RF voltage induced at the SPI input pins: simultaneous injection on the four SPI lines and injection on the single SCLK line.

Failure Mechanisms

By comparing the immunity level reported in Figure 9 for the SPI injection with the immunity level reported in Figure 4 for cell inputs injection, it can be highlighted that the immunity level for SPI injection is lower than the immunity level of the unfiltered cell inputs. This is a serious concern, since the EMI immunity for SPI injection cannot be improved by filtering [16] because EMI filters would give rise to an unacceptable degradation of nominal digital waveforms.

An analysis of the mechanisms giving rise to EMI-induced failures when DPI is performed on SPI lines has been carried out on the basis of the data retrieved during the DPI tests, in analogy to what was discussed in Section 4.1.2. Based on these data, failures below 100 MHz are related, as one could expect, to errors in the SPI transmission detected by checking the PEC code. At higher frequency, however, EMI failures for SPI injection are related to an offset in the acquired cell voltages, equal for all the six cells, as shown in Figure 11. Such a behavior, which is similar to what was highlighted for DPI on the cell inputs in the high frequency range (Figure 6), can be related to EMI propagation inside the DUT to the internal ADC and/or to its reference voltage source.

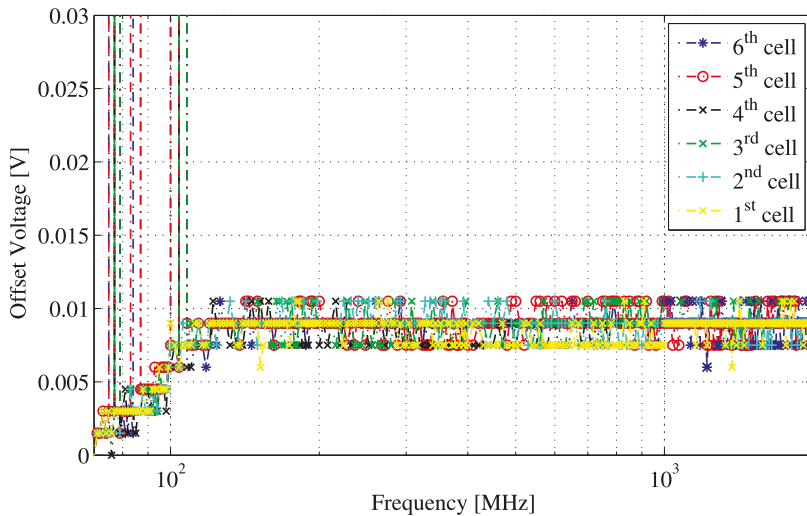


Figure 11. EMI-induced offset in the cell voltage readings obtained in accordance with failure levels of Figure 9 above 50 MHz (simultaneous injection on the four SPI pins).

5. Discussion: DPI Tests

DPI measurements have been performed in the bandwidth 1 MHz to 2 GHz up to a maximum incident power of 37 dBm on a commercial BMS. A test board has been specifically designed and fabricated in order to perform DPI in compliance with IEC 62132-4. In particular, DPI has been performed:

- On the cell monitoring inputs of the BMS IC connected to the top cell in the stack to be monitored (DM and CM injection), with and without RC low-pass filters recommended by the manufacturer;
- On the SPI lines.

During the tests, the following malfunctions in the operation of the BMS IC have been reported:

- Offset in the acquired cell voltages (considering that the target accuracy level of the IC an offset exceeding 10 mV has been considered as a failure);
- SPI communication failures (PEC failure and/or communication impaired).
- An increase in the current absorption from the power supply.

Offsets in acquired cell voltages have been reported both by DPI on the cell monitoring inputs and on the SPI communication lines. For what concerns cell monitoring input injection, an offset voltage has been reported for the cell undergoing injection, but also for other cells, depending on frequency. Communication failures have been reported for DPI in the communication lines only.

For what concerns DPI on cell monitoring inputs without the RC filters, a DPI immunity level from 5dBm to 15dBm has been reported up to 1 GHz. No substantial difference can be noticed for CM and DM injection. For what concerns DPI on cell monitoring inputs with the RC filters, a DPI immunity level exceeding the test level of 37 dBm has been reported for most frequencies above 5 MHz. Nonetheless, an immunity level as low as 20 dBm (for DM injection) has been reported in a frequency band around 700 MHz, in accordance with the parallel resonance of the filter capacitor (which is operating above its self-resonant frequency and shows an inductive impedance) and PCB parasitics. When filters were mounted, a slightly higher immunity level was measured for CM rather than for DM injection.

For what concerns DPI on SPI lines, a DPI immunity level lower than 5 dBm has been measured both at low frequency (<30 MHz) and in the bandwidth 700 MHz to 1 GHz. A slightly worse behavior has been reported for simultaneous injection on all the four SPI lines at the same time, rather than for injection performed on a single line. It is worth noting that unlike cells inputs, SPI communication lines cannot be filtered in order to avoid unacceptable degradation of the digital signal to be transmitted.

On the basis of the results of DPI tests, it can be observed that the immunity level of the BMS IC can be severely limited by its susceptibility to EMI superimposed onto the SPI line inputs.

6. Radiated Susceptibility Tests

In order to further investigate the BMS IC susceptibility, radiated EMI tests of a BMS IC have been performed in anechoic chamber in compliance with ISO11452-2 [26]. The DPI injection networks have been removed and the EMI filters on the cell inputs prescribed by the manufacturer have been included. The antenna has been placed both in front of the DUT and the cable harness. The DUT is located inside an anechoic chamber over a metal plane and it is remotely controlled and monitored by means of optical links. A sketch of the measurement setup is reported in Figure 12. The two terminals of the battery pack, monitored by the BMS, are connected through a 1.5 m-long cable to two LISNs. According to [26], the operation of the DUT has been tested radiating the DUT with a 200 V/m incident EM field, a typical test level for safety critical automotive applications, in the 200 MHz–1.4 GHz bandwidth, considering both horizontal and vertical polarization.

Figure 12 shows the radiated test setup with the antenna placed in front of the equipment under test (EUT corresponds to the PCB with the DUT and the battery pack). Referring to this test setup, the EMI-induced wrong readings (area in gray) and the offset in the cell voltage readings in the anechoic chamber for vertical and horizontal polarizations are reported respectively in Figures 13 and 14. Both for vertical and horizontal polarization, the radiated field gives rise to completely wrong ADC readings, corresponding to the maximum or to the minimum values of the ADC range for a frequency lower than 400 MHz in the gray area in both Figures 13 and 14). The same phenomena are also observed in the range 850–950 MHz for horizontal polarization. Moreover, the results of radiated tests in Figures 13 and 14 highlight an EMI-induced offset in the acquired voltages in the range 650–900 MHz.

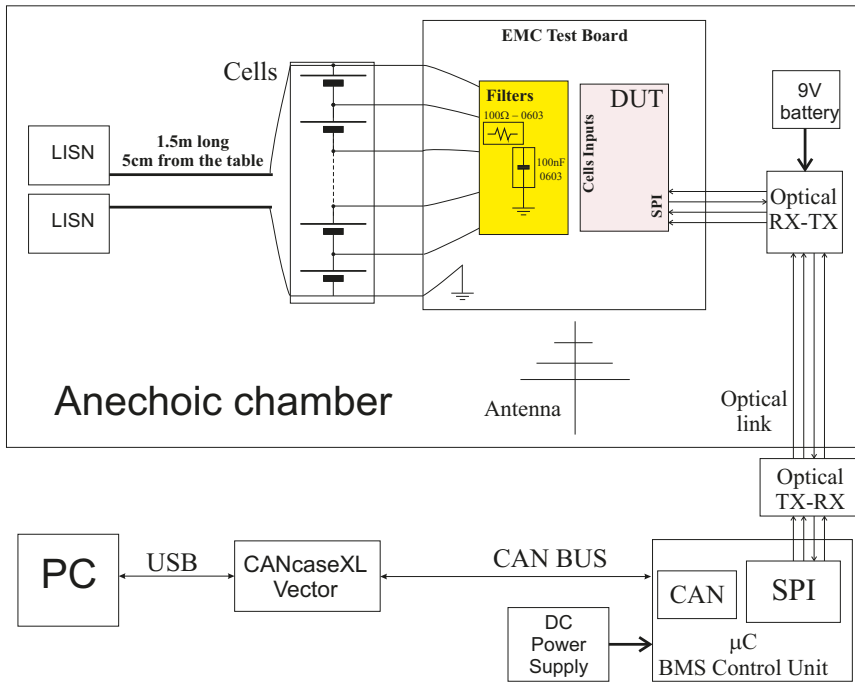


Figure 12. Radiated susceptibility test setup. Antenna in front of the equipment under test (EUT).

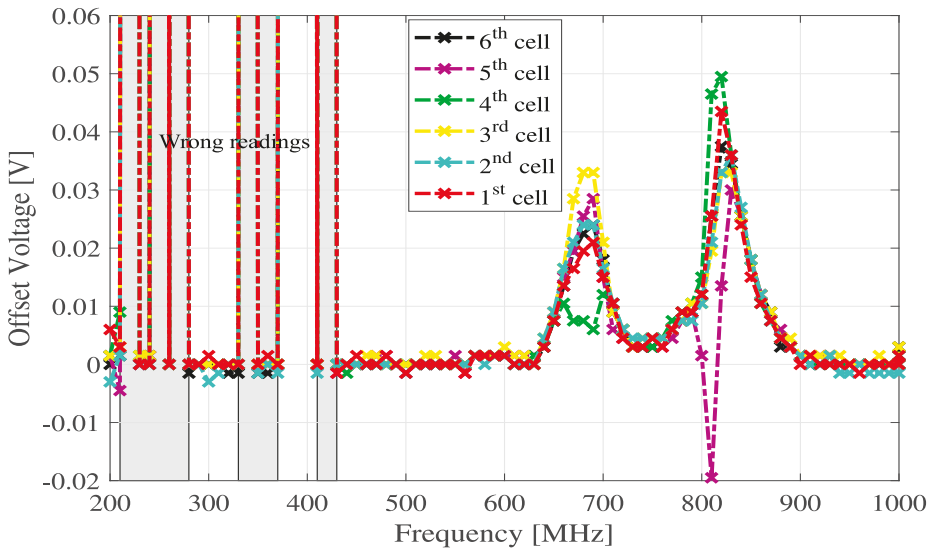


Figure 13. EMI-induced offset in the cell voltage readings. Antenna in front of the EUT (Figure 12). Vertical polarization.

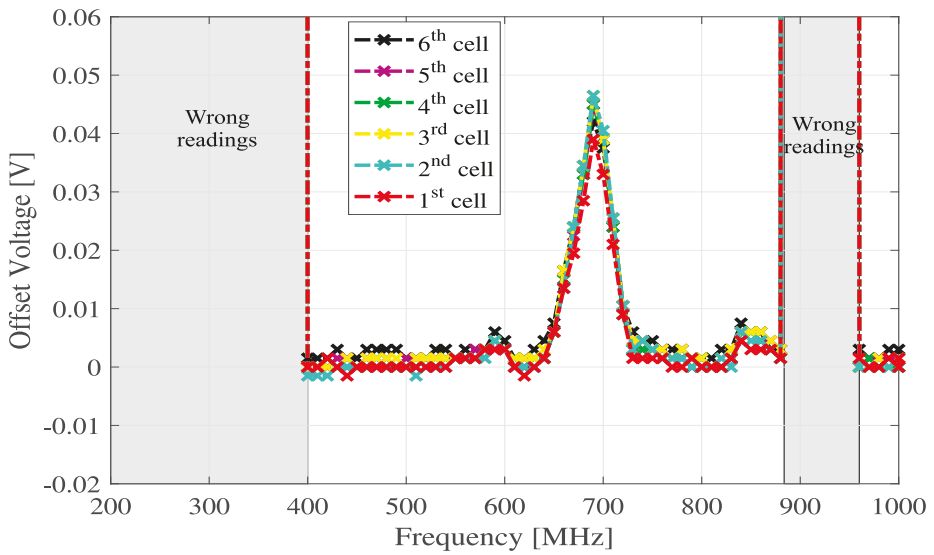


Figure 14. EMI-induced offset in the cell voltage readings. Antenna in front of the EUT (Figure 12). Horizontal polarization.

The same measurements have been repeated by moving the antenna in front of the cable, obtaining a similar phenomena. The respective wrong readings and EMI-induced offsets in the cell voltage readings in the anechoic chamber for vertical and horizontal polarizations are reported respectively in Figures 15 and 16.

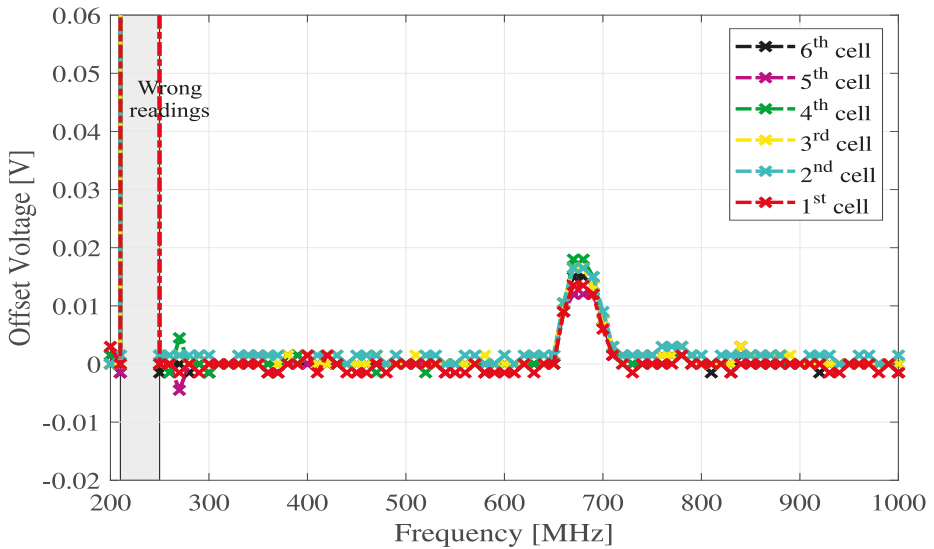


Figure 15. EMI-induced offset in the cell voltage readings. Antenna in front of the cable. Vertical polarization.

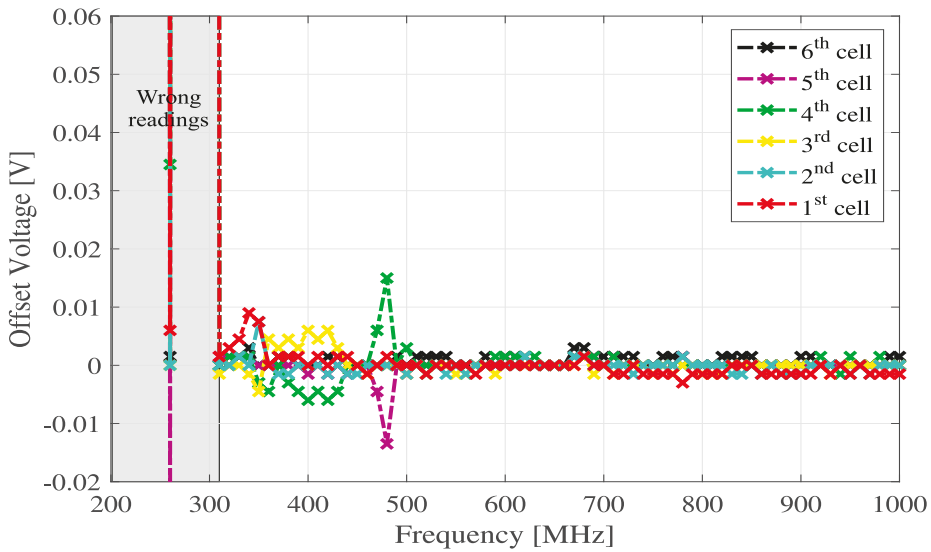


Figure 16. EMI-induced offset in the cell voltage readings. Antenna in front of the cable. Horizontal polarization.

7. Discussion: DPI vs. Radiated Immunity Tests

The radiated susceptibility measurements performed in compliance with ISO 11425-2 [26] aimed for establishing a correlation between the EMC performance of the BMS IC, previously assessed by the DPI method, and the susceptibility to EMI of a realistic BMS system IC. For a direct comparison, Figure 17 reports the immunity level measured by DPI tests on cell inputs (Figure 4)—its respective peak value in volts (from Figure 5)—and on the SPI lines (Figure 9); see Figure 17a–c respectively. Moreover, see the EMI-induced offsets in acquired cell voltages measured during radiated susceptibility tests in Figure 17d,e—for vertical and horizontal polarizations with the antenna placed in front of the EUT, respectively.

To obtain an approximate relation between DPI immunity level and radiated field strength, it has been observed that the failure threshold considered in DPI tests (EMI-induced offset in acquired cell voltages equal to 10 mV) has been reached irradiating the EUT in the bandwidth from 600 to 900 MHz by a vertically polarized E field $E_v = 100$ V/m, which approximately induces a CM voltage on the BMS PCB lines connected to the cell inputs with a peak amplitude

$$V_{cm} = \int_0^h E_z(z) dz \simeq E_v \cdot h = 8.5 \text{ V}, \tag{4}$$

where $h = 8.5$ cm is the height of the harness connecting the BMS to the cells with respect to the ground plane. The EMI amplitude estimated by (4) is consistent with the results of the DPI immunity test reported in dBm and in volts as EMI peak amplitudes, respectively, in Figure 17a,b. In fact, in the bandwidth around 700 MHz where the effectiveness of RC filters is impaired by the resonance highlighted in (1), the EMI immunity level both for CM and DM injections is similar to that defined in (4).

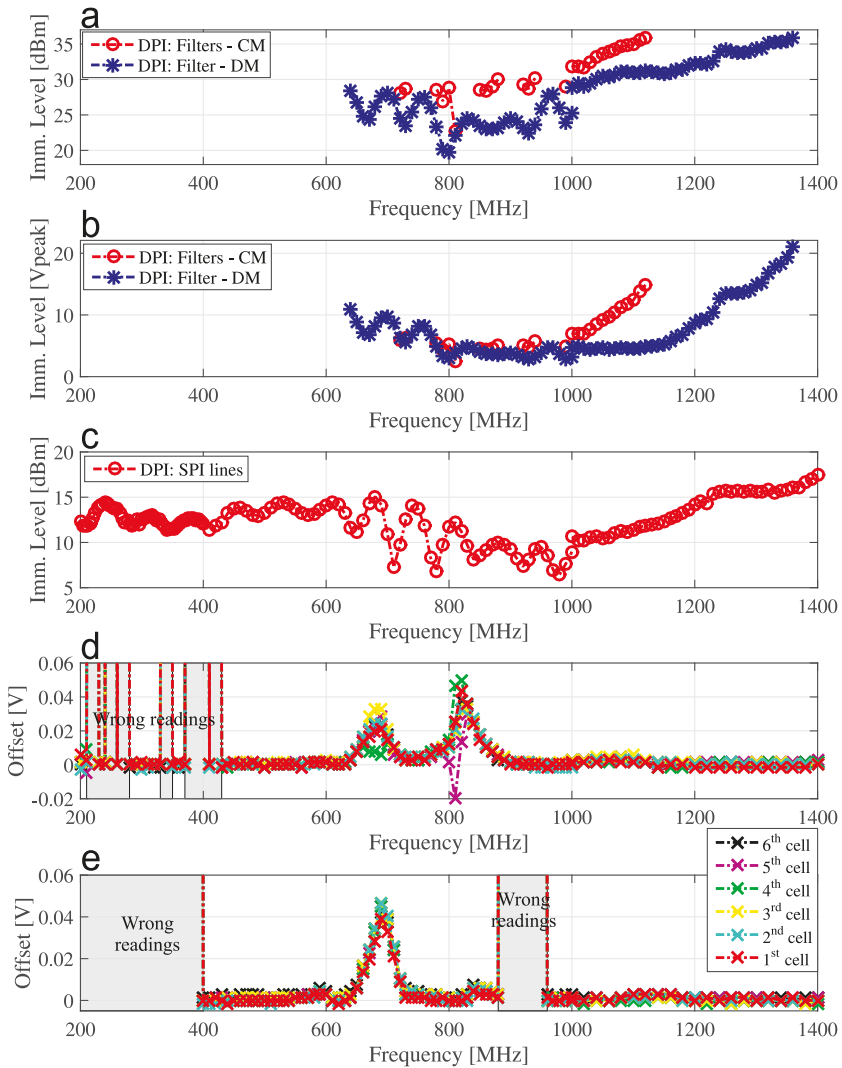


Figure 17. (a) Measured immunity level for DPI on the cell input pins: differential (DM) and common-mode (CM) injection, with 100 Ω , 100 nF RC filters in Figure 2, and (b) respective EMI peak amplitudes. (c) Measured immunity level for DPI on the four SPI lines. (d) EMI-induced offset in the acquired cell voltages, $E = 200$ V/m. Vertical polarization. (e) EMI-induced offset in the acquired cell voltages, $E = 200$ V/m, horizontal polarization.

Considering the significant differences of the injection mechanisms and of the test setup in DPI and radiated tests, further considerations on the correlation between IC-level DPI test results and system-level radiated immunity tests are difficult to be established and are also scarcely significant, since the results of radiated tests could be strongly influenced by the actual structure of the battery pack, including the BMS, which, in real applications, could be rather different with respect to the prototype considered in our investigation. Nonetheless, the same failure mechanisms (offset in acquired cell

voltages and SPI communication failures) and the same critical EMI bandwidth highlighted during DPI tests have been found in system level tests.

In particular, an offset voltage of 10 mV, corresponding to the susceptibility level considered in DPI tests, has been observed by irradiating the system with an antenna placed in front of the EUT with a vertical polarization for a test frequency from 600–900 MHz. Considering that the board undergoing radiated tests includes the RC filters, such results are consistent with the results of DPI according to which the immunity of the EUT is particularly critical in the bandwidth around 700 MHz, where an immunity level of about 20 dBm was reported.

8. Conclusions

The susceptibility to EMI of a BMS front-end IC for EVs and HEVs has been investigated in this paper by DPI tests performed according with IEC 62132-4. On the basis of the experimental results, it has been highlighted that the BMS IC under test can be significantly susceptible to EMI injected on its cell input terminals and on its digital communication (SPI) lines. For what concerns cell inputs injection, in particular, it has been observed that low pass RC filtering can be effective at improving the immunity to EMI of the DUT in the 10–600 MHz bandwidth, but its effectiveness is reduced above 600 MHz. On the other hand, the susceptibility to EMI applied on the SPI input lines, which cannot be filtered, is likely to be a major concern for the specific application. Finally, the different mechanisms giving rise to EMI induced failures of the specific DUT have been highlighted. Depending on the EMI frequency and on the injection points, an EMI-induced offset in the cell readings, SPI failures and completely wrong acquired values have been reported. An abnormal current absorption from the cells while performing DPI has also been observed.

The immunity to EMI of the same BMS system has been addressed even by radiated susceptibility measurements performed in compliance with ISO 11425-2 to establish a correlation between the EMC performance of the BMS IC, previously assessed by the DPI method, and the susceptibility to EMI of a realistic BMS system based on the same IC. During the radiated tests, which have been performed for a field strength of 200 V/m, the same failure mechanisms highlighted during DPI tests have been observed (offset in acquired cell voltages and SPI communication failures).

Funding: The lab activities have been supported by the Regione Piemonte within the Biomethair Project, Fondo Europeo P.O.R. 2007–2013.

Acknowledgments: The author thanks P. Crovetto and F. Fiori from Politecnico di Torino, Italy, who supported a preliminary conference paper [4], and Eng. G. Borio, M. Scaglione, and A. Bertino of the LACE, Torino, Italy, for setting up the test bench used for the radiated emission measurements.

Conflicts of Interest: The author declares no conflict of interest.

References

1. Richelli, A.; Colalongo, L.; Kovács-Vajna, Z.M. Analog ICs for Automotive under EMI Attack. In Proceedings of the 2019 AEIT International Annual Conference, Florence, Italy, 18–20 September 2019; pp. 1–6.
2. Aiello, O.; Fiori, F. On the Susceptibility of Embedded Thermal Shutdown Circuit to Radio Frequency Interference. *IEEE Trans. EMC* **2012**, *54*, 405–412. [[CrossRef](#)]
3. Aiello, O. Hall-Effect Current Sensors Susceptibility to EMI: Experimental Study. *Electronics* **2019**, *8*, 1310. [[CrossRef](#)]
4. Aiello, O.; Crovetto, P.S.; Fiori, F. Susceptibility to EMI of a Battery Management System IC for electric vehicles. In Proceedings of the 2015 IEEE International Symposium on Electromagnetic Compatibility (EMC), Dresden, Germany, 16–22 August 2015; pp. 749–754.
5. Aiello, O.; Fiori, F. A New MagFET-Based Integrated Current Sensor Highly Immune to EMI. *Microelectron. Reliab.* **2013**, *53*, 573–581. [[CrossRef](#)]
6. Aiello, O.; Fiori, F. A new mirroring circuit for power MOS current sensing highly immune to EMI. *Sensors* **2013**, *13*, 1856–1871. [[CrossRef](#)] [[PubMed](#)]

7. Mutoh, N.; Nakanishi, M.; Kanesaki, M.; Nakashima, J. EMI noise control methods suitable for electric vehicle drive systems. *IEEE Trans. Electromagn. Compat.* **2005**, *47*, 930–937 [[CrossRef](#)]
8. Ansean, D.; García, V.M.; González, M.; Blanco-Viejo, C.; Viera, J.C.; Pulido, Y.F.; Sánchez, L. Lithium-Ion Battery Degradation Indicators Via Incremental Capacity Analysis. *IEEE Trans. Ind. Appl.* **2019**, *55*, 2991–3002. [[CrossRef](#)]
9. Omariba, Z.B.; Zhang, L.; Sun, D. Review on Health Management System for Lithium-Ion Batteries of Electric Vehicles. *Electronics* **2018**, *7*, 72. [[CrossRef](#)]
10. Lelie, M.; Braun, T.; Knips, M.; Nordmann, H.; Ringbeck, F.; Zappen, H.; Sauer, D.U. Battery Management System Hardware Concepts: An Overview. *Appl. Sci.* **2018**, *8*, 534. [[CrossRef](#)]
11. Chen, C.L.; Wang, D.S.; Li, J.J.; Wang, C.C. A Voltage Monitoring IC With HV Multiplexer and HV Transceiver for Battery Management Systems. *IEEE Trans. VLSI* **2015**, *23*, 244–253. [[CrossRef](#)]
12. Chol-Ho, K.; Moon-Young, K.; Gun-Woo, M. A Modularized Charge Equalizer Using a Battery Monitoring IC for Series-Connected Li-Ion Battery Strings in Electric Vehicles. *IEEE Trans. Power Electron.* **2013**, *28*, 3779–3787.
13. Cheng, K.W.E.; Divakar, B.P.; Wu, H.; Ding, K.; Ho, H.F. Battery-Management System (BMS) and SOC Development for Electrical Vehicles. *IEEE Trans. Veh. Technol.* **2011**, *60*, 76–88. [[CrossRef](#)]
14. Spadacini, G.; Pignari, S.A. Numerical Assessment of Radiated Susceptibility of Twisted-Wire Pairs With Random Nonuniform Twisting. *IEEE Trans. EMC* **2013**, *55*, 956–964. [[CrossRef](#)]
15. Richelli, A. EMI Susceptibility Issue in Analog Front-End for Sensor Applications. *J. Sens.* **2016**, *2016*, 1082454. [[CrossRef](#)]
16. Crovetto, P.; Fiori, F. IC digital input highly immune to EMI. In Proceedings of the 2013 International Conference on Electromagnetics in Advanced Applications (ICEAA), Torino, Italy, 9–13 September 2013; pp. 1500–1503.
17. Richelli, A.; Matiga, G.; Redoute, J.M. Design of a Folded Cascode Opamp with Increased Immunity to Conducted Electromagnetic Interference^o in 0.18 um. *Microelectron. Reliab.* **2015**, *55*, 654–661. [[CrossRef](#)]
18. Richelli, A.; Delaini, G.; Grassi, M.; Redoute, J.M. Susceptibility of Operational Amplifiers to Conducted EMI Injected Through the Ground Plane into Their Output Terminal. *IEEE Trans. Reliab.* **2016**, *65*, 1369–1379. [[CrossRef](#)]
19. Andrea, D. *Battery Management Systems for Large Lithium-Ion Battery Packs*; Artech House Inc: Boston, MA, USA, 2010.
20. Jiang, J.; Zhang, C. *Fundamentals and Applications of Lithium-Ion Batteries in Electric Drive Vehicles*; John Wiley & Sons Singapore Pte. Ltd.: Singapore, 2015.
21. Hauser, A.; Kuhn, R. 12—Cell balancing, battery state estimation, and safety aspects of battery management systems for electric vehicles. In *Advances in Battery Technologies for Electric Vehicles*; Scrosati, B., Garche, J., Tillmetz, W., Eds.; Woodhead Publishing: Cambridge, UK, 2015; pp. 283–326.
22. Lu, L.; Han, X.; Li, J.; Hua, J.; Ouyang, M. A review on the key issues for lithiumion battery management in electric vehicles. *J. Power Sources* **2013**, *226*, 272–288. [[CrossRef](#)]
23. Doughty, D.; Roth, P. A general discussion of Li-ion battery safety. *Electrochem. Soc. Interface* **2012**, *21*, 37–44.
24. IEC 623132-4:2006. Integrated Circuits, Measurement of Electromagnetic Immunity—Part 4: Direct RF Power Injection Method. Available online: <https://webstore.iec.ch/publication/6510> (accessed on 2 February 2020).
25. Generic IC EMC Test Specification, Ed. 2.1. 2017. Available online: http://www.zvei.org/fileadmin/user_upload/Presse_und_Medien/Publikationen/2017/Juli/Generic_IC EMC_Test_Specification/Generic_IC EMC_Test_Specification_2.1_180713_ZVEI.pdf (accessed on 19 January 2020).
26. Road Vehicles—Vehicle Test Methods for Electrical Disturbances from Narrowband Radiated Electromagnetic Energy, ISO Std. 11451-2. 2005. Available online: <https://www.iso.org/standard/37999.html> (accessed on 2 February 2020).



Article

EMI Susceptibility of the Output Pin in CMOS Amplifiers

Anna Richelli *, Luigi Colalongo and Zsolt Kovacs-Vajna

Department of Information Engineering, University of Brescia, 25123 Brescia BS, Italy; luigi.colalongo@unibs.it (L.C.); zsolt.kovacsvajna@unibs.it (Z.K.-V.)

* Correspondence: anna.richelli@unibs.it; Tel.: +39-030-371-5501

Received: 16 January 2020; Accepted: 5 February 2020; Published: 9 February 2020

Abstract: Measurements in commercial devices demonstrate a considerable susceptibility of the operational amplifiers to the electromagnetic interferences coupled to their output pin. This paper investigates some basic architectures starting from single stage amplifiers up to a whole operational amplifier. The result is a correlation between the different amplifier configurations, the output impedance and the susceptibility to the interferences. The simulations are performed by using the standard CMOS UMC 180nm technology and by running the netlist of the schematics extracted from the layout.

Keywords: Electromagnetic Interferences; Amplifiers; CMOS integrated circuits; susceptibility of the output pin

1. Introduction

The assessment of IC immunity to EMI is presently compulsory for many applications, because, thanks to the progress of VLSI, electronics is ubiquitous. It is evident in the following industries: computing, communication, manufacturing, transport, entertainment, business, health. We can find ICs nearly everywhere: in computers (of course), in cellphones, watches, medical devices, cars.... Moreover, in recent years, raises serious preoccupations on the vulnerability of electronic equipment to intentional EMI attacks [1–5]: sources capable of producing very high RF power over a wide frequency range are, indeed, presently easily available or even home-made manufacturable. In general, as shown in Figures 1 and 2, Electromagnetic Compatibility issues can be divided into two parts: emissions and susceptibility. Both of them should be as low as possible. This paper will focus on susceptibility, in particular of the analog ICs to conducted interferences. Due to the small dimensions of Integrated Circuits indeed, susceptibility and emission via conduction are more important than via radiation. The susceptibility of analog integrated circuits to conducted EMI has been modelled and verified with simulations as well as experimentally in several works, and analytical models predicting high-power EMI effects in CMOS operational amplifiers and offering a good matching with experimental results have been presented in [6]. On the other hand, the exact repercussion of electromagnetic interference (EMI), which is injected conductively into arbitrary pins of an integrated circuit (IC), is very hard to predict owing to the fact that all the existing coupling paths need to be taken into account [7]. Several works can be found in the literature, describing the susceptibility of analog ICs, as these are more sensitive to EMI. Most of this research focuses on operational amplifiers and other widely used analog blocks, such as for example voltage references, because of their high sensitivity to EMI and their prevalence in electronic circuits [8–15]. The EMI signals are considered directly injected into the gate of the differential pair or into the power supply pins (V_{dd} and V_{ss}). On the other hand, all the pins can be a possible injection point as demonstrated, for example in [16], where the susceptibility of a bulk-driven CMOS amplifier is investigated by injecting the interferences into the bulk pin. Moreover, the direct

injection of the interferences is not the only path available for the EMI. Indeed in [17], the interferences reach the IC (a Local Interconnect Network (LIN) integrated output driver) by means of a parasitic capacitive coupling between the output pin and the conductive ground plane. The unwanted RF signals may indeed be transmitted through the copper plane, often shared with other analog, digital or mixed ICs, and can be capacitively coupled to all the pins, including the output one [18–20].

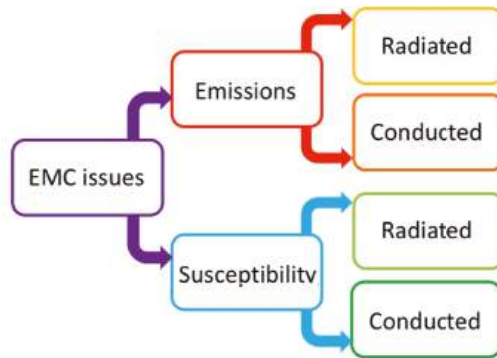


Figure 1. EMC issues.

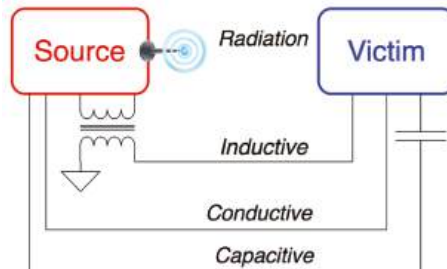


Figure 2. Possible coupling mechanisms for EMI attack.

Precisely, the susceptibility of the Operational Amplifiers to the Electromagnetic Interferences capacitively coupled to the output pin has been demonstrated in recent works [18–20], involving both commercial amplifiers and custom CMOS integrated ones. The results show a considerable vulnerability and exacerbate the scenario of EMI pollution. Moreover, it follows that the PCB ground plane, commonly shared with other analog, digital or mixed-signal circuits, can be a critical point of EMI pickup and injection. For the sake of clarity, the most relevant measurement results, provided by the literature [18,19], are plotted in Figures 3–8. The first four graphics show the EMI induced offset in well-known commercial amplifiers (ua741, OPA705, NE5534 and ICL7611). We can see that regardless the technology and the architecture of the amplifiers (bipolar, CMOS or BiCMOS), they are all susceptible to the interferences coupled to the output pin. Also, the offset is very high around the hundreds of MHz and it depends on the amplitude of the interferences. The second couple of figures refers to some commercial voltage references. They are very sensible to the EMI coupled to the output pin.

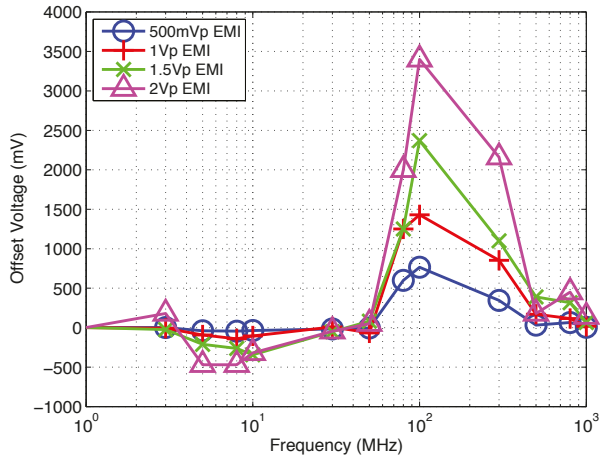


Figure 3. EMI induced offset in ua741: interferences coupled to the output pin.

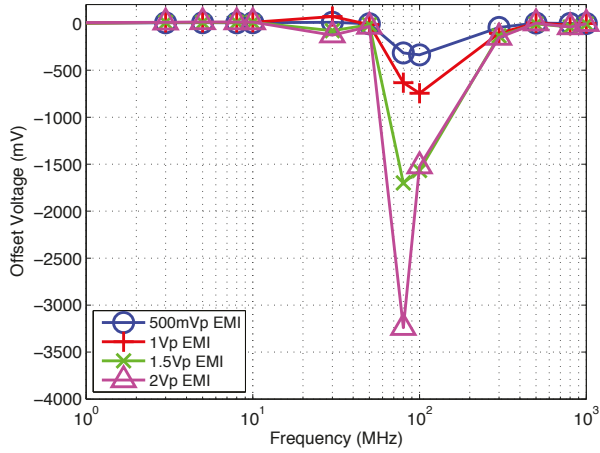


Figure 4. EMI induced offset in OPA705: interferences coupled to the output pin.

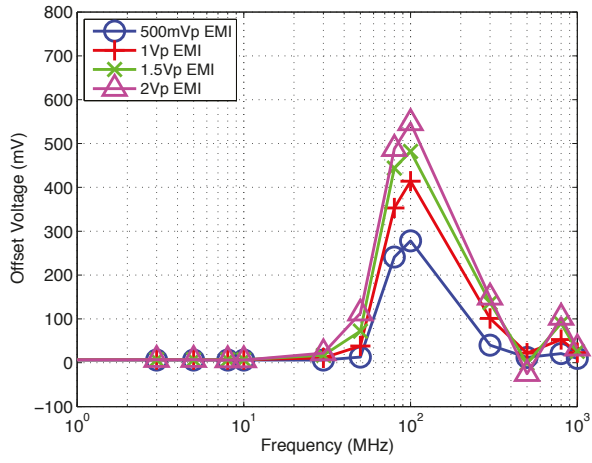


Figure 5. EMI induced offset in NE5534: interferences coupled to the output pin.

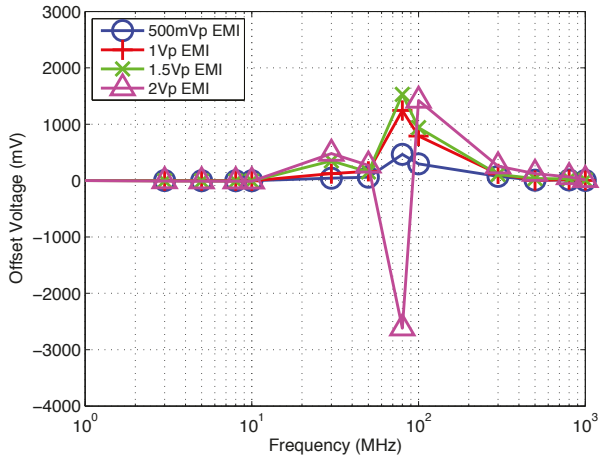


Figure 6. EMI induced offset in ICL7611: interferences coupled to the output pin.

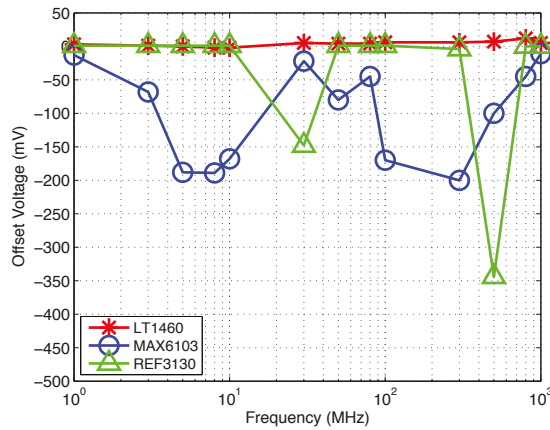


Figure 7. EMI induced offset in series voltage references: interferences coupled to the output pin.

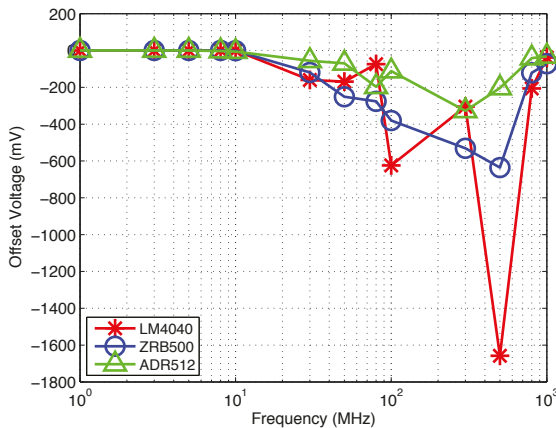


Figure 8. EMI induced offset in shunt voltage references: interferences coupled to the output pin.

Therefore, it is of paramount importance to deeply understand the reason of the susceptibility, the possible injection paths and the differences between the amplifier configurations. This paper has been organized as follows. In the second section, an overview about the simulation settings, the amplifier configurations and the transistors sizing will be provided; in the following section, a single stage common source amplifier will be studied when subjected to the EMI coupled to its output node (i.e., the drain terminal); in the fourth, fifth and sixth sections the same will be done for the other simple topologies (common gate, common drain and cascode, respectively); in Section 7 a two stages differential input Miller amplifier will be analyzed both in open loop and closed loop configurations. Finally, in Section 8, the discussion of the main results will be drawn and Section 9 concludes the paper.

2. Definition of the Simulation Settings

To reproduce the EMI pollution coming from the PCB, or from a generic ground plane or from close high-frequencies signal traces, an ideal sinusoidal voltage source is connected to the output pin

of the generic amplifier, by means of an ideal capacitor, representing the capacitive coupling. A few picofarad forms a realistic value of the parasitic capacitance between a middle length trace and the PCB ground plane, as stated in [21–23]. The amplifiers are designed in a standard CMOS technology (the UMC 180nm) and the simulations are performed using the software Virtuoso, developed by Cadence, and, in particular, the Analog Design Environment (ADE) tool. In this way, the investigation of the EMI effect can be carried out with the biggest flexibility. Indeed, the sizing of the transistors can be easily changed, all the possible configurations of the amplifier can be simulated and the effect of the amplitude and the frequency of the interferences can be easily checked. The experimental measurements offer more eminent and complete results, but in this technology the simulations and the measurements of susceptibility fit rather well, Ref. [18,20,24]. Moreover, the simulations (if well supported by the transistor models) are a powerful instrument to understand the possible reasons of the susceptibility. They indeed allow changing the conditions, the sizing, the settings, and so on..., and allow analyzing the effect of every change individually. Here, a list of the amplifier stages subjected to the interferences is briefly depicted. The DC and AC parameters and the transistor sizing are summarized in the following tables. The details on the circuit architectures, the schematics and the behavior of the amplifiers when subjected to the EMI are, instead, discussed in the corresponding sections. Table 1 refers to the common source stage shown in Figure 9; Table 2 summarizes the parameters of the common drain stage shown in Figure 10; in Table 3 the parameters of the cascode stage shown in Figure 11 are listed.

Table 1. DC and AC parameters and Transistor Sizing of the Common Source Stage.

	DC Biasing and AC Parameters	Components Sizing
Common Source with R (passive load)	VbiasN = 500 mV, 16 dB gain 1.5 MHz cut-off freq., 11 MHz GBW	W = 20 μm, L = 1 μm R = 10 kΩ
Common Source with PMOS (active load)	VbiasN = 500 mV, VbiasP = 1 V, 35 dB gain 180 kHz cut-off freq., 10 MHz GBW	Wn = 20 μm, Ln = 1 μm Wp = 20 μm, Lp = 1 μm

Table 2. DC and AC parameters and Transistor Sizing of the Common Drain Stage.

	DC Biasing and AC Parameters	Components Sizing
Common Drain with R (passive load)	VbiasN = 1.2 V, −1dB gain 13 MHz cut-off freq.	W = 20 μm, L = 1 μm R = 10 kΩ
Common Drain with NMOS (active load)	VbiasN = 1.2 and VbiasN2 = 500 mV, 0 dB gain 9.6 MHz cut-off freq.	Wn = 20 μm, Ln = 1 μm Wn2 = 20 μm, Ln2 = 1 μm

Table 3. DC and AC parameters and Transistor Sizing of the Cascode Stage.

	DC Biasing and AC Parameters	Components Sizing
Cascode with R (passive load)	VbiasN1 = 0.5 V, VbiasN2 = 1 V, 16 dB gain 1.5 MHz cut-off freq., 10 MHz GBW	Wn1,2 = 20 μm, Ln1,2 = 1 μm R = 10 kΩ
Common Drain with NMOS (active load)	VbiasN1 = 0.5 V, VbiasN2 = 1 V, VbiasP = 1.015 V 45 dB gain, 0.6 MHz cut-off freq., 10 MHz GBW	Wn1,2 = 20 μm, Ln1,2 = 1 μm Wp = 20 μm, Lp = 1 μm

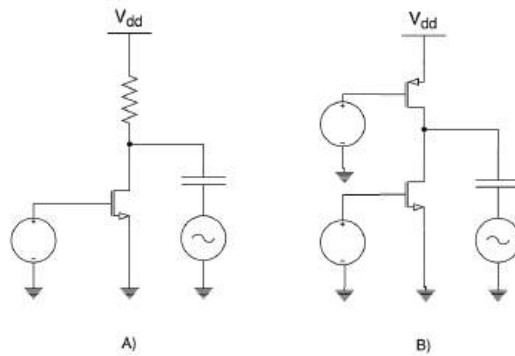


Figure 9. Schematics of the common source stage, with passive (A) and active (B) load respectively.

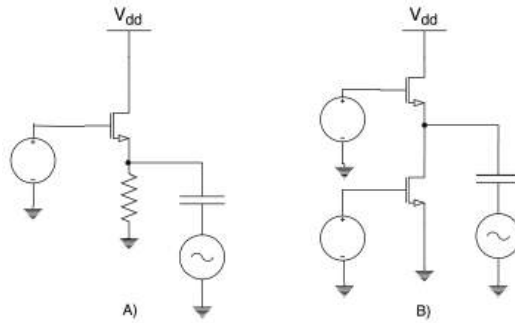


Figure 10. Schematics of the common drain stage, with passive (A) and active (B) load respectively.

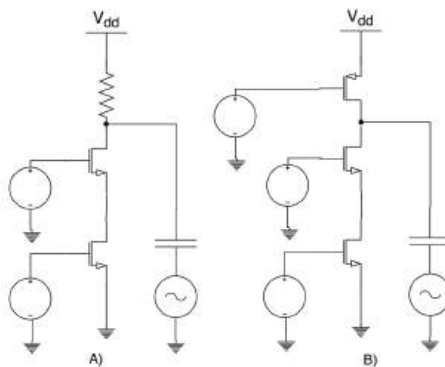


Figure 11. Schematics of the cascode stage, with passive (A) and active (B) load respectively.

3. Susceptibility of the Common Source Stage

As a first step, a common source stage (CS) is investigated. The CS amplifier is based on a NMOS transistor, designed in the standard CMOS UMC (United Microelectronics Corporation) 180 nm

technology; it is a N_18_MM device (which means regular threshold transistor for 1.8 V nominal voltage supply), with aspect ratio 20, length 1 μm and width 20 μm . The biasing point of the device is given by an ideal voltage source of 500 mV at the transistor gate and a resistor of 10 k Ω connected between the drain and the Vdd (1.8 V), as shown in Figure 9A. The resistor acts also as the active load of the CS stage. With the threshold of 374 mV, the biasing point sets the current at 57 μA and these small signal parameters: g_m 690 μS and g_{ds} 7.2 μS . As a single stage amplifier it exhibits a gain of 16 dB, a cut-off frequency of 1.5 MHz and a gain bandwidth product (GBW) of 11 MHz. The interference is represented by means of a sinusoidal signal with large amplitude and medium-large frequency. In particular, the amplitude is 1 V peak to peak and the frequency is ranging between 10 kHz and 10 GHz. The capacitive coupling versus the noisy ground plane is set to 1 pF. In this case, the common source amplifier exhibits a very low EMI induced offset (a few mV at maximum) and therefore a high immunity to the interferences coupled to the output pin. If a PMOS transistor takes the place of the resistor, as active load, the immunity changes. The new schematic is shown in Figure 9B. The resistive load has been substituted by an active load made of a PMOS transistor in saturation region, with the same aspect ratio of the NMOS counterpart. The gate of the PMOS is biased at 1V and the threshold voltage is around 500 mV. The operating point is slightly different to that of the first circuit and the current is now 54 μA . The small signal simulations show a gain of 35 dB, a cut-off frequency of 180 kHz and a GBW of 10 MHz.

In this second case (with active load), the common source stage presents a large susceptibility to the interferences coupled to its output pin. Indeed, the EMI induced offset on the output voltage reaches about 200 mV and it is rather large in a wide frequency range, starting from 500 kHz (offset is 100 mV) up to 10 GHz. The results of the simulations performed on both the amplifiers are shown in Figure 12. If the amplitude of interfering signal increases, the induced offset has a large raise, as expected. For example, if the EMI amplitude is 1 V, the maximum offset becomes 400 mV.

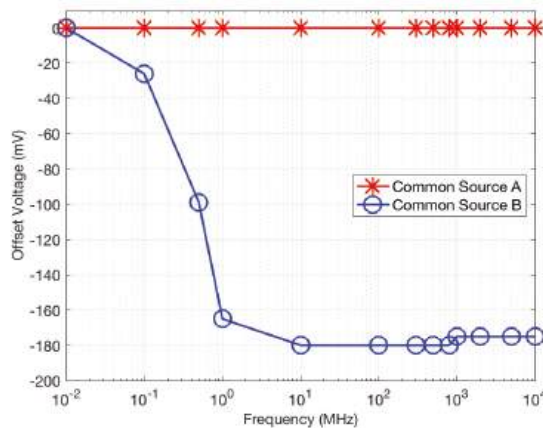


Figure 12. EMI induced offset in the common source stage.

4. Susceptibility of the Common Gate Stage

The behavior of the common gate stage (shown in Figure 13) is exactly the same of the common source stage. This is because the injection point (the drain of the transistor) is the same.

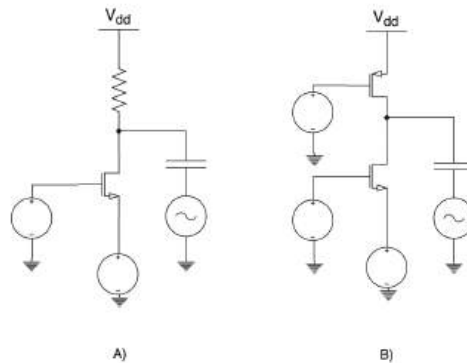


Figure 13. Schematics of the common gate stage, with passive (A) and active (B) load respectively.

5. Susceptibility of the Common Drain Stage

The behavior of the common drain stage is now investigated. The first case is the schematic shown in Figure 10A, with the resistive load.

The NMOS device is a regular threshold transistor, with aspect ratio 20, length $1\mu\text{m}$ and width $20\mu\text{m}$. The biasing point of the device is given by an ideal voltage source of 1.2 V at the transistor gate and a resistor of $10\text{ k}\Omega$ connected between the source and gnd acts as a passive load. In this operating point the small signal parameters are: g_m $763\ \mu\text{S}$ and g_{ds} $8.2\ \mu\text{S}$. The current is $68\ \mu\text{A}$ and the threshold voltage is 379 mV . The AC gain is -1 dB and the cut-off frequency is 13 MHz . The second case is the common drain with the active load (as in Figure 10B). The input transistor is biased at the same 1.2 V , while the active load NMOS is biased by an ideal voltage source of 0.5 V connected to its gate. The operating point is slightly different from that of case A: the current is now indeed $50\ \mu\text{A}$. The small signal parameters of the input transistor are now: g_m $635\ \mu\text{S}$ and g_{ds} $6.8\ \mu\text{S}$. The active load NMOS has similar parameters: g_m of $633\ \mu\text{S}$ and g_{ds} of $7.1\ \mu\text{S}$. The AC gain is 0 dB and the cut-off frequency is 9.6 MHz . To evaluate the susceptibility of the common drain stage the interferences are coupled to the transistor source (which is the output pin in this configuration) by means of a 1 pF capacitor. The EMI amplitude is 1 V peak to peak and the frequency is ranging between 10 kHz and 10 GHz . The results of the simulations performed on both the amplifiers are shown in Figure 14. As one can see both the schematics (A and B, with resistive or active load) are rather susceptible to the interferences, starting from a few MHz of the interfering signal frequency.

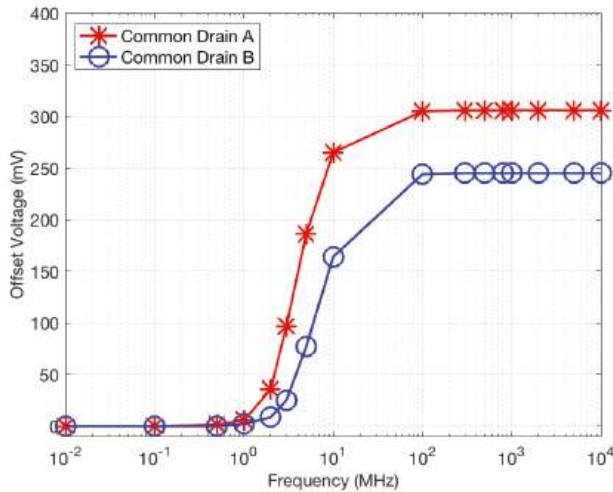


Figure 14. EMI induced offset in the common drain stage.

6. Susceptibility of the Cascode Stage

To have a complete overview of the single stage susceptibility, a cascode stage (common source + common gate) is also considered. The schematic is shown in Figure 11 with passive resistive load (A) and with active load (B). The transistors have always a length of 1 μm and a width of 20 μm . The common source transistor is biased with 0.5 V at the gate, while the common gate has a biased of 1V. The PMOS transistor in the schematic B is biased at 1.015 V in order to have operating points very similar between the circuits A and B, with the same current of about 50 μA and the same small signal parameters. In particular, the common source transistor has: g_m 633 μS and g_{ds} 7.1 μS . The common gate transistor has: g_m 633 μS and g_{ds} 7.4 μS . Finally, the active load PMOS transistor has: g_m 301 μS and g_{ds} 3.5 μS . In the first case (schematic A), the AC gain is 16 dB, the cut-off frequency is 1.5 MHz and the GBW is around 10 MHz. In the second case (schematic B), the AC gain is 45 dB, the cut-off frequency is 0.6 MHz and the GBW is around 10 MHz. The behavior of the cascode stage seems very similar to that of the common source stage. The circuit with passive load presents a negligible EMI-induced offset, while the circuit with active load is rather susceptible. The results of the simulations performed on both the amplifiers are shown in Figure 15.

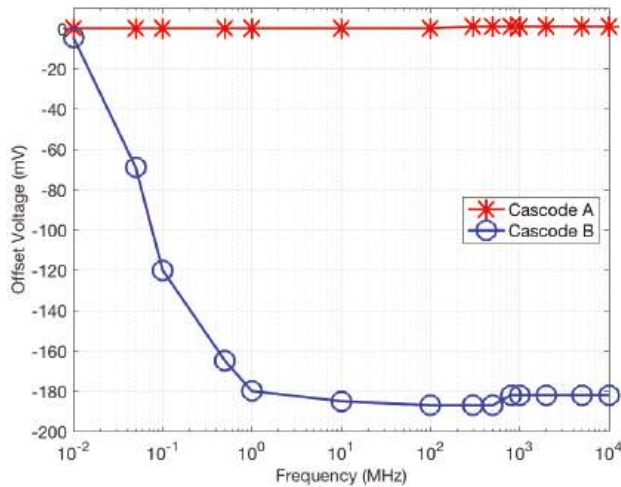


Figure 15. EMI induced offset in the cascode stage.

7. Susceptibility of a Two Stages Amplifier

The next step is to investigate the susceptibility of a two stages differential input single ended amplifier. Therefore, a Miller amplifier has been considered. The Miller amplifier is indeed one of the most common CMOS OpAmp. It is based on a differential input stage with single ended conversion which has a behavior similar to that of a common source stage. The second gain stage is usually a common source plus an active load. Sometimes, depending on the applications, a voltage buffer is added after the second stage, to have a low output impedance.

7.1. Susceptibility of a Two Stages Amplifier in Open Loop Configuration

In this subsection, we consider a two stages amplifier in an open loop. This is usually the case of an amplifier used as a comparator. The schematics of the circuits are shown in Figure 16. On the left (Figure A) there is the amplifier with a resistive load, while on the right (Figure B) there is the same amplifier with active load. Concerning the A circuit, the AC simulations show a gain of 55 dB, a cut-off frequency of 22 kHz, a GBW of 12 MHz. Regarding the B circuit, the gain is 72 dB (thanks to the active load), the cut-off frequency is 2.8 kHz and the GBW is 12 MHz. Although both the circuits are now used in an open loop configuration, they have a frequency compensation RC network that ensures 75° of phase margins if the circuits are in a closed loop. The main small signal parameters and the operating point are also listed in Table 4.

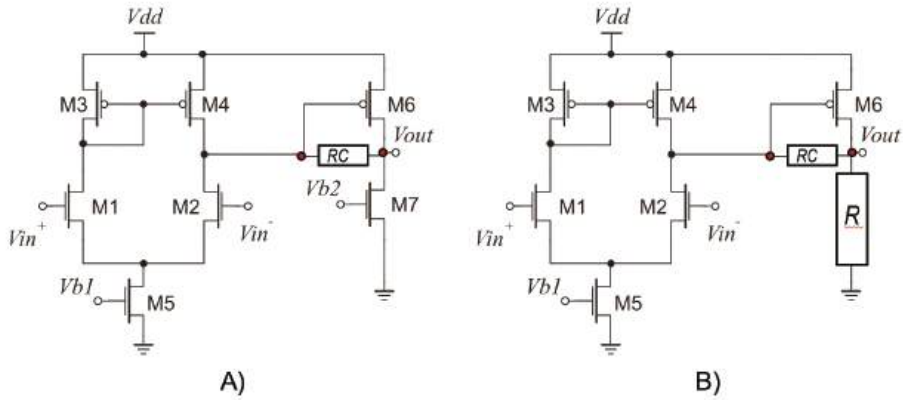


Figure 16. Schematic of the Miller amplifier: (A) with active load, (B) with resistive load.

Table 4. DC and AC parameters and Transistor Sizing of the Two Stages Amplifier.

	DC Biasing and AC Parameters	Components Sizing
Miller with R (passive load)	Vb1 = 1.16 V, 55 dB gain 22 kHz cut-off freq., 12 MHz GBW	Wn1,2 = 20 μm, Ln1,2 = 1 μm; Wp3,4,6 = 25 μm, Lp3,4,6 = 0.5 μm Wn5 = 20 μm, Ln5 = 1 μm; R = 10 kΩ
Miller with NMOS (active load)	Vb1 = Vb2 = 1.16 V, 72 dB gain, 2.8 kHz cut-off freq., 12 MHz GBW	Wn1,2 = 20 μm, Ln1,2 = 1 μm; Wp3,4,6 = 25 μm, Lp3,4,6 = 0.5 μm Wn5 = 20 μm, Ln5 = 1 μm; Wn7 = 8.5 μm, Ln7 = 0.5 μm

The offset induced by the interfering signals capacitively coupled to the output pin is shown in Figure 17: the blue line represents the Miller amplifier with active load (A circuit in Figure 16) and the red one represents the amplifier with the passive load (B circuit in Figure 16). The output stage of the amplifier in the open loop configuration is exactly a common source stage and a similar EMI susceptibility could be expected. Instead, as shown by the simulation results plotted in Figure 17, the EMI induced offset has two main differences. The first one is the susceptibility of the amplifier with passive load: although it is much less than the amplifier with active load, it is rather high, much higher than the susceptibility of the simple common source stage with passive load (which is negligible). The maximum offset is indeed 600 mV and the critical frequencies range from tens of MHz up to GHz. The second difference is that the susceptibility of the amplifier with active low decreases at very high frequencies. It does not happen in the simple stages (common source, gate, drain and cascode).

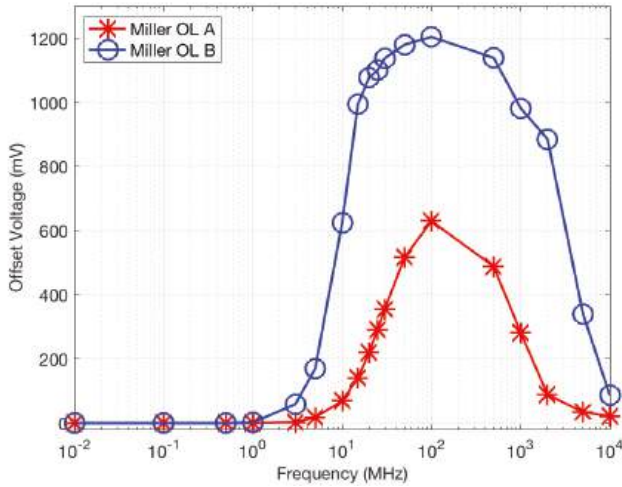


Figure 17. EMI induced offset in the Miller amplifier, open loop configuration.

Finally, another huge difference is the value of the offset, which is much larger than that of the single stage: indeed, the maximum offset is above 1 V in the Miller amplifier, while it is less than 200 mV in the common source stage. One of the possible reason of the different behavior could be the RC network for the frequency compensation. It is indeed in the amplifier schematic, even if it is used in an open loop. The sizing of the RC network is: 3 kΩ for the resistor and 1 pF for the capacitor. The RC network is directly connected to the output pin, it is across the first and the second stage and it may cause a typical phenomenon, Ref. [25–27], called EMI charge pumping, which leads to a severe DC shift of the biasing point. To investigate this, a schematic without the RC network (see Figure 18) has been simulated and the simulation results are plotted in Figure 19.

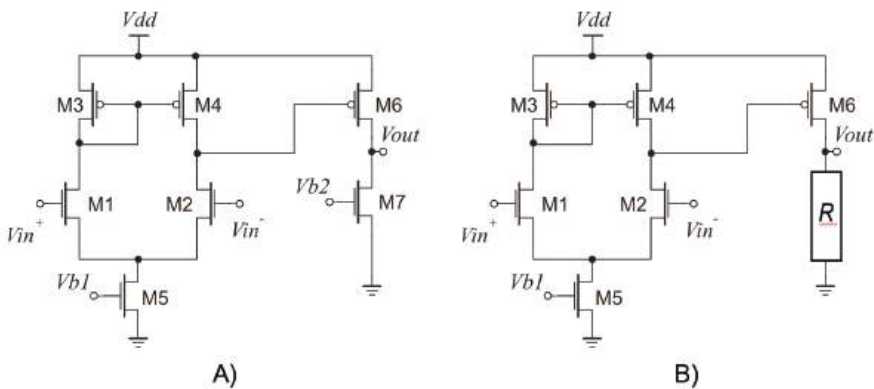


Figure 18. Schematic of the Miller amplifier without the RC network for the frequency compensation: (A) with active load, (B) with resistive load.

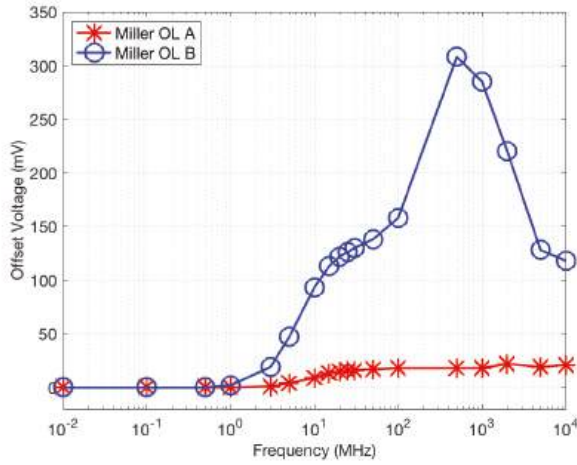


Figure 19. EMI induced offset in the Miller amplifier without RC network, open loop configuration.

By comparing Figures 17 and 19, it results that: the EMI induced offset is much reduced, and it is almost negligible in the case of resistive load (B circuit). On the other hand, there are still some differences which can be due to the first stage of the amplifier, which polarizes the second stage and is also weakly connected to the output node by means of the parasitics.

7.2. Susceptibility of a Two Stages Amplifier in Closed Loop Configuration

The circuits shown in Figure 16 are now connected in a closed loop and the effect of interferences are investigated. The feedback loop decreases the output impedance and a reduction of the EMI induced offset is reasonably expected. The results are indeed plotted in Figure 20.

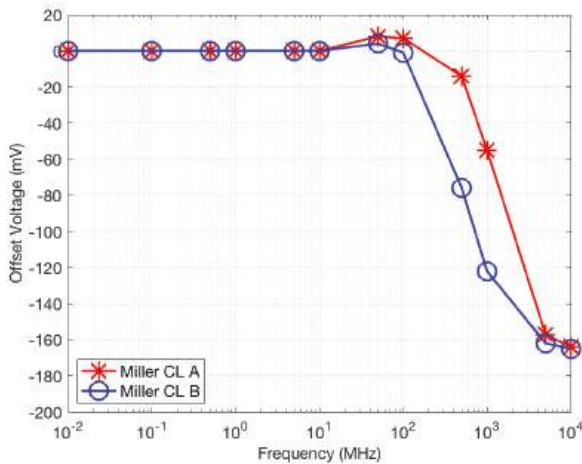


Figure 20. EMI induced offset in the Miller amplifier with RC network, closed loop configuration.

The susceptibility is similar to that of a simple common source stage (the maximum EMI induced offset is the same); the behavior of the amplifier with the active load is very similar to that of the

amplifier with resistive load and the range of uncritical frequencies is enlarged up to a few hundreds of MHz.

8. Overview of the Obtained Results

The exact repercussion of electromagnetic interference, which is injected into arbitrary pins of an integrated amplifier, is very hard to predict owing to the fact that all the existing coupling paths need to be taken into account.

The investigation of single stage amplifier, such as common source, common gate, common drain and cascode, is easier, but non trivial. The susceptibility can be related, indeed, to the output impedance. The common source, common gate and cascode stage have a high impedance output node and it is known that the high impedance (floating) node are more prone to pick up the noise. The behavior of the common drain stage is less intuitive, but it can be still attributed to the impedance: at large frequencies the output impedance of the common drain (which is small at low frequencies) grows up. Moreover, the parasitic gate-source capacitance of the common drain creates a feedback from the output to the input and the charge pumping is maximum. This explains the increasing of the EMI induced offset above the hundreds of MHz.

Regarding the two stages amplifier, a distinction must be done between the open loop and closed loop configuration. For the closed loop configuration, it results that the Miller amplifier (independently on the passive or active low) has a negligible offset until 100 MHz. This result is reasonable because the feedback reduces the output impedance and therefore the susceptibility. Moreover, in this case, by choosing one of the several architectures depicted in the literature, with a high immunity to the EMI injected into the input pin [8–10,13–16], the susceptibility to the output pin can be further reduced, ref. [20]. For the open loop configuration, the behavior is rather unpredictable, but it does not depend on the transistor sizing because a common source stage with the same size and biasing has a different behavior (similar to the one depicted in section III). By removing the RC network, the EMI-induced offset assumes more reasonable values. Therefore, a possible cause of the very large offset at the middle high frequencies can be found by comparing the output node with and without the frequency compensation network. We found that the RC decreases the impedance seen from the drain of the PMOS transistor, making it similar to that of the passive load. In brief, the output node could be in a kind of tri-state. An additional voltage buffer could be useful in this case to reduce the output impedance and therefore the susceptibility. The results obtained in the open loop configuration can be also exemplary to understand the behavior of several circuits, such as digital ones and logic gates. Finally, a general consideration is that the behavior at very high frequencies is always difficult to predict. Neither the measurements are so determining, because of the parasitics of the IC package which complicate the analysis.

9. Conclusions

This paper compares the susceptibility to the interferences coupled to the output pin in several different topologies, starting from the single stage amplifiers up to the whole operational Miller amplifier. The output pin is indeed a critical point of injection and therefore effort and attention must be spent to understand the coupling mechanism. The investigation of single stage amplifiers, such as common source, common gate, common drain and cascode, is easier, but non trivial. The susceptibility can be related, indeed, to the output impedance. Regarding the two stages amplifier, similar considerations can be drawn but also a distinction must be done between the open loop and closed loop configuration. In general, the open loop configuration exhibit a larger and less predictable EMI induced offset, while the amplifier with the feedback loop shows a good immunity up to hundreds of MHz.

Author Contributions: All the authors have contributed substantially to the paper. A.R. has provided the simulation tools and has written the paper; L.C. and Z.K.-V. have written the paper and supervised the work. All authors have read and agreed to the published version of the manuscript.

Funding: This research received no external funding.

Conflicts of Interest: The authors declare no conflict of interest.

References

1. Van De Beek, S.; Leferink, F. Robustness of a TETRA Base Station Receiver Against Intentional EMI. *IEEE Trans. Electromagn. Compat.* **2015**, *57*, 461–469. [\[CrossRef\]](#)
2. Dawson, J.F.; Flintoft, I.D.; Kortoci, P.; Dawson, L.; Marvin, A.C.; Robinson, M.P.; Stojilovic, M.; Rubinstein, M.; Menssen, B.; Garbe, H.; et al. A Cost-Efficient System for Detecting an Intentional Electromagnetic Interference (IEMI) attack. In Proceedings of the IEEE International Symposium on Electromagnetic Compatibility, Gothenburg, Sweden, 1–4 September 2014; pp. 1252–1256.
3. *IEEE Draft Recommended; Practice for Protecting Public Accessible Computer Systems from Intentional EMI; IEEE P1642/D10; IEEE: Piscataway, NJ, USA, 2014; pp. 1–31.*
4. Kune, D.F.; Backes, J.; Clark, S.S.; Kramer, D.; Reynolds, M.; Fu, K.; Kim, Y.; Xu, W. Ghost Talk: Mitigating EMI Signal Injection Attacks against Analog Sensors. In Proceedings of the 2013 IEEE Symposium on Security and Privacy, Berkeley, CA, USA, 19–22 May 2013; pp. 145–159.
5. Van De Beek, S.; Leferink, F. Current intentional EMI studies in Europe with a focus on STRUCTURES. In Proceedings of the IEEE International Symposium on Electromagnetic Compatibility Tokyo 2014, Tokyo, Japan, 12–16 May 2014; pp. 402–405.
6. Fiori, F.; Crovetto, P. Prediction of high-power EMI effects in CMOS operational amplifiers. *IEEE Trans. Electromagn. Compat.* **2006**, *48*, 153–160. [\[CrossRef\]](#)
7. Ramdani, M.; Sicard, E.; Boyer, A.; Ben Dhia, S.; Whalen, J.J.; Hubing, T.H.; Coenen, M.; Wada, O. The Electromagnetic Compatibility of Integrated Circuits—Past, Present and Future. *IEEE Trans. Electromagn. Compat.* **2009**, *51*, 78–100. [\[CrossRef\]](#)
8. Crovetto, P.S. Operational amplifier immune to EMI with no baseband performance degradation. *Electr. Lett.* **2010**, *46*, 209–210. [\[CrossRef\]](#)
9. Walravens, C.; Van Winckel, S.; Redoute, J.M.; Steyaert, M. Efficient reduction of electromagnetic interference effects in operational amplifiers. *Electr. Lett.* **2007**, *43*, 84–85. [\[CrossRef\]](#)
10. Richelli, A. CMOS OpAmp resisting to large electromagnetic interferences. *IEEE Trans. Electromagn. Compat.* **2010**, *52*, 1062–1065. [\[CrossRef\]](#)
11. Fiori, F. EMI susceptibility: The achilles' heel of smart power ICs. *IEEE EMC Mag.* **2015**, *4*, 101–105. [\[CrossRef\]](#)
12. Crovetto, P.; Musolino, F. Interference of Spread-Spectrum EMI and Digital Data Links under Narrowband Resonant Coupling. *Electronics* **2020**, *9*, 60. [\[CrossRef\]](#)
13. Richelli, A.; Matig-a, G.; Redoute, J.M. Design of a folded cascode opamp with increased immunity to conducted electromagnetic interference in 0.18 μm CMOS. *Microelectr. Reliab.* **2015**, *55*, 654–661. [\[CrossRef\]](#)
14. Redoute, J.M.; Steyaert, M. EMI-Resistant CMOS Differential Input Stages. *IEEE Trans. Circuits Syst. I Regul. Pap.* **2010**, *57*, 323–331. [\[CrossRef\]](#)
15. Richelli, A. Increasing EMI immunity in novel low-voltage CMOS OpAmps. *IEEE Trans. Electromagn. Compat.* **2010**, *54*, 947–950. [\[CrossRef\]](#)
16. Sbaraini, S.; Richelli, A.; Kovács-Vajna, Z.M. EMI susceptibility in bulk-driven Miller opamp. *Electr. Lett.* **2010**, *46*, 1111–1113. [\[CrossRef\]](#)
17. Redouté, J.-M.; Steyaert, M. An EMI Resisting LIN Driver in 0.35-micron High-Voltage CMOS. *IEEE J. Solid State Circuits* **2007**, *42*, 1574–1582. [\[CrossRef\]](#)
18. Richelli, A.; Delaini, G.; Grassi, M.; Redouté, J.-M. Susceptibility of Operational Amplifiers to Conducted EMI Injected Through the Ground Plane into Their Output Terminal. *IEEE Trans. Reliab.* **2016**, *65*, 1369–1379. [\[CrossRef\]](#)
19. Richelli, A.; Colalongo, L.; Toninelli, L.; Rusu, I.; Redouté, J.-M. Measurements of EMI susceptibility of precision voltage references. In Proceedings of the EMCCompo 2017, St. Petersburg, Russia, 4–8 July 2017.

20. Becchetti, S.; Richelli, A.; Colalongo, L.; Kovács-Vajna, Z.M. A Comprehensive Comparison of EMI Immunity in CMOS Amplifier Topologies. *Electronics* **2019**, *8*, 1181. [[CrossRef](#)]
21. Preibisch, J.B.; Duan, X.; Schuster, C. An Efficient Analysis of Power/Ground Planes With Inhomogeneous Substrates Using the Contour Integral Method. *IEEE Trans. Electromagn. Compatib.* **2014**, *56*, 980–989. [[CrossRef](#)]
22. Kachout, M.; Bel Hadj Tahar, J.; Choubani, F. Modeling of Microstrip and PCB Traces to Enhance Crosstalk Reduction. In Proceedings of the IEEE SIBIRCON-2010, Listvyanka, Russia, 11–15 July 2010; pp. 594–597.
23. Ricchiuti, V. Evaluation of the Effective Electrical Parameters of a PCB Trace for Accurate Signal Integrity Simulations. In Proceedings of the PIERS 2004, Pisa, Italy, 28–31 March 2004; pp. 77–80.
24. Richelli, A.; Kennedy, S.; Redouté, J.M. An EMI-Resistant Common-Mode Cancellation Differential Input Stage in UMC 180 nm CMOS. *IEEE Trans. Electromagn. Compatib.* **2017**, *59*, 2049–2051. [[CrossRef](#)]
25. Redouté, J.-M.; Steyaert, M. *EMC of Analog Integrated Circuits*; Springer: Dordrecht, The Netherlands, 2010.
26. Richelli, A.; Redouté, J.-M. A Methodological Approach to EMI Resistant Analog Integrated Circuit Design. *IEEE EMC Mag.* **2015**, *4*, 92–100.
27. Redouté, J.-M.; Steyaert, M. Current mirror structure insensitive to conducted EMI. *IET Electr. Lett.* **2005**, *41*, 1145–1146. [[CrossRef](#)]



© 2020 by the authors. Licensee MDPI, Basel, Switzerland. This article is an open access article distributed under the terms and conditions of the Creative Commons Attribution (CC BY) license (<http://creativecommons.org/licenses/by/4.0/>).

Article

Hall-Effect Current Sensors Susceptibility to EMI: Experimental Study

Orazio Aiello

Department of Electronics and Telecommunications (DET), Politecnico di Torino, Corso Duca degli Abruzzi 24, I-10129 Torino, Italy; orazio.aiello@polito.it

Received: 27 September 2019; Accepted: 3 November 2019; Published: 8 November 2019

Abstract: The paper deals with the susceptibility to Electromagnetic Interference (EMI) of Hall-effect current sensors. They are usually employed in power systems because of their galvanic isolation. The EMI robustness of such contactless device was compared with that of resistive current sensing (wired method). To this purpose, a printed circuit board (PCB) was fabricated. EMI tests methods such as Bulk Current Injection (BCI), Transverse-Electromagnetic (TEM) cell and Direct Power injection (DPI) were performed to evaluate the robustness of the Hall-Effect current sensor. EMI-induced failures are highlighted by comparing the different measurements tests and setups.

Keywords: hall-effect current sensors; commercial current sensor; electromagnetic compatibility (EMC); electromagnetic interference (EMI); direct power injection (DPI) test; transverse-electromagnetic (TEM) test; bulk current injection (BCI) test

1. Introduction

Current sensing circuits are essential for control and monitoring purposes in switching power supplies. In fact, a current sensor is usually employed in the current-mode loop control of DC-DC converters [1–5]. Among the current sensing techniques, Hall-effect current sensors are sensitive to the magnetic field generated by the current to be detected. This allows keeping the power circuit current flows to be monitored electrically isolated from the sensor [6]. On this basis, Hall-effect sensors are not affected by conducted interference generated by the power system to be monitored [7–10] and are therefore particularly employed in electromagnetically-polluted environments.

In this study, the correctness of Hall-effect current sensor operation in the presence of radiated and conducted Electromagnetic Interference (EMI) was investigated referring to a commercial device. A printed circuit board (PCB) suitable to perform Electromagnetic Compatibility (EMC) test was designed so that a continuous wave (CW) Radio Frequency Interference (RFI) could be superimposed on an operating Hall-effect current sensor according to the respective international standard (such as Bulk Current Injection (BCI) [11], Transverse-Electromagnetic (TEM) cell [12] and Direct Power injection (DPI) [13]).

The paper is organized as follows. In Section 2, the test printed circuit board (PCB) is described. Section 3 focuses on the BCI experimental setup. The results of the respective BCI immunity tests are also reported and discussed. In Section 4, the EMI susceptibility of the Hall-effect is further investigated by TEM cell immunity tests. The DPI tests performed to point out the Hall-effect susceptibility to conducted disturbances are presented in Section 5. Finally, some concluding remarks are drawn in Section 6.

2. Test Board

To compare the EMI robustness of a contactless current sensing approach (that exploits the Hall-effect) and a wired one (based on the voltage drop across a sensing resistance), a test PCB was